Doctoral Dissertation

(Shinshu University)

Studies on the growth of BaTaO$_2$N single crystals by flux method for photocatalytic H$_2$ evolution

LUO, YING

March 2021

Department of Science and Technology, Graduate School of Medicine, Science and Technology

Contents

Abstract

Solar driven water splitting on particulate photocatalysts is a potential way to achieve clean and renewable hydrogen energy. To effectively convert solar energy, the development of visible-light-active photocatalysts has become one of the important targets of researchers in recent years. In this context, (oxy)nitride materials, especially $BaTaO_2N$, have been the subject of investigation due to their narrow band gap and suitable band energy potential. This thesis focuses on the growth of highly crystallized $BaTaO_2N$ with some special surface features by using flux method to obtain an excellent photocatalytic activity for H_2 evolution. $BaTaO_2N$ single crystals exposed with sole {100} facets and co-exposed with anisotropic {100} and {110} facets are primarily fabricated by using the NaCl and KCl flux, respectively. A combination of theoretical and experimental studies has been utilized to understand the different electronic properties between the {100} and {110} facets. Both the top of the valence band and bottom of conduction band for the {100} facets are positioned lower than those for the {110} facets, resulting the photogenerated electrons and holes separately transfer to the {100} and {110} facets. Therefore, $BaTaO_2N$ crystals with co-exposed {100} and {110} facets prepared by KCl flux show a higher photocatalytic performance. Subsequently, other chloride fluxes (RbCl, CsCl, and $BaCl_2 \cdot 2H_2O$) are also employed to prepare $BaTaO_2N$ crystals. Because of the high crystallinity and low defect density, $BaTaO_2N$ crystals prepared by RbCl flux exhibit a significantly higher photocatalytic H_2 evolution rate than those by other fluxes. In addition, suitable synthetic conditions have also been investigated and proposed. Finally, $BaTaO_2N$ crystals with a plate-like structure are achieved by using K_2CO_3–KCl binary flux. Owing to the generation of oxo-complex $[TaO_3]^-$ by the assistance of CO_3^{2-} and the lattice match of the $BaTaO_2N$ (111) plane with the $Ba_5Ta_4O_{15}$ (001) plane, the platy $BaTaO_2N$ crystals with well-developed {111} facets are formed *via* the simultaneous formation and transformation of $Ba_5Ta_4O_{15}$. An excellent photocatalytic performance

for H_2 evolution is obtained at the molar ratio of 20/80 due to the plate-like structure and high crystallinity of the $BaTaO_2N$ photocatalyst. The co-exposure of {100} and {110} facets, higher crystallinity, and platy shape are conductive to the spatial charge separation, the reduction of recombination centers, and the shortening of the migration distance of photogenerated electrons and holes, respectively, thereby resulting in an enhanced photocatalytic performance of $BaTaO_2N$. This finding provides a facile approach for the fabrication of shape-controlled and highly crystallized (oxy)nitride photocatalysts aimed at efficient solar H_2 production.

General Introduction

1. Photocatalytic water splitting

With the increasingly serious of environmental pollution and energy crisis in the word, it is essential to develop clean and sustainable energy resources that neither rely on the fossil fuels nor produce carbon dioxide and other environmentally unfriendly gas. Solar energy has attracted much attention as a promising alternative fuel, as the sunlight reaching the surface of earth on an hourly basis is sufficient to fulfill the annual human energy consumption.[1–4] Therefore, numerous efforts are made to efficiently covert and utilize solar energy. Among them, solar driven water splitting on photocatalysts has been considered as a potential way to convert solar energy to generate clean, renewable, and storable hydrogen energy.[5–11] Since the early 1970s, Honda and Fujishima reported that overall water splitting could be achieved by using TiO_2 as an anode and Pt as a cathode under the ultraviolet (UV) irradiation.[12] Many researchers have extensively studied the development and design of solar driven photoelectrochemical (PEC) cells for efficient utilization of solar energy. However, the proposed system so far is still complicated because of the lack of efficient materials with suitable band structures and appropriate internal properties as the electrodes.[13–15] Solar water splitting on particulate photocatalysts, has also been explored since 1980s, which has been regarded as a low cost and easy to operate technology.[16–18] Moreover, due to the ready synthesis of related photocatalysts and the simple design of reactor and devices, the particulate photocatalyst system also has the potential to realize the large-scale hydrogen production by water splitting.[19–21]

Thermodynamically, water splitting into H_2 and O_2 is an uphill chemical reaction that involves a large positive change in the Gibbs free energy ($\Delta G^o = 237$ KJ·mol^{-1}).[22,23] That is, this reaction cannot proceed spontaneously but requires additional energy. Figure 1 shows the schematic diagram of the photocatalytic water splitting rection, which consists of three main processes: (1) when the semiconductor

materials absorb photons with energies larger than their band gap, electrons located on the valence band are excited to the conduction band, resulting in electron-hole pairs; (2) the photogenerated electrons and holes independently migrate to the surface of semiconductor; and (3) the successfully migrated electrons and holes reduce and oxidize the adsorbed species on the surface of semiconductor, respectively. Except for those involved in the reaction, however, most of the electrons recombine with the holes before migrating to the surface of semiconductor. For each process, there are some requirements and features should be noted.
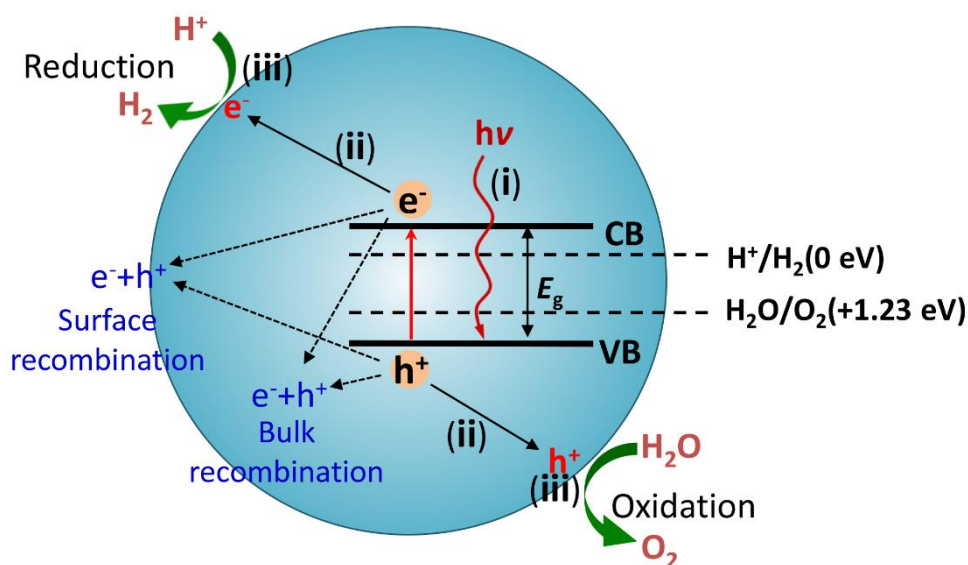

Figure 1. Schematic diagram of the photocatalytic water splitting rection process. VB, valance band; CB, conduction band; E_g, band gap.

In the first process, the requirement for the generation of electron-hole pairs is that the incident energy must be larger than the band gap energy of photocatalysts. Therefore, the utilization range of sunlight depends on the band gap of the photocatalysts. For example, the most widely studied TiO_2 and $SrTiO_3$ have the band gaps of 3.2 eV~3.4 eV, which can only absorb ultraviolet (UV) light with a wavelength of less than 365~390 nm.[24–27] Thus, the band gap of semiconductor becomes an important parameter for the selection of suitable catalysts for solar water splitting. In the second process, charge separation plays a crucial role in determining the photocatalytic performance, numerous attempts were employed to overcome the short lifetime of photogenerated electrons and holes and promote the efficiency of

charge separation. For example, the highly crystallized photocatalyst is generally beneficial for the transfer of photogenerated charges because the defects, which would act as the recombination center, are reduced by the increase in crystallization.[28,29] In addition, for more effective charge separation and transfer, shape control, surface modification, doping and many other methods are considered.[30–33] Photocatalysts with platy, tunnel, and pillared shapes, usually show a large surface area which could shorten the migration distance of photogenerated charges and increase the probabilities of charges reaching the surface of photocatalysts. The surface modification and doping could change the exposed facets and the composition of materials to adjust the surface properties and internal electronic structure, thereby affecting the charge separation. In the third process, the electrons and holes migrate to the surface of semiconductor to participate in the reduction and oxidation half reactions, respectively. To successfully achieve the two half reactions, the potential of conduction band minimum (CBM) should be more negative than that of reducing H^+ to H_2 (0 V $vs.$ NHE), while the potential of valence band maximum (VBM) should be more positive than that of oxidizing H_2O to O_2 (1.23 V $vs.$ NHE).[34,35] In addition, bare photocatalysts usually suffer from lacking active sites for the catalytic reaction. Therefore, cocatalysts are widely used to enhance the photocatalytic performance.

Although a lot of metal oxides with a suitable energy band have been reported, most metal oxides have a wide band gap and can only respond to ultraviolet (UV) light (λ <400 nm) (Figure 2).[22–27,36–38] Since about half of the incident sunlight on the surface of earth is visible light (400 nm $<\lambda$ <760 nm), the development of photocatalysts with narrower band gap to effectively utilize the visible light is indispensable. Until the first half of the 1990s, a few sulfides and oxides, such as CdS and WO_3, were reported to be active as photocatalysts for water splitting under visible light.[39,40] Afterwards, certain chalcogenides (e.g., CdS and CdSe), which have the narrow band gaps to allow absorption of visible light and the suitable band potentials for the water reduction and oxidation reactions, were expected to conduct the overall water splitting or obtain the higher photocatalytic activity. However, since the S^{2-} and

Se^{2-} anions are more easily oxidized than water, CdS and CdSe are unstable in the process of water oxidation, leading to the self-oxidization and degradation of these photocatalysts.[41] Although WO_3 is stable during the reaction, it can only be used as a photocatalyst for oxygen evolution because the potential of CBM of WO_3 is positive than that of reducing H^+ to H_2. Similar results were observed in other oxides (e.g., $BiVO_4$ and Fe_2O_3) with narrow band gaps. To achieve the visible-light-driven water splitting, it is important to design photocatalysts with a suitable band structure and stable property.
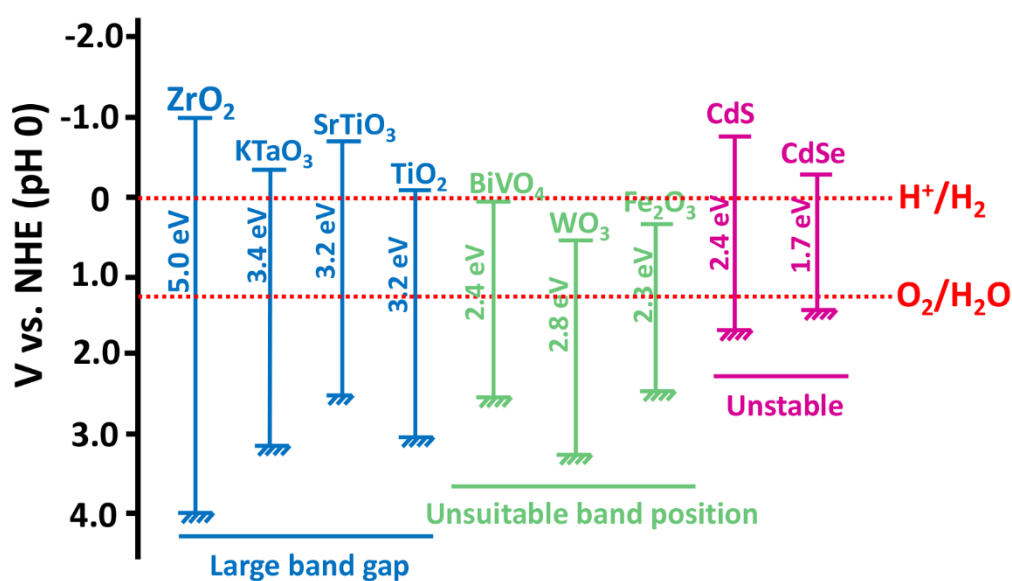

Figure 2. The relationship between the band structures of some representative photocatalysts and the redox potential of water splitting.

2. (Oxy)nitrides and perovskite structure

For the metal oxide photocatalysts, the lowest unoccupied molecular orbitals (LUMOs) mainly consist of transition-metal d orbitals which usually locates at a more negative potential than 0 V (*vs*. NHE), and the highest occupied molecular orbitals (HOMOs) consist of O 2p orbitals which locates at a more positive potential than 3.0 V (*vs*. NHE), thereby these photocatalysts always have a band gap larger than 3.0 eV.[34–38] Considering that the valence band potential of metal oxide photocatalysts is sufficient to oxidize H_2O to O_2 (1.23 V *vs*. NHE), many efforts are made to introduce other

elements to adjust the composition of valence band, such as S and N elements. The potential of S 2p and N 2p orbitals are higher than that of O 2p orbitals, which results in more negative valence band, thus producing a small band gap that is active to the visible light. In particular, (oxy)nitrides and nitrides, including $LaTiO_2N$, $LaTaON_2$, ABO_2N (A = Ca, Sr, Ba; B = Ta, Nb), Ta_3N_5, TaON, etc., have attracted much attention as the promising photocatalysts because they have a sufficiently small band gap (1.7−2.5 eV) that can respond to visible light.[8,42–45] As a simple example, a significant change in band structure is observed when the O atoms in Ta_2O_5 is gradually replaced by N atoms, as shown in Figure 3.[8,42] The VBM (i.e., HOMO) of Ta_2O_5 consists of O 2p, which locates at 3.4 V $vs.$ NHE. Conversely, when the N 2p orbitals is incorporated in the valence band, the VBM moves to 2.0 V $vs.$ NHE and 1.5 V $vs.$ NHE for TaON and Ta_3N_5, respectively, while the potential of the CBM (i.e., LUMO) is almost same. As a result, Ta_3N_5 and TaON show a smaller band gap than Ta_2O_5.
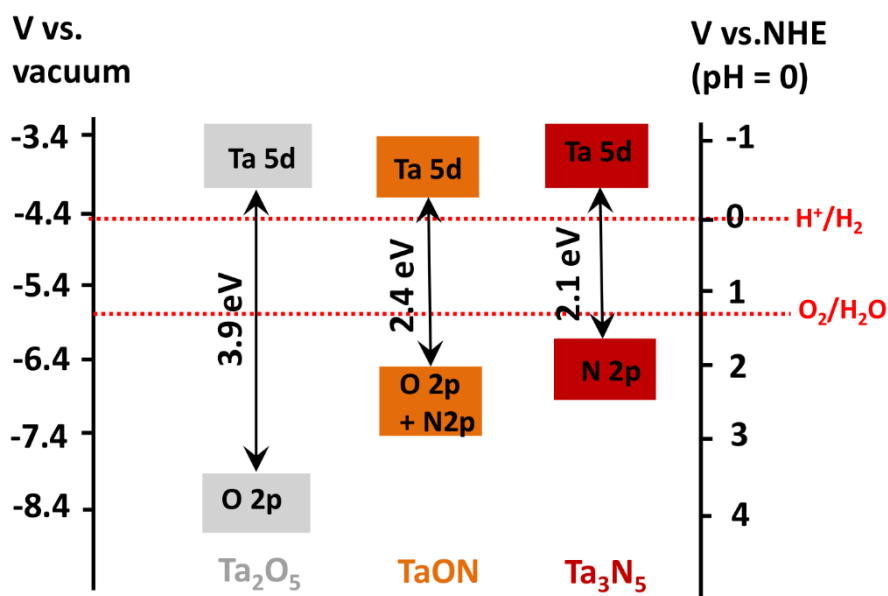
Figure 3. Schematic diagram of the band structures of Ta_2O_5, TaON, Ta_3N_5.

Oxygen and nitrogen have many similarities, such as ionic radius, electronegativity, and polarizability, so they can easily replace each other.[46] They also have many distinct different characteristics, including charges, electron affinity, and bond energy, which would strongly affect the physical and chemical properties of finally obtained materials, as summarized in Table 1.[47,48] Thermodynamically,

compared with (oxy)nitrides, nitrides are less stable and it is difficult to obtain the pure phase nitrides because the nitrogen molecules have extremely strong triple bands. (Oxy)nitrides can not only combine the advantage of oxides and nitrides to keep stable in air, but also allow to form the perovskite structure which cannot be achieved by metal oxides.

Perovskite-type oxides with the general formula ABO_3 (where A is a rare earth, alkaline earth or alkali metal and B is a typically transition metal), have been regarded as an important family of materials and used in numerous technological applications.[49,50] Perovskite materials also show obvious advantages as photocatalysts, as mentioned from Misono and Tanaka:[51] (1) they are composed by a wide variety of elements, while the basic structures are similar; (2) their structure details can be well characterized, and their surface information can be inferred from the well-defined structure information; (3) the valence and stoichiometry of internal constituent can be adjusted by selecting different elements; (4) much information about their physical and chemical properties had been accumulated. Despite many advantages, most of perovskite oxides can only respond UV light, which largely limits their application. Therefore, the discovery of (oxy)nitrides with perovskite structure would undoubtedly promote the further development of perovskite photocatalysts for the visible-light-driven water splitting.

Table 1. Chemical and physical properties of O and N.[46–48]

Parameters	O	N
Charges	–2	–3
Ionic radii (Å)[a]	1.4	1.5
Electronegativity	3.4	3.0
Atomic polarizability (Å^3)	0.8	1.1
Electron affinity (kJ/mol)	601	1736
Bond energy X-X (kJ/mol)[b]	498	941

[a]Coordination number is recognized as 4; [b]X represents O or N atoms.

An ideal perovskite oxide belongs to the cubic structure with $Pm\bar{3}m$ space group,

in which the BO_6 octahedra is combined by sharing corner to form the basic framework, B is located in the center of octahedra, and A is filled in the octahedral interstice. However, under the influence of external conditions (e.g., temperature, pressure, and doping), the real perovskites usually show a degree of lattice distortion because of the octahedron titling around its center, resulting in the crystal phases transform into rhombohedral, monoclinic, orthogonal, tetragonal, and triclinic phase.[49–52] Therefore, the degree of distortion is regarded as an important parameter to evaluate the stability and formability, expressed by tolerance factor. There are two common calculation methods for tolerance factor, depending on ionic radius and cation-anion distances. For perovskite (oxy)nitrides, it can be considered as the position of oxygen in perovskites to be randomly replaced by nitrogen. Thus, the formula for (oxy)nitrides can be similarly expressed as $AB(ON)_3$ which contains two forms of ABO_2N and $ABON_2$, and the corresponding calculations of tolerance factor for each form are shown in the Table 2.[53] Studies have shown that the tolerance factors of structurally stable perovskites are between 0.78 and 1.05.[54] It provides the basis for the preparation and modification of perovskite (oxy)nitrides. To date, only a limited number of (oxy)nitride perovskites have been reported, and even fewer are investigated for photocatalytic water splitting under visible light.

Table 2. Perovskite tolerance factor of ABO_3, ABO_2N and $ABON_2$ depending on ionic radius and cation-anion distances.

Perovskite	Tolerance factor depending on	
	ionic radius	cation-anion distances
ABO_3	$\dfrac{r_A + r_O}{\sqrt{2}(r_B + r_O)}$	$\dfrac{d_{A-O}}{\sqrt{2}d_{B-O}}$
ABO_2N	$\dfrac{[(r_A + r_O)^8(r_A + r_N)^4]^{1/12}}{\sqrt{2}[(r_B + r_O)^4(r_B + r_N)^2]^{1/6}}$	$\dfrac{(\prod_{i=1}^{12} d_{(A-O/N)})^{1/12}}{\sqrt{2}(\prod_{i=1}^{6} d_{(B-O/N)})^{1/6}}$
$ABON_2$	$\dfrac{[(r_A + r_O)^4(r_A + r_N)^8]^{1/12}}{\sqrt{2}[(r_B + r_O)^2(r_B + r_N)^6]^{1/6}}$	$\dfrac{(\prod_{i=1}^{12} d_{(A-O/N)})^{1/12}}{\sqrt{2}(\prod_{i=1}^{6} d_{(B-O/N)})^{1/6}}$

where r_A, r_B, r_O, and r_N are the ionic radius of A, B, oxygen, and nitrogen,

respectively. d_{A-O}, d_{A-O}, $d_{A-O/N}$, and $d_{A-O/N}$, are the cation-anion geometric distance.

Tantalum-based (oxy)nitrides, which have suitable band potentials for water redox reactions, are regarded as a group of very promising photocatalysts for efficient water splitting. $ATaO_2N$ (A = Ca, Ba, Sr), TaON, $LaTaON_2$ are the typical representative tantalum-based (oxy)nitrides and their basic properties related to photocatalytic performance are shown in Table 3.[8,42,43,55–58] Except for TaON, which shows baddeleyite structure, the others exhibit perovskite crystal structure. In addition, although $LaTaON_2$ belongs to perovskite structure, it shows a large distortion of the $Ta(O, N)_6$ octahedral network, and the tolerance factors calculated from ionic radius and cation-anion distances are 0.95 and 0.96, respectively. As shown in Figure 4, $LaTaON_2$ with lattice parameters of a = 8.09 Å, b = 16.12 Å, c = 5.71 Å, α =90º, β =134.82º, and γ = 90º in the *C2/m* space group shows a totally ordered distribution of the anions (oxygen and nitrogen ions), in which two oppositely distributed oxygen and four nitrogen ions form the octahedron, and lanthanum is indirectly filled in the octahedral interstice. It seems that because of this larger distortion, $LaTaON_2$ usually contains more defects and thus exhibits poor performance.

Table 3. Basic properties of representative tantalum-based (oxy)nitrides.

Tantalum-based (oxy)nitrides	Crystal structure	Absorption edge (nm)	Bandgap (eV)
$CaTaO_2N$	Perovskite	510	2.4
$SrTaO_2N$	Perovskite	570	2.2
$BaTaO_2N$	Perovskite	660	1.9
$LaTaON_2$	Perovskite	640	1.9
TaON	Baddeleyite	510	2.4

For $ATaO_2N$ (A = Ca, Ba, Sr), the octahedra consists of four oxygen and two nitrogen ions with disorder distribution and is combined by sharing corner to form the basic framework, as shown in Figure 5. The crystal structure of $CaTaO_2N$ has been solved in the *Pnma* space group, with slightly unbalanced displacement parameters (a

= 5.55 Å, b = 5.63 Å, c = 7.9 Å, α = β = γ = 90º Å) and a small tolerance factor of 0.95. In the case of SrTaO$_2$N, the lattice parameters are a = b = 5.69 Å, c = 8.07 Å, and α = β = γ = 90º in the *I4/mcm* space group. Both CaTaO$_2$N and SrTaO$_2$N have a distortion by the octahedral tilting and show a noticeably smaller Ta-O/N distance of approximately 2.02 Å. BaTaO$_2$N is a cubic perovskite-type compound with lattice parameters of $a = b = c = 4.11$ Å and $α = β = γ = 90º$ in the *Pm$\bar{3}$m* space group and a Ta-O/N distance of 2.06 Å, showing a tolerance factor of 1.04. Due to the simple and reasonable structure, BaTaO$_2$N usually shows fewer defects than other (oxy)nitrides and presents a wide modifiable space.
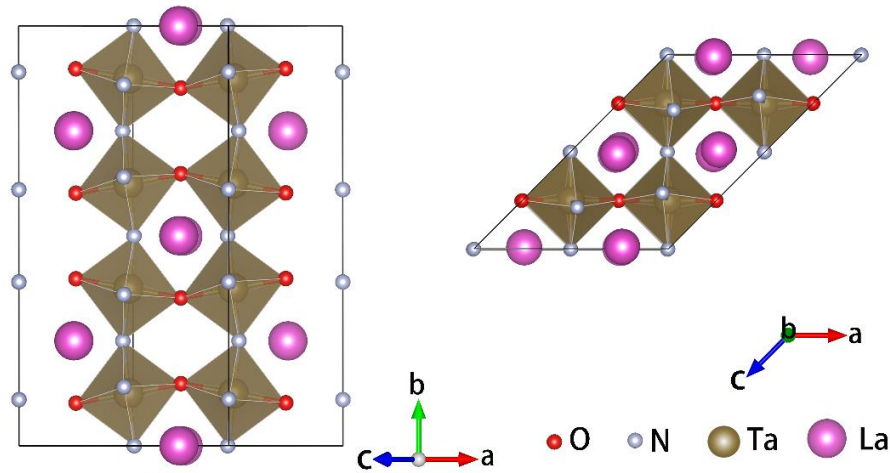

Figure 4. Crystal structure of LaTaON$_2$ viewed from different directions, produced using VESTA program.[59]

It has been demonstrated that BaTaO$_2$N can produce H$_2$ or O$_2$ in the presence of related sacrificial reagents under visible light irradiation because of the narrow band gap (E_g = 1.9 eV) that can harvest visible light up to 660 nm and the suitable band position that straddles the potentials for water reduction and oxidation. Matoba et al. reported that BaTaO$_2$N exhibited hydrogen evolution from water without sacrificial agents under visible light by forming a solid solution with BaZrO$_3$.[60] Ueda et al. prepared a BaTaO$_2$N photoanode by particle transfer method with Co cocatalysts which showed a photocurrent of 4.2 mA·cm^{-2} at 1.2 V$_{RHE}$ in the photoelectrochemical water oxidation reaction under simulated sunlight (AM1.5).[61] Moreover, a certain modified BaTaO$_2$N also was widely used in the two-step photocatalytic water splitting

(Z-scheme) system. Maeda et al. illustrated that the Pt-loaded $BaZrO_3$-$BaTaO_2N$ is the most suitable hydrogen evolution photocatalyst in the Z-scheme system to achieve the simultaneous H_2 and O_2 evolution, in combination with PtO_3/WO_3 or TiO_2 as an oxygen evolution photocatalyst and IO_3^-/I^- pair as redox mediator under visible light.[62] However, the performance of $BaTaO_2N$ photocatalyst is still low due to the lack of suitable methods to obtain crystals with high crystallinity and specific morphology.
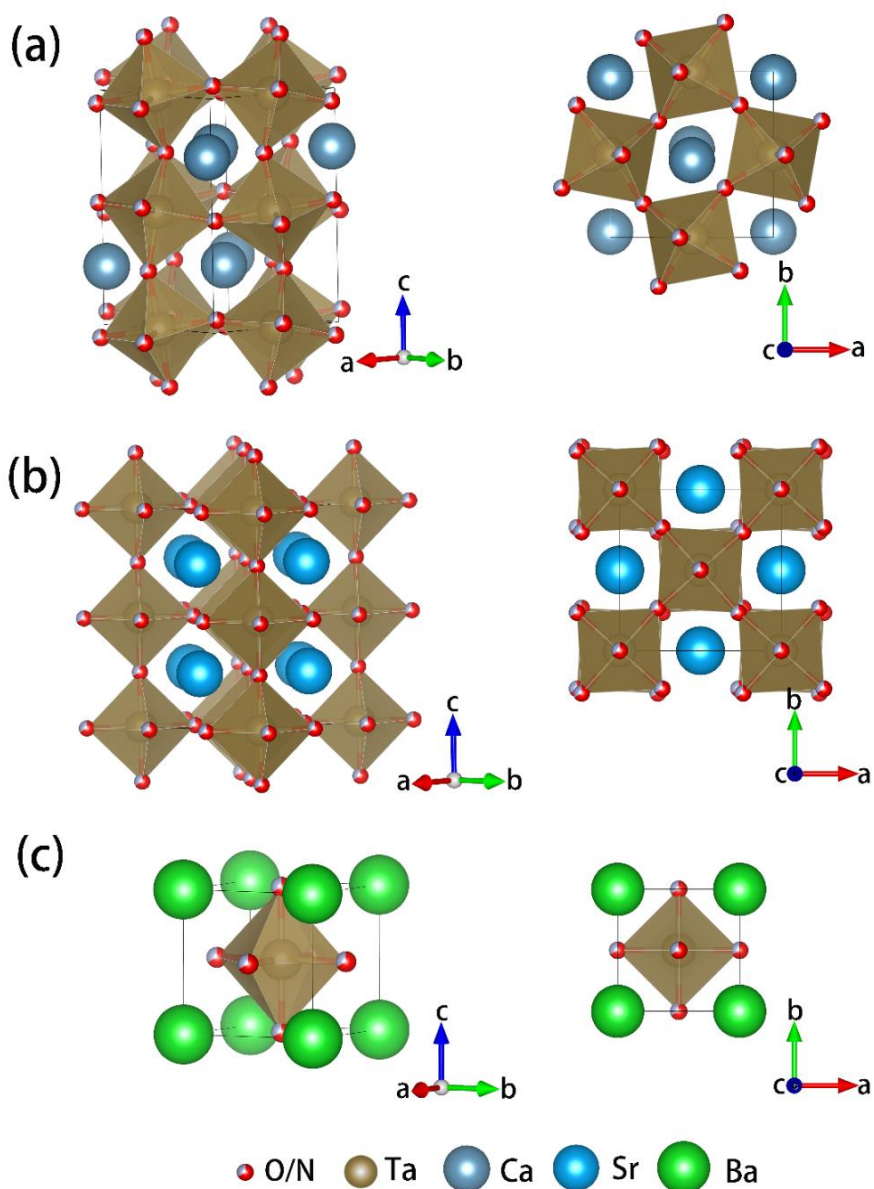

Figure 5. Crystal structures of (a) $CaTaO_2N$, (b) $SrTaO_2N$, and (c) $BaTaO_2N$ viewed from different directions, produced using VESTA program.[59]

3. Preparation of (oxy)nitrides

Compared with metal oxide photocatalysts, the preparation of (oxy)nitride usually requires an ammonia flow and a high temperature. Because of the high stability of N_2, NH_3 gas was widely applied a nitrogen source.[63,64] Generally, the conventional synthesis methods include two step processes: (1) the preparation of corresponding oxide precursors ($Ba_5Ta_4O_{15}$ or $Ba_2Ta_2O_7$) and (2) the high temperature nitridation process in which the O^{2-} ions in oxide precursor was replaced by N^{3-} ions produced by the dissociation of ammonia.[65–67] In the first step, the corresponding precursor can be fabricated *via* traditional solid-state reaction, hydrothermal, and polymerized complex. In the second step, however, there are many limits because of the existence of ammonia. It involves the tail gas treatment and the choice of chemicals. Some elements are banned in ammonia atmosphere. When the temperature is above 600, ammonia would gradually dissociate on the surface of photocatalysts to form active nitriding species, as shown in equation (1)–(4).

$$2NH_3 \rightarrow N_2 + 3H_2 \tag{1}$$

$$2NH_3 \rightarrow 2NH_2 + 3H_2 \tag{2}$$

$$2NH_2 \rightarrow 2NH + 3H_2 \tag{3}$$

$$2NH \rightarrow 2N + 3H_2 \tag{4}$$

It has been demonstrated that N_2 has no effect on the nitridation and the generation of active species at high temperature are important.[68] Therefore, a long reaction time and high reaction temperature are required in this process. Meanwhile, the anion vacancies and some reduced metal species are easily formed due to the charge compensation caused by the replacement of O^{2-} ions with N^{3-} ions and the reducing ammonolysis atmosphere, which act as recombination centers for photogenerated electrons and holes and thereby cause a low activity.[69,70] To reconcile the harsh synthetic condition, a few novel approaches have been explored to reduce the reaction temperature and realize sufficient nitridation. In 2012, Kachina reported that TiN prepared by treating TiO_2 using the NH_3–CCl_4 mixtures exhibited excellent

optical absorption property and high photocatalytic performance.[71] The great advantages of introducing CCl_4 into NH_3 are to obtain highly dispersed nitrogen (equation (5) and (6)) and reduce the nitridation temperature because of the beneficial change in reaction thermodynamics.

$$6TiO_2 + 8NH_3 \rightarrow 6TiN + 12H_2O + N_2 \tag{5}$$

$$6TiO_2 + 6CCl_4 + 8NH_3 \rightarrow 6TiN + 8HCl + N_2 + 6CO_2 \tag{6}$$
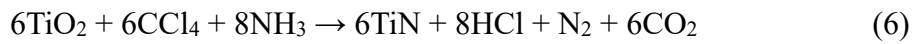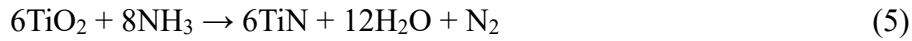
In addition, other nitrogen sources, such as cyanamide and urea, also have been employed for the preparation of (oxy)nitride. Gomathi et al. successfully synthesized a series of (oxy)nitrides $MTaO_2N$ (M = Ca, Sr, or Ba), $MNbO_2N$ (M = Sr or Ba), $LaTiO_2N$ and $SrMoO_{3-x}N_x$ by the urea route.[72] In this method, the corresponding metal carbonates and transition metal oxides as raw materials were mixed with excess urea and then heated at an appropriate temperature in N_2 atmosphere, which avoided proceeding the high ammonolysis process. Urea decomposes at 523 K and almost completely at 823 K. However, although the decomposition temperature of urea was low, the obtained samples have poor crystallinities. As shown in equation (7), NH_3 was produced by the decomposition of urea. To obtain highly crystallized crystals, the reaction temperature should be enhanced and then the ammonia indirectly becomes a nitrogen source.

$$CO(NH_2)_2 \rightarrow NH_3 + HCNO \tag{7}$$

Flux method, which utilizes a high-temperature molten salts (the flux) as the solvent, has been demonstrated to be a powerful method to synthesize the high-quality (oxy)nitride crystals during the high-temperature nitridation process. For example, Kawashima et al. fabricated highly crystallized $LaTiO_2N$ crystals with smooth surface and particle size of 39–120 nm by using KCl flux.[73] It simplified the synthesis process by directly heating the mixtures of source materials (La_2O_3 and TiO_2) and KCl flux under a NH_3 flow and avoided the dissolution and recrystallization of the corresponding oxide precursors ($La_2Ti_2O_7$) compared with the conventional two-step method. With the assistance of KCl flux, $LaTiO_2N$ crystals with low defects were successfully obtained in a relatively short nitridation process and showed a good

activity for photocatalytic O_2 evolution from water. Dong et al. synthesized $BaTaO_2N$ crystal by nitriding the Ba-rich $LiBa_4Ta_3O_{12}$ precursor using flux method and found that this sample showed a higher activity than the conventional sample prepared by solid state reaction, because of the decreased defect density and the enhanced surface area.[74]

Certainly, the selection of suitable flux is the key point to obtain the target products.[75–77] A good flux usually should meet the following requirements: (1) a low melting point, which can decrease the reaction temperature by forming a eutectic melt with precursors; (2) a high solubility for the reagents, which can reduce the diffusion resistance of solute and obtain highly crystalized crystals; (3) low volatility; (4) easy to be removed from the obtained products; (5) low cost; (6) unreactive with the crucible or other experimental tools; (7) low toxicity. Moreover, the anions and cations with special chemical or physical properties in flux also affect the crystal habits. For example, mineralizers (F^-, Cl^-) can be used for stabilizing the complexes to promote the dissolution of precursors and widening the metastable region to alter the viscosity of melt, thereby controlling the growth process. Some oxo-anions, such as SO_4^{2-}, NO_3^- and CO_3^{2-}, tend to generate O^{2-} ions which can promote the dissolution of metal oxides and then form the corresponding oxo-complexes during the high temperature melting reaction, leading to the change of intermediate phase and consequently crystal morphology and crystallinity. Therefore, the types of ions should also be one of the considerations for choosing suitable fluxes.

Bugaris et al. provided a comprehensive review on the application of flux agents for the crystal growth and materials discovery of novel complex oxides.[77] A lot of commonly used fluxes including alkali metal chlorides, carbonates, hydroxides, and some oxides with low melting point were discussed by their applicability and typical reaction temperature. Moreover, many other literatures have introduced and discussed the enhancement of reaction kinetics and crystal growth in the flux agents.[75,76,78–80] The crystal growth process can be simply described as four steps, as shown in Figure 6. Firstly, the reactants gradually decompose and dissolve with increasing temperature (i).

When the temperature is higher than the melting point of the flux, the flux completely melts, and the reactants diffuses through the flux (ii). Once the solute concentration reaches the supersaturation point, the atoms produced by the decomposition of reactants start to aggregate into nuclei (iii). At last, these nuclei grow into nanocrystals with increasingly larger size until the atoms on the surface of the nanocrystals are in equilibrium with the atoms in the solution (iv). During the nucleation and growth stages, the control of growth parameters (such as surface energy, temperature, time, solute concentration etc.,) and crystalline phase is critical in determining the final size, shape, and surface feature. Because of the assistance of flux, highly crystalline and well-developed faceted surface could be obtained in a relatively low reaction temperature.
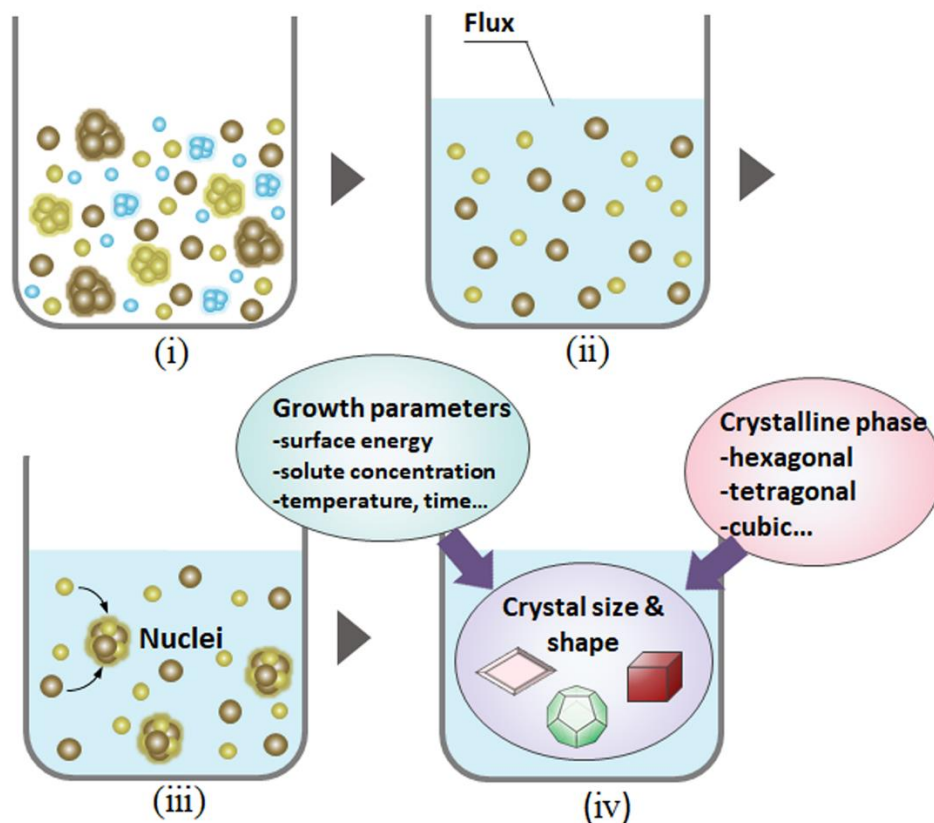

Figure 6. Schematic illustration of the crystal formation in flux: (i) the decomposition and dissolution of reactants; (ii) reactant diffusion through the flux; (iii) nucleation; (iv) crystal growth.

4. Goal and scope of present work

In author's group, it has been reported that $BaTaO_2N$ prepared by one step process using flux method in which the raw materials were directly treated in the NH_3 flow exhibited a higher photocatalytic activity than that by two-step conventional method because it avoids the dissolution and recrystallization of the corresponding oxide precursors.[81] However, there are few reports on the control of crystallinity, surface, and morphology of $BaTaO_2N$ by flux method which have an extremely important effect on photocatalytic performance. Therefore, in this thesis, the goal is to grow high crystalized $BaTaO_2N$ crystals with some special surface features by selecting or combining suitable fluxes to obtain an excellent photocatalytic activity for H_2 evolution.

In Chapter 1, attention is focused on the growth of $BaTaO_2N$ crystals with different exposure facets and investigating its effect on photocatalytic performance. The charge separation has been regarded as one of the most important factors affecting the activity of photocatalysts in solar light-driven water splitting. Some groups have reported that the exposure of anisotropic facets on photocatalysts is beneficial to the charge separation and results in higher activity.[82-84] However, it is difficult to create the exposed facets that facilitate spatial charge separation on (oxy)nitride materials, because the crystal growth of (oxy)nitrides is usually uncontrollable during the conventional high-temperature nitridation procedure.

Here, $BaTaO_2N$ crystals exposed with sole {100} facets and co-exposed with anisotropic {100} and {110} facets are fabricated by using the one-pot NaCl or KCl-assisted nitridation approach, respectively. When modified with Pt as a H_2 evolving cocatalyst, the photocatalytic activity for H_2 production on $BaTaO_2N$ with co-exposed {100} and {110} facets is nearly tenfold over those on $BaTaO_2N$ with only {100} facets or irregularly shape. The enhanced activity is attributed to the efficient spatial charge separation, that is, the accumulation of photogenerated electrons and holes on the {100} and {110} facets of $BaTaO_2N$, respectively.

In Chapter 2, attention is focused on the selection of more suitable flux to obtain BaTaO$_2$N crystals with better crystallinity to further improve the activity. BaTaO$_2$N is an important (oxy)nitride photocatalyst for water splitting under visible light. However, the preparation of BaTaO$_2$N crystals with low defect densities and high crystallinities is challenging *via* ammonolysis at high temperatures. Although NaCl and KCl fluxes are used for assisting the growth of BaTaO$_2$N in the above chapter, no other chloride fluxes are examined for the synthesis of BaTaO$_2$N crystals.

Thus, the effects of the flux type (RbCl, CsCl, and BaCl$_2$·2H$_2$O) on the morphology, crystallinity, and photocatalytic performance of the BaTaO$_2$N crystals are studied initially. It is found that the BaTaO$_2$N crystals grown using a RbCl flux exhibits a significantly higher photocatalytic H$_2$ evolution rate than those grown using the other two fluxes. In particular, the observed activity was almost twice as high as that reported over BaTaO$_2$N crystals grown using a KCl flux. Such an excellent activity is attributed to the lower defect density and higher crystallinity, which are confirmed by UV-vis diffuse reflectance spectroscopy and composition analysis. Subsequently, the effects of the source ratio, solute concentration, reaction temperature and time on the crystallinity and morphology of the BaTaO$_2$N crystals grown using a RbCl flux are studied systematically to gain insight into the BaTaO$_2$N crystal growth mechanism.

In Chapter 3, attention is focused on obtaining platy BaTaO$_2$N crystals and studying its photocatalytic activity for H$_2$ production. Shape-controlled syntheses of inorganic single crystals play a crucial role in the determination of their physical and chemical properties. Nevertheless, the main shape of BaTaO$_2$N is still cubic because BaTaO$_2$N belongs to the cubic system and has a highly symmetric lattice.[85,86] It has been reported that the plate-like structure of photocatalyst materials can decrease the charge carrier diffusion distance from the bulk to the surface, thus promoting the photo-excited charge separation and transfer towards efficient photocatalytic reactions.[87] Therefore, plate-like structured BaTaO$_2$N crystals that are well crystallized are expected to be explored and so are their photocatalytic performances

for H_2 evolution.

Herein, highly crystalline $BaTaO_2N$ crystal with a plate-like structure from K_2CO_3–KCl binary flux under a nitridation atmosphere are fabricated. The fabricated platy $BaTaO_2N$ is characterized and the results as well as formation mechanism are discussed accordingly. Because of the formation of oxo-complex $[TaO_3]^-$ by the assistance of CO_3^{2-} and the dissociation of NH_3, the formation and transformation of $Ba_5Ta_4O_{15}$ occurred simultaneously. Moreover, the atomic arrangement of the $BaTaO_2N$ (111) plane matches well with that of the $Ba_5Ta_4O_{15}$ (001) plane, resulting in a platy $BaTaO_2N$ crystals with well-developed {111} facets. Upon optimizing the molar ratio of K_2CO_3 and KCl, an excellent photocatalytic performance for H_2 evolution is obtained at the molar ratio of 20/80 due to the plate-like structure and high crystallinity of the $BaTaO_2N$ photocatalyst.

5. References

(1) Dresselhaus, M. S.; Thomas, I. L. Alternative Energy Technologies. *Nature* **2001**, *414*, 332–337.

(2) Lewis, N. S. Toward Cost-Effective Solar Energy Use. *Science* **2007**, *315*, 798–801.

(3) Barber, J. Photosynthetic Energy Conversion: Natural and Artificial. *Chem. Soc. Rev.* **2009**, *38*, 185–196.

(4) Wang, Z.; Li, C.; Domen, K. Recent Developments in Heterogeneous Photocatalysts for Solar-Driven Overall Water Splitting. *Chem. Soc. Rev.* **2019**, *48*, 2109–2125.

(5) Maeda, K.; Domen, K. Photocatalytic Water Splitting: Recent Progress and Future Challenges. *J. Phys. Chem. Lett.* **2010**, *1*, 2655–2661.

(6) Kudo, A.; Miseki, Y. Heterogeneous Photocatalyst Materials for Water Splitting. *Chem. Soc. Rev.* **2009**, *38*, 253–278.

(7) Walter, M. G.; Warren, E. L.; McKone, J. R.; Boettcher, S. W.; Mi, Q.; Santori, E. A.; Lewis, N. S. Solar Water Splitting Cells. *Chem. Rev.* **2010**, *110*, 6446–6473.

(8) Xiao, M.; Wang, S.; Thaweesak, S.; Luo, B.; Wang, L. Tantalum (Oxy)Nitride: Narrow Bandgap Photocatalysts for Solar Hydrogen Generation. *Engineering* **2017**, *3*, 365–378.

(9) Hisatomi, T.; Kubota, J.; Domen, K. Recent Advances in Semiconductors for Photocatalytic and Photoelectrochemical Water Splitting. *Chem. Soc. Rev.* **2014**, *43*, 7520–7535.

(10) Osterloh, F. E. Inorganic Materials as Catalysts for Photochemical Splitting of Water. *Chem. Mater.* **2008**, *20*, 35–54.

(11) Lee, J. S. Photocatalytic Water Splitting Under Visible Light with Particulate Semiconductor Catalysts. *Catal. Surv. Asia* **2005**, *9*, 217–227.

(12) Fujishima, A.; Honda, K. Electrochemical Photolysis of Water at a Semiconductor Electrode. *Nature* **1972**, *238*, 37–38.

(13) Khaselev, O.; Turner, J. A. A Monolithic Photovoltaic-Photoelectrochemical Device for Hydrogen Production *via* Water Splitting. *Science* **1998**, *280*, 425–427.

(14) Sakai, Y.; Sugahara, S.; Matsumura, M.; Nakato, Y.; Tsubomura, H. Photoelectrochemical Water Splitting by Tandem Type and Heterojunction Amorphous Silicon Electrodes. *Can. J. Chem.* **1988**, *66*, 1853–1856.

(15) Abe, R. Recent Progress on Photocatalytic and Photoelectrochemical Water Splitting under Visible Light Irradiation. *J. Photochem. Photobiol. C: Photochem. Rev.* **2010**, *11*, 179–209.

(16) Lehn, J. M.; Sauvage, J. P.; Ziessel, R. Photochemical Water Splitting Continuous Generation of Hydrogen and Oxygen by Irradiation of Aqueous Suspensions of Metal Loaded Strontium Titanate. *NouV. J. Chim.* **1980**, *4*, 623–627.

(17) Domen, K.; Naito, S.; Soma, M.; Onishi, T.; Tamaru, K. Photocatalytic Decomposition of Water Vapour on an NiO–SrTiO$_3$ Catalyst. *J. Chem. Soc., Chem. Commun.* **1980**, 543–544.

(18) Fabian, D. M.; Hu, S.; Singh, N.; Houle, F. A.; Hisatomi, T.; Domen, K.; Osterloh F. E.; Ardo, S. Particle Suspension Reactors and Materials for Solar-Driven Water Splitting. *Energy Environ. Sci.* **2015**, *8*, 2825–2850.

(19) Goto, Y.; Hisatomi, T.; Wang, Q.; Higashi, T.; Ishikiriyama, K.; Maeda, T.; Sakata, Y.; Okunaka, S.; Tokudome, H. Katayama, M.; Akiyama, S.; Nishiyama, H.; Inoue, Y.; Takewaki, T.; Setoyama, T.; Minegishi, T.; Takata, T.; Yamada, T.; Domen, K. A Particulate Photocatalyst Water-Splitting Panel for Large-Scale Solar Hydrogen Generation. *Joule* **2018**, *2*, 509–520.

(20) Maeda, K. Z-Scheme Water Splitting using Two Different Semiconductor Photocatalysts. *ACS Catal.* **2013**, *3*, 1486–1503.

(21) Pinaud, B. A.; Benck, J. D.; Seitz, L. C.; Forman, A. J.; Chen, Z.; Deutsch, T. G.; James, B. D.; Baum, K. N.; Baum, G. N.; Ardo, S.; Wang, H.; Millere, E.; Jaramillo, T. F. Technical and Economic Feasibility of Centralized Facilities for Solar Hydrogen Production *via* Photocatalysis and Photoelectrochemistry. *Energy Environ. Sci.* **2013**, *6*, 1983–2002.

(22) Chen, S.; Takata, T.; Domen, K. Particulate Photocatalysts for Overall Water Splitting. *Nat. Rev. Mater.* **2017**, *2*, 17050.

(23) Maeda, K.; Domen K. Photocatalytic Water Splitting: Recent Progress and Future Challenges. *J. Phys. Chem. Lett.* **2010**, *1*, 2655–2661

(24) Abdi, F. F.; Han, L.; A. Smets, H. M.; Zeman, M.; Dam, B.; van de Krol, R. Efficient Solar Water Splitting by Enhanced Charge Separation in a Bismuth Vanadate-Silicon Tandem Photoelectrode. *Nat. Commun.* **2013**, *4*, 2195.

(25) Chen, X.; Shen, S.; Guo, L.; Mao, S. S. Semiconductor-Based Photocatalytic Hydrogen Generation. *Chem. Rev.* **2010**, *110*, 6503–6570.

(26) Takata, T.; Jiang, J.; Sakata, Y.; Nakabayashi, M.; Shibata, N.; Nandal, V.; Seki, K.; Hisatomi, T.; Domen, K. Photocatalytic Water Splitting with a Quantum Efficiency of almost Unity. *Nature* **2020**, *581*, 411–414.

(27) Domen, K.; Naito, S.; Onishi, T.; Tamaru, K. Photocatalytic Decomposition of Liquid Water on a NiO-SrTiO$_3$ Catalyst. *Chem. Phys. Lett.* **1982**, *92*, 433–434.

(28) Maeda, K.; Domen, K. New Non-Oxide Photocatalysts Designed for Overall Water Splitting under Visible Light. *J. Phys. Chem. C* **2007**, *111*, 7851–7861.

(29) Ebbinghaus, S. G.; Abicht, H. P.; Dronskowski, R.; Muller, T.; Reller, A.;

Weidenkaff, A. Perovskite-Related Oxynitrides-Recent Developments in Synthesis, Characterisation and Investigations of Physical Properties. *Prog. Solid State Chem.* **2009**, *37*, 173–205.

(30) Tong, H.; Ouyang, S.; Bi, Y.; Umezawa, N.; Oshikiri, M.; Ye, J. Nano-Photocatalytic Materials: Possibilities and Challenges. *Adv Mater.* **2012**, *24,* 229–251.

(31) Xiong, J.; Han, C.; Li, Z.; Dou, S. Effects of Nanostructure on Clean Energy: Big Solutions Gained from Small Features. *Sci. Bull.* **2015**, *60*, 2083–2090.

(32) Li, Y.; Li, F.; Li, X.; Song, H.; Lou, Z.; Ye, Z.; Zhu, L. Ultrahigh Efficient Water Oxidation under Visible Light: Using Fe Dopants to Integrate Nanostructure and Cocatalyst in $LaTiO_2N$ System. *Nano Energy* **2016**, *19*, 437–445.

(33) Shen, S.; Zhao, L.; Zhou, Z.; Guo, L. Enhanced photocatalytic hydrogen evolution over Cu-doped $ZnIn_2N$ system. *J. Phys. Chem. C* **2008**, *112*, 16148–16155.

(34) Maeda, K. Photocatalytic Water Splitting using Semiconductor Particles: History and Recent Developments. *J. Photochem. Photobiol. C* **2011**, *12*, 237–268.

(35) Wang, W.; Tade, M. O.; Shao, Z. Research Progress of Perovskite Materials in Photocatalysis-and Photovoltaics-Related Energy Conversion and Environmental Treatment. *Chem. Soc. Rev*. **2015**, *44*, 5371–5408.

(36) Inoue, Y.; Kubokawa, T.; Sato, K. Photocatalytic Activity of Sodium Hexatitanate, $Na_2Ti_6O_{13}$, with a Tunnel Structure for Decomposition of Water. J. Chem. Soc., *Chem. Commun.* **1990**, 1298–1299.

(37) Yanagida, T.; Sakata, Y.; Imamura, H. Photocatalytic Decomposition of H_2O into H_2 and O_2 over Ga_2O_3 Loaded with NiO. *Chem. Lett.* **2004**, *33*, 726.

(38) Liu, H.; Shangguan, W.; Teraoka, Y. Visible-Light-Responding $BiYWO_6$ Solid Solution for Stoichiometric Photocatalytic Water Splitting. *J. Phys. Chem. C* **2008**, *112*, 8521–8523.

(39) Matsumura, M.; Saho, Y.; Tsubomura, H. Photocatalytic Hydrogen Production from Solutions of Sulfite using Platinized Cadmium Sulfide Powder, *J. Phys. Chem*. **1983**, *87*, 3807–3808.

(40) Darwent, J. R.; Mills, A Photo-Oxidation of Water Sensitized by WO_3 Powder. *J. Chem. Soc. Faraday Trans.* **1982**, *78*, 359–367.

(41) Williams, R. Becquerel Photovoltaic Effect in Binary Compounds. *J. Chem. Phys.* **1960**, *32*, 1505–1514.

(42) Chun, W. J.; Ishikawa, A.; Fujisawa, H.; Takata, T.; Kondo, J. N.; Hara, M.; Kawai, M.; Matsumoto, Y.; Domen, K. Conduction and Valence Band Positions of Ta_2O_5, TaON, and Ta_3N_5 by UPS and Electrochemical Methods. *J. Phys. Chem. B* **2003**, *107*, 1798–803.

(43) Balaz, S.; Porter, S. H.; Woodward, P. M.; Brillson, L. J. Electronic Structure of Tantalum Oxynitride Perovskite Photocatalysts. *Chem. Mater.* **2013**, *25*, 3337–3343.

(44) Takata, T.; Pan, C.; Domen, K. Design and Development of Oxynitride Photocatalysts for Overall Water Splitting under Visible Light Irradiation. *ChemElectroChem* **2016**, *3*, 31–37.

(45) Xu, J.; Pan, C.; Takata, T.; Domen, K. Photocatalytic Overall Water Splitting on the Perovskite-Type Transition Metal Oxynitride $CaTaO_2N$ under Visible Light Irradiation. *Chem. Commun.* **2015**, *51*, 7191–7294.

(46) Shannon, R. D. Revised Effective Ionic Radii and Systematic Studies of Interatomic Distances in Halides and Chalcogenides. *Acta Crystallogr A* **1976**, *32*, 751–767.

(47) Baur, W. H. Effective Ionic Radii in Nitrides. *Crystall. Rev.* **1987**, *1*, 59–83.

(48) Pearson, R. G. Negative Electron Affinities of Nonmetallic Elements. *Inorg. Chem.* **1991**, *30*, 2856–2858.

(49) Bhalla, A.; Guo, R.; Roy, R. The Perovskite Structure–a Review of Its Role in Ceramic Science and Technology. *Mater. Res. Innov.* **2000**, *4*, 3–26.

(50) Grabowska, E. Selected Perovskite Oxides: Characterization, Preparation and Photocatalytic Properties–a Review. *Appl. Catal. B: Environ.* **2016**, *186*, 97–126

(51) Tanaka, H.; Misono, M. Advances in Designing Perovskite Catalysts. *Curr. Opin. Solid State Mater. Sci.* **2001**, *5*, 381–387.

(52) Shi, J.; Guo, L. ABO$_3$-Based Photocatalysts for Water Splitting. Progr. *Nat. Sci.: Mater. Int*. **2012**, *22*, 592–615.

(53) Li, W.; Ionescu, E.; Riedel, R. Gurlo, A. Can We Predict the Formability of Perovskite Oxynitrides from Tolerance and Octahedral Factors? *J. Mater. Chem. A* **2013**, *1*, 12239–12245

(54) Randall, C. A.; Bhalla, A. S.; Shrout, T. R.; Cross, L. E. Classification and Consequences of Complex Lead Perovskite Ferroelectrics with Regard to B-site Cation Order. *J. Mater. Res.* **1990**, *5*, 829–834.

(55) Zhou, J.; Zhou, C.; Shi, Z.; Xu, Z.; Yan, S.; Zou, Z. Oriented Attachment Growth of Hundred-Nanometer-Size LaTaON$_2$ Single Crystal in Molten Salts for Enhanced Photoelectrochemical Water Splitting. *J. Mater. Chem. A* **2018**, *6*, 7706–7713.

(56) Kim, Y. Effects of KCl Flux on the Morphology, Anion Composition, and Chromaticity of Perovskite Oxynitrides, CaTaO$_2$N, SrTaO$_2$N, and LaTaON$_2$. *Ceram. International* **2014**, *40*, 5275–5281.

(57) Zhong, Y.; Li, Z.; Zhao, X.; Fang, T.; Huang, H.; Qian, Q.; Chang, X.; Wang, P.; Yan, S.; Yu, Z.; Zou, Z. Enhanced Water-Splitting Performance of Perovskite SrTaO$_2$N Photoanode Film through Ameliorating Interparticle Charge Transport. *Adv. Funct. Mater*. **2016**, *26*, 7156–7163.

(58) Luo, Y.; Suzuki, S.; Wang, Z.; Yubuta, K.; Vequizo, J. J. M.; Yamakata, A.; Shiiba, H.; Hisatomi, T.; Domen, K.; Teshima, K. Construction of Spatial Charge Separation Facets on BaTaO$_2$N Crystals by Flux Growth Approach for Visible-Light-Driven H$_2$ Production. *ACS Appl. Mater. Interfaces* **2019**, *11*, 22264−22271.

(59) Momma, K.; Izumi, F. VESTA 3 for Three-Dimensional Visualization of Crystal, Volumetric and Morphology Data. *J. Appl. Crystallogr.* **2011**, *44*, 1272−1276.

(60) Matoba, T.; Maeda, K.; Domen, K. Activation of BaTaO2N Photocatalyst for Enhanced Non-Sacrificial Hydrogen Evolution from Water under Visible Light by Forming a Solid Solution with BaZrO$_3$. *Chem. Eur. J.* **2011**, *17*, 14731–14735

(61) Ueda, K.; Minegishi, T.; Clune, J.; Nakabayashi, M.; Hisatomi, T.; Nishiyama, H.;

Katayama, M.; Shibata, N.; Kubota, J.; Yamada, T.; Domen, K. Photoelectrochemical Oxidation of Water Using BaTaO$_2$N Photoanodes Prepared by Particle Transfer Method. *J. Am. Chem. Soc.* **2015**, *137*, 2227−2230

(62) Maeda, K.; Lu, D.; Domen, K. Solar-Driven Z-Scheme Water Splitting Using Modified BaZrO$_3$–BaTaO$_2$N Solid Solutions as Photocatalysts. *ACS Catal.* **2013**, *3*, 1026−1033

(63) Zhang, P.; Zhang, J.; Gong, J. Tantalum-based Semiconductors for Solar Water Splitting. *Chem. Soc. Rev*. **2014**, *43*, 4395–422.

(64) Pinaud, B. A.; Vailionis, A.; Jaramillo, T. F. Controlling the Structural and Optical Properties of Ta3N5 Films through Nitridation Temperature and the Nature of the Ta Metal. *Chem. Mater.* **2014**, *26*, 1576–82.

(65) Seo, J.; Nakabayashi, M.; Hisatomi, T.; Shibata, N.; Minegishi, T.; Domen, K. Solar-Driven Water Splitting over a BaTaO2N Photoanode Enhanced by Annealing in Argon. *ACS Appl. Energy Mater.* **2019**, *2*, 5777−5784.

(66) Wang, C.; Hisatomi, T.; Minegishi, T.; Wang, Q.; Zhong, M.; Katayama, M.; Kubota, J.; Domen, K. Synthesis of Nanostructured BaTaO$_2$N Thin Films as Photoanodes for Solar Water Splitting. *J. Phys. Chem. C* **2016**, *120*, 15758–15764.

(67) Higashi, M.; Domen, K.; Abe, R. Fabrication of an Efficient BaTaO2N Photoanode Harvesting a Wide Range of Visible Light for Water Splitting. *J. Am. Chem. Soc.* **2013**, *135*, 10238−10241.

(68) A. Hellwig, A. Hendry, Formation of Barium-Tantalum Oxynitrides. *J. Mater. Sci.* **1994**, *29*, 4686–4693.

(69) Wang, X.; Hisatomi, T.; Wang, Z.; Song, J.; Qu, J.; Takata, T.; Domen K. Core–Shell-Structured LaTaON$_2$ Transformed from LaKNaTaO$_5$ Plates for Enhanced Photocatalytic H$_2$ Evolution. *Angew. Chem.* **2019**, *131*, 1–6.

(70) Wang, C.; Hisatomi, T.; Minegishi, T.; Wang, Q.; Zhong, M.; Katayama, M.; Kubota, J.; Domen, K. Synthesis of Nanostructured BaTaO$_2$N Thin Films as Photoanodes for Solar Water Splitting. *J. Phys. Chem. C* **2016**, *120*, 15758−15764.

(71) Kachina, A.; Puzenat, E.; Ould-Chikh, S.; Geantet, C.; Delichere, P.; Afanasiev, P.

A New Approach to the Preparation of Nitrogen-Doped Titania Visible Light Photocatalyst. *Chem. Mater.* **2012**, *24*, 636−642.

(72) Gomathi, A.; Reshma, S.; Rao, C. N. R. A Simple Urea-Based Route to Ternary Metal Oxynitride Nanoparticles. *J. Solid State Chem.* **2009**, *182*, 72−76.

(73) Kawashima, K.; Hojamberdiev, M.; Wagata, H.; Yubuta, K.; Vequizo, J. J. M.; Yamakata, A.; Oishi, S.; Domen, K.; Teshima, K. NH_3-Assisted Flux-Mediated Direct Growth of $LaTiO_2N$ Crystallites for Visible-Light-Induced Water Splitting. *J. Phys. Chem. C* **2015**, *119*, 15896−15904

(74) Dong, B.; Qi, Y.; Cui, J.; Liu, B.; Xiong, F.; Jiang, X.; Li, Z.; Xiao, Y.; Zhang, F.; Li, C. Synthesis of $BaTaO_2N$ Oxynitride from Ba-Rich Oxide Precursor for Construction of Visible-Light-Driven Z-Scheme Overall Water Splitting. *Dalton Trans.* **2017**, *46*, 10707–10713

(75) Boltersdorf, J.; King, N.; Maggard, P. A. Flux-Mediated Crystal Growth of Metal Oxides: Synthetic Tunability of Particle Morphologies, Sizes, and Surface Features for Photocatalysis Research. *CrystEngComm* **2015**, *17*, 2225−2241

(76) Chen, D. P.; Fu, J.; Skrabalak, S. E. Towards Shape Control of Metal Oxide Nanocrystals in Confined Molten Media. *ChemNanoMat.* **2015**, *1*, 18–26.

(77) Bugaris, D. E.; Zur Loye, H. C. Materials Discovery by Flux Crystal Growth: Quaternary and Higher Order Oxides. *Angew. Chem. Int. Ed.* **2012**, *51*, 3780–3811.

(78) Kim, Y. Effects of KCl Flux on the Morphology, Anion Composition, and Chromaticity of Perovskite Oxynitrides, $CaTaO_2N$, $SrTaO_2N$, and $LaTaON_2$. *Ceram. International* **2014**, *40*, 5275–5281.

(79) Yamada, T.; Murata, Y.; Wagata, H.; Yubuta, K.; Teshima, K. Facile Morphological Modification of $Ba_5Nb_4O_{15}$ Crystals Using Chloride Flux and in Situ Growth Investigation. *Cryst. Growth Des.* **2016**, *16*, 3954−3960.

(80) Xiao, X.; Hayashi, F.; Yubuta, K.; Selloni, A.; Teshima, K. Effects of Alkali Cations and Sulfate/Chloride Anions on the Flux Growth of {001}-Faceted β-Li_2TiO_3 Crystals. *Cryst. Growth Des.* **2017**, *17*, 1118–1124.

(81) Hojamberdiev, M.; Yubuta, K.; Vequizo, J. J. M.; Yamakata, A.; Oishi, S.; Domen, K.; Teshima, K. NH$_3$-Assisted Flux Growth of Cube-like BaTaO$_2$N Submicron Crystals in a Completely Ionized Nonaqueous High-Temperature Solution and Their Water Splitting Activity. *Cryst. Growth Des.* **2015**, *15*, 4663–4671.

(82) Zhang, Y.; Park, S. J. Au-pd Bimetallic Alloy Nanoparticle-Decorated BiPO$_4$ Nanorods for Enhanced Photocatalytic Oxidation of Trichloroethylene. *J. Catal.* **2017**, *355*, 1-10.

(83) Wang, Z.; Inoue, Y.; Hisatomi, T.; Ishikawa, R.; Wang, Q.; Takata, T.; Chen, S.; Shibata, N.; Ikuhara, Y.; Domen, K. Overall Water Splitting by Ta$_3$N$_5$ Nanorod Single Crystals Grown on the Edges of KTaO$_3$ Particles. *Nature Catal.* **2018**, *1*, 756-763.

(84) Li, J.; Li, Y.; Zhang, G.; Huang, H.; Wu, X. One-Dimensional/Two-dimensional Core-Shell-Structured Bi$_2$O$_4$/BiO$_{2-x}$ Heterojunction for Highly Efficient Broad Spectrum Light Driven Photocatalysis: Faster Interfacial Charge Transfer and Enhanced Molecular Oxygen Activation Mechanism. *ACS Appl. Mater. Interfaces* **2019**, *11*, 7112-7122.

(85) Fang, M.; De Wijs, G. A.; Orhan, E.; De With, G.; De Groot, R. A. Hintzen, H. T. Marchand, R. Local Structure and Electronic Properties of BaTaO$_2$N with Perovskite-Type Structure. *J. Phys. Chem. Solids.* **2003**, *64*, 281–286

(86) Luo, Y.; Wang, Z.; Suzuki, S.; Yubuta, K.; Kariya, N.; Hisatomi, T.; Domen, K.; Teshima, K. Fabrication of Single-Crystalline BaTaO$_2$N from Chloride Fluxes for Photocatalytic H$_2$ Evolution under Visible Light. *Cryst. Growth Des.* **2020**, *20*, 255–261.

(87) Ida, S.; Ishihara, T. Recent Progress in Two-Dimensional Oxide Photocatalysts for Water Splitting. *J. Phys. Chem. Lett.* **2014**, *5*, 2533–2542.

Chapter 1. Construction of Spatially Charge-Separation Facets on BaTaO₂N Crystals by Flux Growth Approach for Visible-Light-Driven H₂ Production

1. Introduction

Charge separation is a crucial process for enhancing the solar-to-hydrogen energy conversion efficiency in photocatalytic water splitting by particulate semiconductors.[1–5] Although electron and hole pairs can be generated in one semiconductor by harvesting a wide range of the solar spectrum, they are easily recombined during the migration to the surface because of the lack of an electron or hole transfer pathway and the close proximity of the surface electron-accumulating and hole-accumulating sites. Moreover, modification of H_2-evolving and/or O_2-evolving cocatalysts can provide the catalytic active sites and extract electrons or holes toward the photocatalytic reaction. However, if the cocatalysts are randomly distributed on the surface of the semiconductor, there is a high probability that the cocatalysts will be located at the incorrect surface sites, implying that the H_2-evolving cocatalysts may be positioned at the surface hole-accumulating sites and the O_2-evolving cocatalysts may be placed at the surface electron-accumulating sites. As a result, the separation of the photo-generated electrons and holes toward efficient photocatalytic reactions may be significantly suppressed.[6–9] Therefore, the construction of spatially charge-separation facets on photocatalysts with the site-selectively deposited cocatalyst is regarded as a desirable method to maximize the charge separation efficiency.

Recently, some groups demonstrated that the exposure of anisotropic facets of different photocatalysts was beneficial to the   charge separation, based on the different atomic construction and coordination between two adjacent facets.[10–14] As a representative example, Li et al. achieved considerably high photocatalytic activity based on the efficient charge separation on the different facets of $BiVO_4$ crystals.[15] Additionally, they demonstrated that the selective deposition of reduction and oxidation

cocatalysts on the respective electron-rich and hole-rich facets of $SrTiO_3$ crystals greatly increased the photocatalytic activity.[16] In addition, Jaroniec et al. proved that the co-exposed {001}/{101} facets of TiO_2 exhibited a type-II band alignment according to the different band structures of {001} and {101} facets by density functional theory (DFT) calculations, and a new concept "facet junction" was proposed that may generate an internal field between the anisotropic facets.[17] Thus, efficient charge separation can be realized on the anisotropic facets to enhance the photocatalytic activity of various oxide photocatalysts. However, it is difficult to create the exposed facets that facilitate spatial charge separation based on (oxy)nitride materials whose visible light absorption can reach longer than 600 nm, because the crystal growth of (oxy)nitrides is usually uncontrollable during the conventional high-temperature nitridation procedure.

BaTaO$_2$N with a cubic perovskite structure is regarded as one of the promising photocatalysts, because it has a narrow band gap (E_g = 1.9 eV) that can harvest visible light as long as 660 nm and suitable band positions that straddle the potentials for water reduction and oxidation.[18,19] It has been demonstrated that BaTaO$_2$N can produce H_2 or O_2 photocatalytically from aqueous solutions containing relative sacrificial reagents. Usually, BaTaO$_2$N fabricated through the conventional nitridation process exhibits an irregular morphology without the exposure of clear facets. The one-pot flux-assisted nitridation approach can be a promising way to tailor the crystal morphology of (oxy)nitride materials. By the mediation of the flux reagent, rearrangement and recrystallization of (oxy)nitride precursors in the melting salt occur during the high-temperature nitridation process, which results in the formation of well-grown (oxy)nitride crystals.[20,21] Therefore, symmetric BaTaO$_2$N crystals are expected to be obtained with the selectively exposed facets, and the spatial charge separation between different facets is expected to be investigated. In this study, we focus on the investigation into the effect of BaTaO$_2$N with different exposure facets on photocatalytic performance. BaTaO$_2$N crystals firstly prepare by the one-pot NaCl or KCl-assisted nitridation procedure and conventional method, respectively. The activity for H_2 evolution on each sample located with Pt as a H_2-evolving cocatalyst will be

examined. Subsequently, the theoretical calculation will be used to analyze the electronic structure of facets and combined the experimental results to comprehensive understand the effect of BaTaO$_2$N exposed different facets on the electrons and holes separation.

2. Experimental section

Materials preparation. BaTaO$_2$N crystals were prepared by the one-pot flux-assisted nitridation approach. The starting materials BaCO$_3$ (99.9%) and Ta$_2$O$_5$ (99.9%) were purchased from Wako Pure Chemical Industries, Ltd., and were mixed with flux reagents with a solute concentration of 10 mol.%. Reagent-grade NaCl (99.5%) or KCl (99.5%) was selected as the flux. In order to prevent TaO$_x$N$_y$ formation due to barium volatilization during the nitridation process, the ratio of Ba/Ta was adjusted to 1.1.[22] After manually mixed using mortar, mixtures (~2 g) were put in an alumina crucible and then nitrided at 950 °C for 8 h under a NH$_3$ flow rate of 200 ml·min^{-1}. When the temperature of the tube furnace cooled to 300 °C, the NH$_3$ was converted to N$_2$ and then cooled to room temperature. The obtained samples were washed by hot water a few times to remove the residual flux reagents and then dried at 100 °C for 6 h. For comparison, the BaTaO$_2$N crystal was also nitrided at 950 °C for 8 h without the flux reagent. Hereafter, the flux-assisted samples are denoted as BTON (NaCl) and BTON (KCl), and the conventional sample is denoted as BTON (w/o).

Photocatalytic H$_2$ evolution reaction. Before the photocatalytic H$_2$ evolution reaction, the obtained samples were loaded with Pt by the photo-deposition method. H$_2$PtCl$_6$·6H$_2$O was selected as the precursor, and CH$_3$OH as the hole scavenger. Normally, 0.1 g of the as-prepared powders and CH$_3$OH (10 vol.%) were added in 150 ml of distilled water. After ultrasound for a few minutes, a corresponding amount of H$_2$PtCl$_6$·6H$_2$O was added into the mixtures. The mixed solution was vacuumed using water splitting equipment and irradiated by a 300-W Xe lamp with a 420 nm cutoff filter under continuous stirring. After 5 h, the Pt-deposited powders were obtained, and the system was vacuumed again. Then, the H$_2$ gas was produced and determined.

Theoretical calculation. Plane-wave-based DFT was conducted to obtain the electron structure and energy state location using the CASTEP program.[23] The exchange-correlation functional was treated by Perdew-Burke-Ernzerhof generalized gradient approximation. Geometry optimization of the bulk $BaTaO_2N$ was performed with a 380-eV cut-off energy. In the calculation, the energy convergence accuracy was 5×10^{-6} eV per atom, the force acting on each atom was not more than 0.01 eV $Å^{-1}$, the internal stress was not more than 0.02 GPa, and the maximum displacement tolerance was 5×10^{-4} Å. The calculated parameters were based on the structure of $BaTaO_2N$: $a = b = c = 4.1128$ Å, which formed a cubic perovskite structure with the space group $Pm\overline{3}m$.[24] In the unit cell of $BaTaO_2N$, Ba is at the origin (0, 0, 0) and has a coordination number of 12 with anions (O and N), Ta is at the body center (+1/2, +1/2, +1/2) with octahedral coordination $(Ta(O, N)_6)$, anion with composition of 0.67 and 0.33 for O and N, respectively, is at the face center.

Metal and oxide-selective photo-deposition. The Pt metal particles and MnO_x oxides were photo-deposited on the $BaTaO_2N$ by imitating previous work.[4] It should be noted that the contents of the deposition of the Pt mental particles were modified to 2 wt.% to facilitate observation of the depositional position. 50 mg of as-prepared powders and CH_3OH (20 vol.%) were dissolved in 150 ml of distilled water, and then the mixed solution was operated similarly with H_2 evolution reaction. As for the MnO_x oxide deposition, $Mn(NO_3)_2$ was selected as the precursor and $NaIO_3$ was selected as the electron acceptor. The deposition process is similar to that of the Pt metal particles. The co-deposition of the Pt and MnO_x was performed similarly using photo-deposition with dual precursors.

To alleviate the effect of the metals and oxides being selectively adsorbed onto specific facets, an impregnation method was adopted. The loading amounts of the cocatalysts were consistent with those of the previous photo-deposition process. Pt and MnO_x were impregnated from $H_2PtCl_6·6H_2O$ and $Mn(NO_3)_2$ solutions by post-calcination at 200 °C for 1 h under a H_2 flow and at 350 °C for 1 h in air, respectively.

Characterization. The phase of the obtained samples was analyzed by X-ray diffraction (XRD) (MiniFlexII, Rigaku) with Cu Kα irradiation. The 2θ range was varied from 10 to 80°. The UV-vis diffused reflectance spectroscopy (UV-vis DRS) was recorded using a JASCO V-670 spectrophotometer. The morphologies and elemental chemical analysis were observed by field-emission scanning electron microscopy (FESEM; JSM-7600F, JEOL) and energy-dispersive spectroscopy (EDS; NORAN System 7, Thermo Fisher Scientific, USA) attached to the FESEM. The exposed facets were further verified by transmission electron microscopy (TEM; JEM-2000 EX-II, JEOL) with a 200-kV accelerating voltage. The nitrogen adsorption-desorption isotherm (BELSORP-mini) was recorded to obtain the surface area. The chemical composition and valence of the elements were measured by X-ray photoelectron spectroscopy (XPS, JPS-9010MX, JEOL). The behavior of electrons and holes was investigated using transient absorption spectra (TAS). In this experiment, samples were irradiated by UV laser pulses (355 nm and 0.2 mJ·pulse^{-1}) and measured at 15200 cm^{-1} and 11000 cm^{-1}.
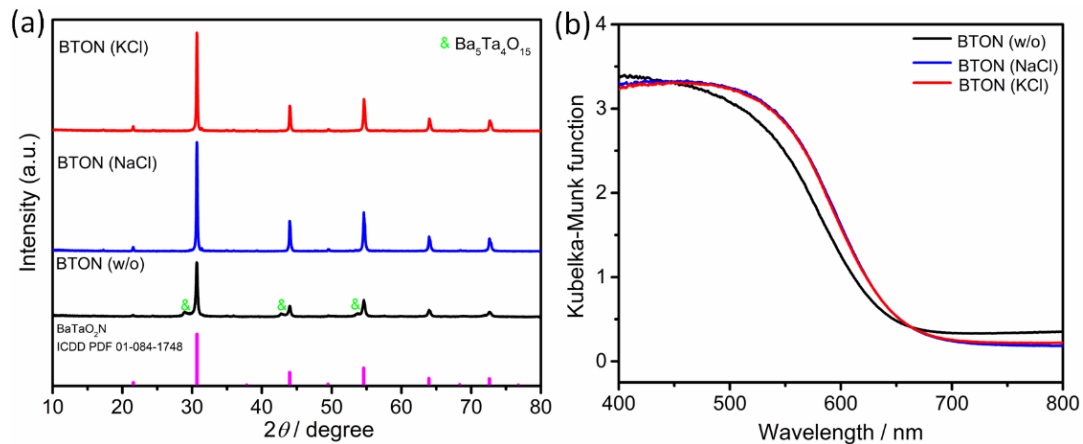
Figure 1. (a) XRD patterns and (b) UV-vis DRS of BTON (w/o), BTON (NaCl) and BTON (KCl).

3. Results and discussion

The crystal structure and visible-light absorption property of different BaTaO$_2$N samples prepared by the one-pot NaCl or KCl-assisted nitridation approach were

characterized by XRD and UV-vis DRS. The XRD patterns of these samples were in good agreement with the cubic perovskite $BaTaO_2N$ structure (ICDD PDF 01-084-1748) except for BTON (w/o), in which a small number of impurities assigned to $Ba_5Ta_4O_{15}$ was observed because of an insufficient nitridation time for the conventional sample (Figure 1a). Moreover, the peak intensities of the BTON (NaCl) and BTON (KCl) samples were higher than that of the BTON (w/o) sample. These results indicate that highly crystalline $BaTaO_2N$ particles with the pure phase were successfully obtained with a relatively short nitridation process with the assistance of flux reagents. In addition, the light absorption edges of both BTON (NaCl) and BTON (KCl) were located at 660 nm, as shown in the UV-vis DRS (Figure 1b), and the existence of $Ba_5Ta_4O_{15}$ impurities led to a blue shift in the absorption edge for BTON (w/o). It should be noted that the background absorption flux-treated $BaTaO_2N$ was lower than that of conventional $BaTaO_2N$, indicating that the flux-assisted nitridation process can decrease the formation of defect densities in $BaTaO_2N$.
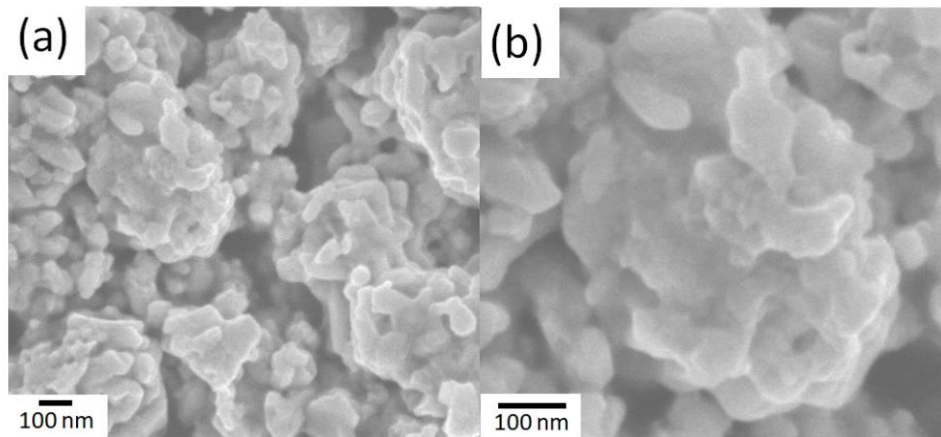
Figure 2. (a) Low- and (b) high-magnification SEM images of BTON (w/o) crystals.
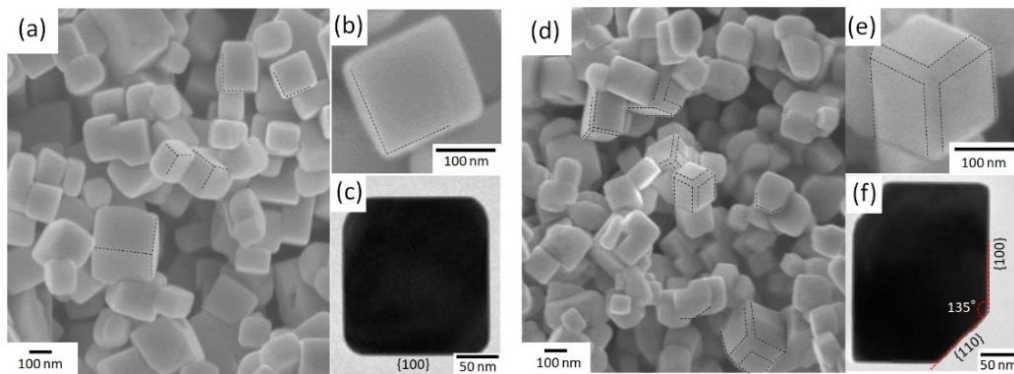
Figure 3. (a) SEM image, (b) high-magnification image and (c) TEM image of BTON (NaCl). (d–f) Similar to (a–c) but for BTON (KCl), respectively.
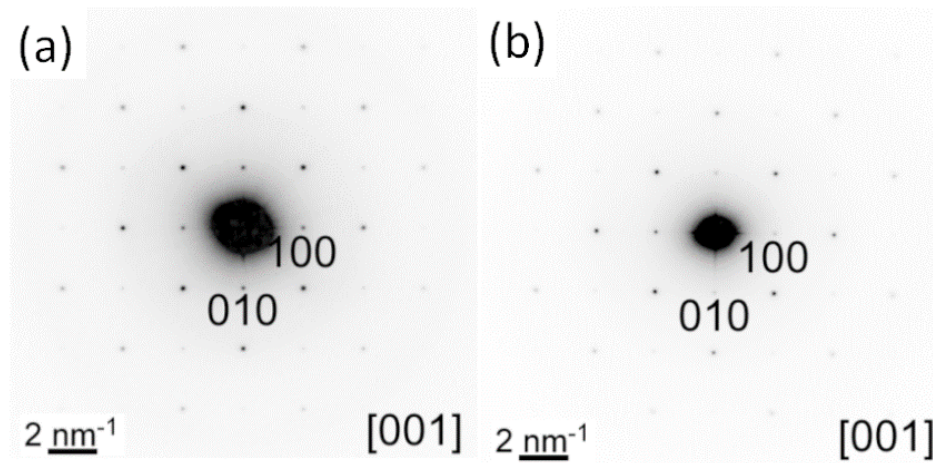
Figure 4. Selected area electron diffraction (SAED) patterns of (a) BTON (NaCl) and (b) BTON (KCl).

The as-prepared samples were further observed by SEM and TEM to confirm the detailed morphological information. As shown in Figure 2, the BTON (w/o) sample exhibits an irregular crystal shape with a severe aggregation of particles. Conversely, the flux treatment gives a significant change in morphology of the $BaTaO_2N$ crystals. The BTON (NaCl) samples grow into an almost perfect cubic structure with six isotropic {100} facets, and the particle size are less than 300 nm (Figures 3a–c). The $BaTaO_2N$ treated by KCl display a similar cubic-like structure and particle size to those treated by NaCl but with exposed smooth edges at the intersection of the {100} facets, as shown in Figures 3d–f. Based on the included angles between the edge and (100) facet (135°, Figure 3f), the corresponding exposed edge planes were determined to be {110} facets. Moreover, the diffraction spots of the selected area electron diffraction in Figure 4 indicate that both the BTON (NaCl) and BTON (KCl) were well-crystallized single crystals. These results demonstrate that the one-pot flux-assisted nitridation approach is a very effective method for tailoring the crystal morphology and obtaining highly crystallized crystals of $BaTaO_2N$ at present. The exposed facets mainly depended on the types of ionic species of the flux reagents. During crystal growth, ionic species of flux reagents will adsorb on the facets which grow rapidly and change the

electrostatic interactions among particles. Compared to Na^+, K^+ more easily occupied the positions of Ba^{2+} on the interfaces between $BaTaO_2N$ and KCl because the size of K^+ (164 pm) is close to that of Ba^{2+} (161 pm). The valence change of cations on the interface will influence the electrostatic interactions and further influence the aggregation and growth of particles, which will prohibit the crystal growth along with the most stable {100} facets and result in the formation of second stable {110} facets. The XPS analysis of BTON (KCl) revealed that the signal could not be observed in the K 2p region (Figure 5a). Furthermore, the position of the main peak (110) at 30.7° did not shift relative to the standard XRD pattern (Figure 5b). These results indicate that the K ions are not retained in the sample, such that the effects of the K species on the surface charge separation can be excluded. Although the exposed {110} facets are not very uniform on the edge, it is clear that a well-structured facet junction was formed in the BTON (KCl) samples, which may benefit charge separation and transfer, thereby enhancing the photocatalytic performance.
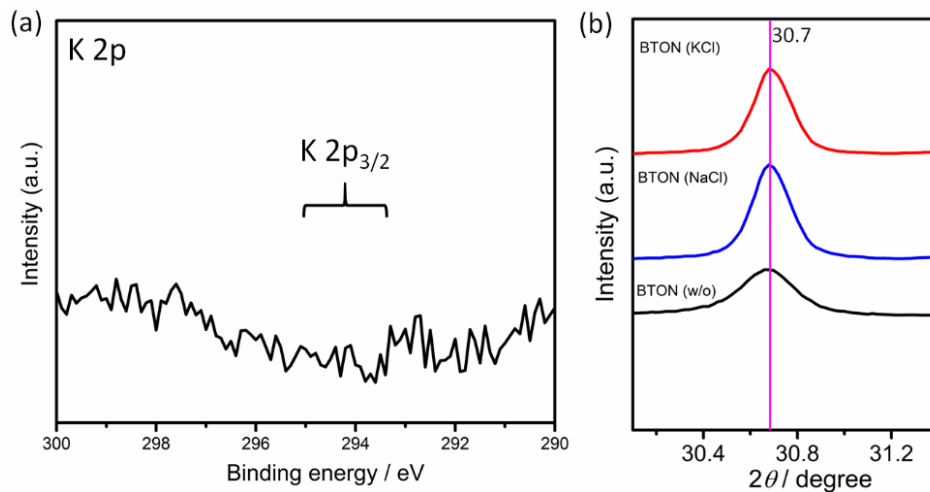
Figure 5. (a) XPS spectrum of K 2p in BTON (KCl). (b) Magnified XRD patterns.

Table 1. Brunauer–Emmett–Teller (BET) surface area of $BaTaO_2N$ crystals.

| Photocatalysts	BET surface area / m^2g^{-1}
BTON (w/o)	5.03
BTON (NaCl)	3.24
BTON (KCl)	3.84
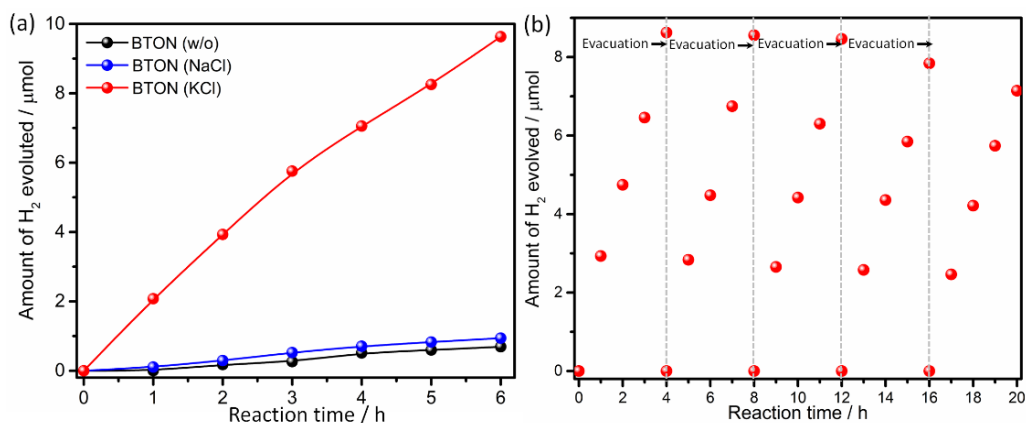
Figure 6. (a) H$_2$ evolution reaction over Pt-modified BTON (w/o), BTON (NaCl), and BTON (KCl), respectively. (b) Cyclic test using BTON (KCl). Reaction conditions: 0.1 wt.% Pt-BTON 0.1g; ultrapure water 150 ml; 10 vol.% CH$_3$OH; 300-W Xe lamp ($\lambda > 420$ nm).
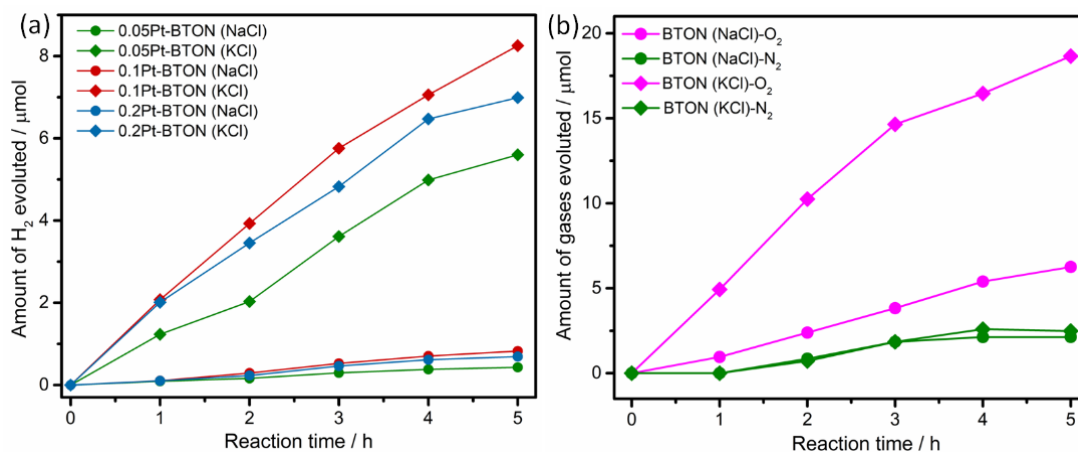

Figure 7. Photocatalytic activities of BTON (NaCl) and BTON (KCl) under visible-light irradiation ($\lambda > 420$ nm). (a) H$_2$ evolution reaction as functions of the amount of Pt. (b) O$_2$ evolution reaction of photocatalysts without cocatalysts modification. Reaction conditions: (a) Pt-modified BTON 0.1g; ultrapure water 150 ml; 10 vol.% CH$_3$OH. (b) BTON 0.1g; ultrapure water 150 ml; La$_2$O$_3$ 0.05g; 0.2 mol L^{-1} AgNO$_3$.
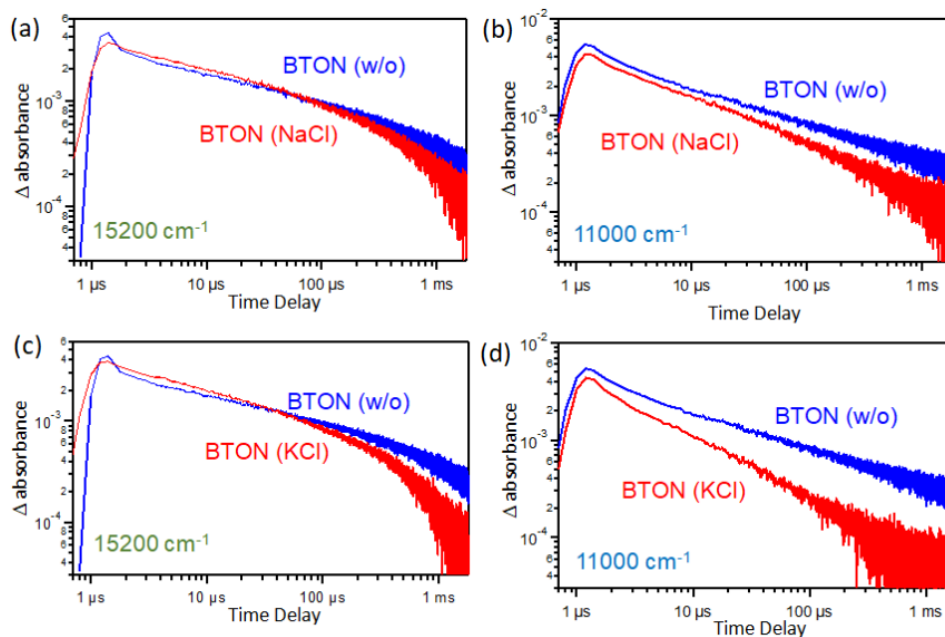
Figure 8. Decay curves of transient absorption of BTON (w/o), BTON (NaCl), and BTON (KCl) irradiated by UV laser pulses (355 nm and 0.2 mJ·pulse^{-1}) probed at (a, c) 15200 and (b, d) 11000 cm^{-1}.

The photocatalytic activity for H$_2$ evolution under visible-light irradiation was investigated using three BaTaO$_2$N samples with different morphologies, as shown in Figure 6a. Both flux-treated BaTaO$_2$N samples show higher photocatalytic activities than the conventional sample, even though the specific surface areas of the former were smaller (Table 1), which implies that the activity of the present samples did not strongly depend on the surface areas. The photocatalytic activity of BTON (NaCl) was slightly higher than that of BTON (w/o), which can be attributable to the high crystallization during the flux-assisted nitridation, leading to a decrease of defect densities. Interestingly, the BTON (KCl) exposed with both {100} and {110} facets exhibited a photocatalytic activity nearly ten times higher than BTON (NaCl) with sole {100} facets, whereas both samples possessed a similar crystallinity and particle size. It is clear that the exposure of both {100} and {110} facets on the BTON (KCl) played an important role in such a significant enhancement of photocatalytic H$_2$ evolution. Figure 6b shows the cyclic H$_2$ evolution reaction using the BTON (KCl) photocatalyst with intermittent evacuation. During the first three cycles, the photocatalytic activity of

BTON (KCl) remained relatively stable. After that, a slight decrease was observed, probably due to the consumption of the sacrificial agent (CH_3OH) in the long photocatalytic reaction. In addition, we explored the effects of the amount of Pt on the BTON (NaCl) and BTON (KCl) (Figure 7a). The photocatalytic activities leading to the H_2 evolution for both samples were found to be similarly dependent on the Pt loading, with the activity increasing sharply with the Pt loading, reaching an optimal level of performance at a Pt content of 0.1 wt.% and then decreasing as the Pt content increased further. It is likely that the number of active sites on the photocatalyst increases as the cocatalyst content increases. However, excessive Pt loading (more than 0.1 wt.%) will block the active sites on the surface and also shade the photocatalyst from the light.[25,26] Moreover, the activities of all the BTON (KCl) samples were much higher than those of all the BTON (NaCl) samples regardless of the amount of Pt. Similar results were obtained from the O_2 evolution reaction, in which the O_2 evolution rate on the BTON (KCl) was significantly higher than that on the BTON (NaCl) (Figure 7b). During the O_2 evolution, a small amount of N_2 was detected under visible-light irradiation because of the self-oxidative decomposition ($2N^{3-} + 6h^+ \longrightarrow N_2$), which has been found in some (oxy)nitrides.[27,28] As the duration of the irradiation increased, this N_2 evolution did not increase notably, but remained relatively balanced. Furthermore, N_2 evolution did not occur in the H_2 evolution test. These results indicate that the $BaTaO_2N$ photocatalyst remains stable in individual oxidation and reduction reactions. The transient absorption spectroscopy curves in Figure 8 display the decay processes of photogenerated charge carriers in three $BaTaO_2N$ photocatalysts by monitoring the absorption intensity changes at 15200 and 11000 cm^{-1}, which reflect the trapped holes and electrons, respectively.[29,30] In comparison to BTON (w/o), BTON (NaCl) exhibits a lower absorption intensity and slightly faster decay at 15200 and 11000 cm^{-1} simultaneously. This indicates that there were fewer defect states in the BTON (NaCl) photocatalyst functioning as trapping centers for photogenerated electrons, and the high crystallization of BTON (NaCl) improved the mobility of photogenerated charges; thus, the contribution of electrons in BTON (NaCl) to the photocatalytic H_2 evolution

reaction increased. Moreover, the absorption intensity of trapped holes and electrons in the BTON (KCl) photocatalyst further decreased and the decay processes clearly accelerated, suggesting that much fewer defect states existed in the BTON (KCl) photocatalyst and the efficient migration of photogenerated charges took place. It is anticipated that the construction of {100} and {110} facets on the BTON (KCl) will result in the spatial separation of photogenerated charges that promote the electron mobility and facilitate electron transfer to the H_2 evolution sites.
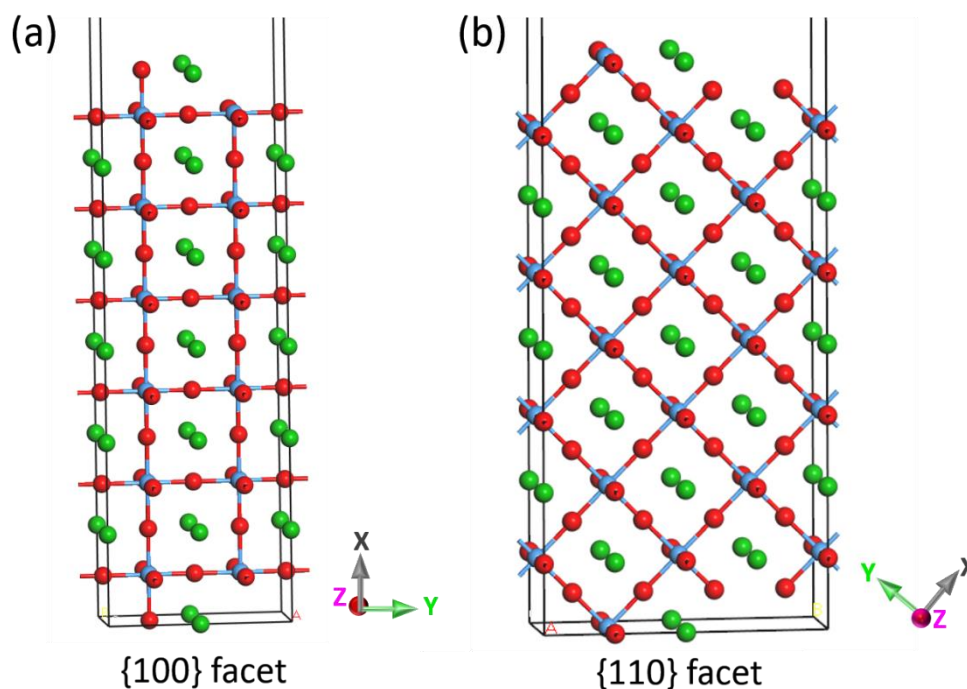
Figure 9. Slabs model of atomic surface structure of $BaTaO_2N$ (a) {100} facet and (b) {110} facet (green ball: Ba atom, blue ball: Ta atom, red ball: O/N atoms). The vertical upward directions of (a) and (b) are [100] and [110], respectively.

To provide insights into the effect of co-exposing {100} and {110} facets on the photocatalytic performance, DFT calculations were performed to study the electronic structure and density of states (DOS) of different $BaTaO_2N$ facets. According to the slab models of {100} and {110} facets (Figure 9), the exposure and bonding of atoms in these facets are different, which results in different electronic structures of these facets. The calculated surface energy of the {110} facet (1.558 J m^{-2}) is higher than that of the {100} facet (1.268 J m^{-2}), implying that the former is less stable than the latter. This

explains why it is not easy to obtain a large surface area of {110} facets.[31] As shown in Figure 10a, the electronic structures of the BaTaO$_2$N facets are similar to those of the bulk BaTaO$_2$N (Figure 11a), where the highest occupied molecular orbital mainly consists of hybridized N 2p and O 2p orbitals, while the lowest unoccupied molecular orbital is mainly composed of the Ta 5d orbital, which is in good agreement with the
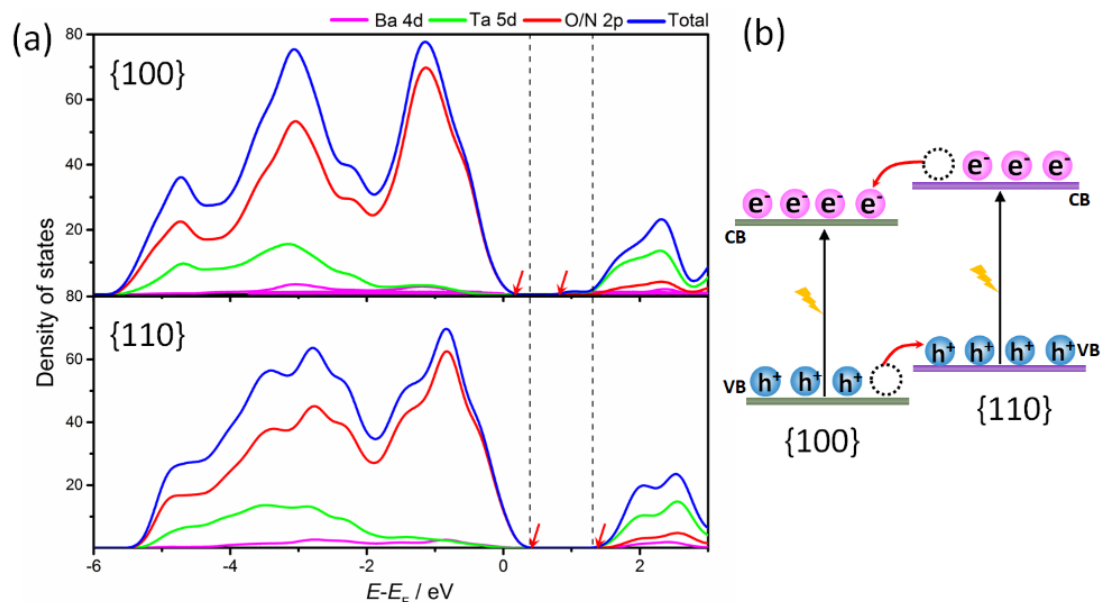

Figure 10. (a) DOS of different energy levels for {100} and {110} facets of BaTaO$_2$N. E_F: Fermi level is set to 0 eV. The red arrows were located on the tops of the valence bands and bottoms of the conduction bands of the {100} and {110} facets, respectively. (b) The diagram of electron-hole transfer in {100} and {110} facet junction.

previous reports.[32,24] It is noticeable that both the top of the valence band and bottom of the conduction band for the {100} facet are positioned lower than those for the {110} facet, respectively. Therefore, a facet junction with type-II band alignment is formed between the co-exposed {100} and {110} facets of BaTaO$_2$N (Figure 10b). Because of the difference in energy levels of {100} and {110} facets, the generation of an internal field between the anisotropic facets makes photogenerated electrons and holes efficiently transfer to the {100} and {110} facets separately.
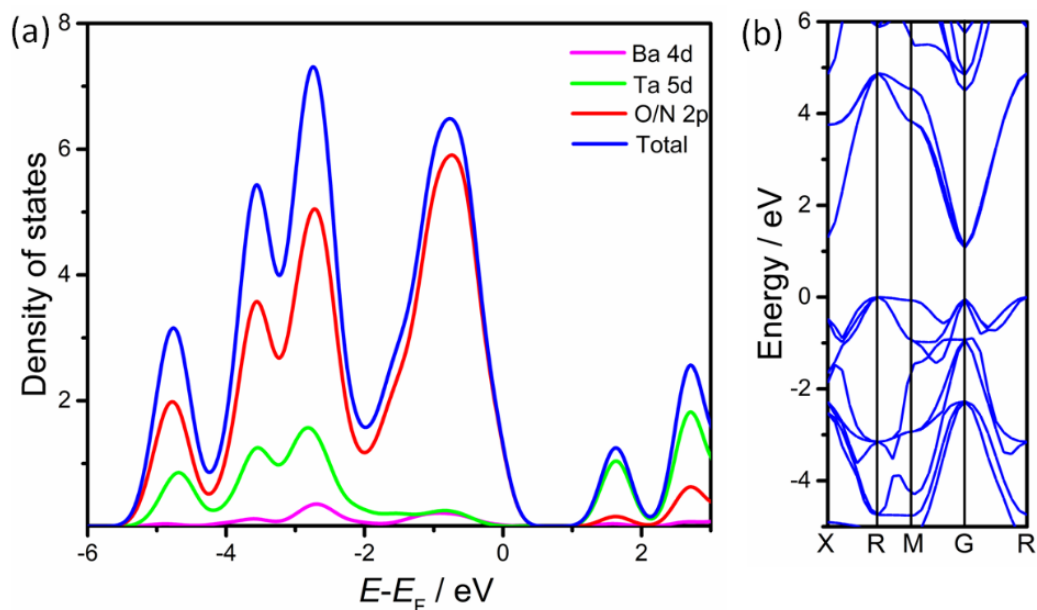
Figure 11. (a) DOS and (b) band structure of $BaTaO_2N$ using bulk model. E_F: Fermi level is set to 0 eV.
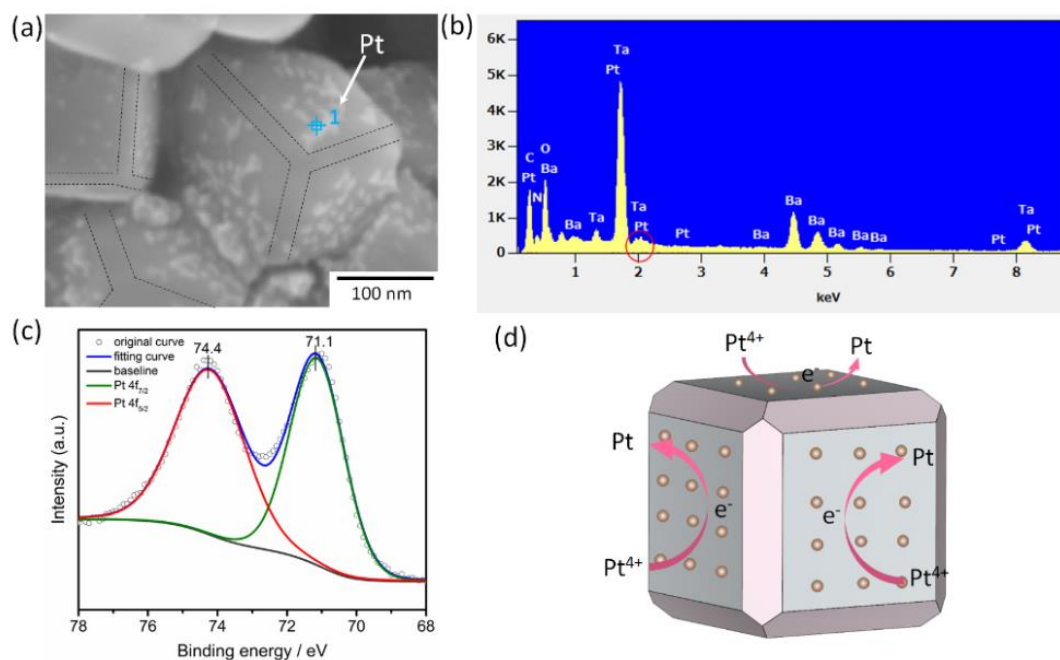

Figure 12. (a) SEM image of photo-deposited metal Pt on the {100} facets. (b) EDS analysis of 1 point of (a). (c) XPS spectrum and (d) schematic illustration of photo-deposited metal Pt on the {100} facets. The diagram in (d) was produced using the VESTA program.[34]

Site-selective photo-depositions of metallic Pt and MnO_x were then carried out to confirm that the photogenerated electrons and holes were spatially separated and

accumulated on the anisotropic facets of BTON (KCl) as predicted by DFT calculations, in which $H_2PtCl_6 \cdot 6H_2O$ and $Mn(NO_3)_2$ were used as precursors. From the SEM images and EDS (Figures 12a, b), it is clearly observed that the Pt particles are primarily formed on the {100} facets, while sponge-like MnO_x species are located on the edges ({110} facets) of the cubic $BaTaO_2N$ (Figures 13a, b). In the XPS of Pt 4f (Figure 12c), the peaks at 74.4 and 71.1 eV are attributed to the Pt $4f_{5/2}$ and Pt $4f_{7/2}$ of metallic Pt, revealing that all of the photo-deposited elements on the {100} facets of BTON (KCl) are metallic.[33] As illustrated in Figure 12d, the photogenerated electrons tend to transfer to the {100} facets and are available for the reduction of $H_2PtCl_6 \cdot 6H_2O$. In addition, photogenerated holes tend to transfer to the {110} facets and facilitate the oxidation of $Mn(NO_3)_2$, as shown in Figure 13d. The oxide form of MnO_x ($x = 1.5$–2) by the photo-oxidation was determined by the binding energy of Mn 2p, which is between Mn_2O_3 and MnO_2 in the XPS (Figure 13c).[16] Following the site depositions, we further investigated the co-deposition of Pt and MnO_x (Figure 14). It is interesting to note that the Pt particles are still primarily formed on the {100} facets, while the sponge-like MnO_x species are selectively located on the {110} facets.
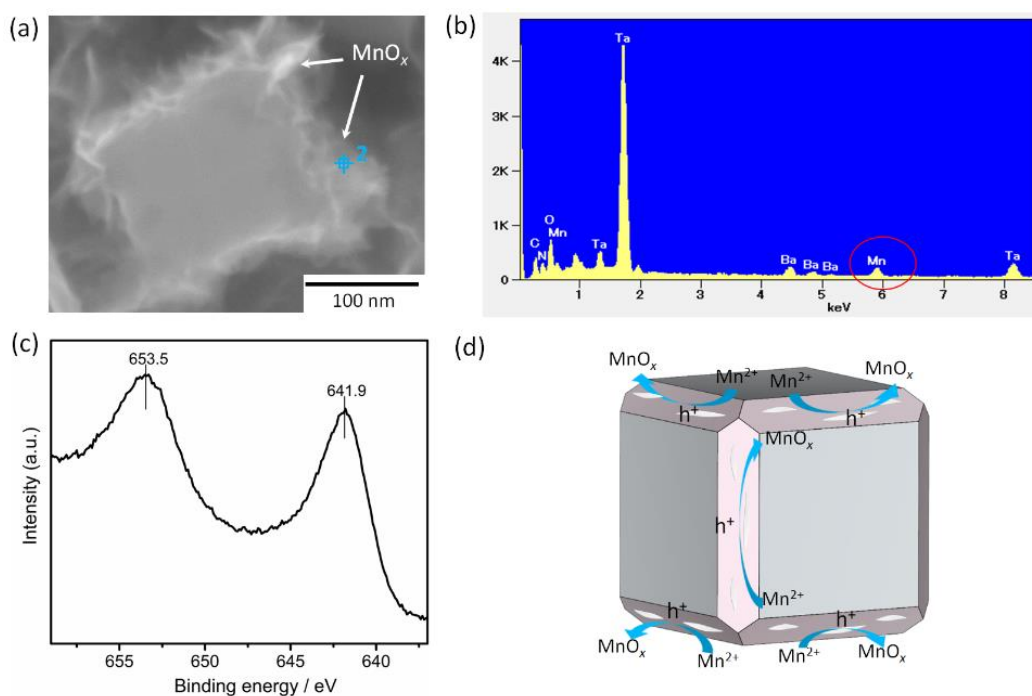

Figure 13. (a) SEM image of photo-deposited oxide MnO_x on the {110} facets. (b) EDS analysis of 2 point of (a). (c) XPS spectrum and (d) schematic illustration of

photo-deposited oxide MnO_x on the {110} facets. The diagram in (d) was produced using the VESTA program.[34]
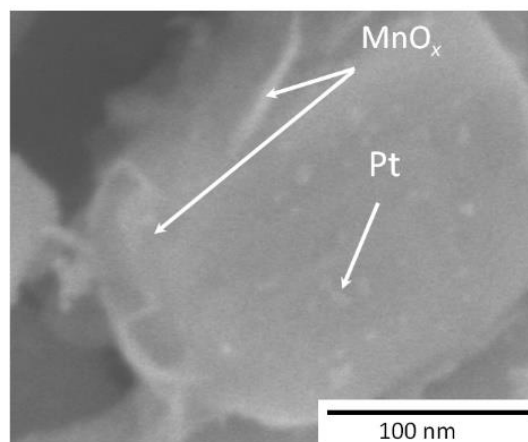

Figure 14. SEM image of photo-deposited dual-cocatalysts (Pt and MnO_x) on BTON (KCl).

There are two possible reasons for the selective photo-deposition of metal ions on different facets: one is the selective accumulation of electrons and holes on the different facets, and the other is the selective adsorption of the reactants on those facets.[15] Meanwhile, the accumulation of electrons and holes on the different facets is affected by the dynamic factor (the difference in the mobility of the charge carriers towards the different facets), as well as the thermodynamic factor (different degrees of surface bending or band alignment for different facets). We firstly checked the adsorption of the reactants on the different facets by using an impregnation method (Figure 15). It was found that Pt particles were randomly formed on both the {100} and {110} facets, while MnO_x species were observed on the {100} facets, thereby excluding the adsorption factor for selective photo-deposition of metal ions on specific facets. Regarding the difference in the mobility, according to the band structure of bulk $BaTaO_2N$ (Figure 11b), we calculated the effective masses of the electrons and holes along the [100] and [110] axes, which are inversely proportional to the mobility,[35] as shown in Table 2. It can be seen that the effective masses of both the electrons and holes along the [110] axis are smaller than those along the [100] axis, indicating that the electrons and holes migrate toward the {110} facet more directly than to the {100} facet. Therefore, the mobility difference cannot be the reason for the selective

43

photo-deposition of metal ions on different facets. On the other hand, based on the DFT calculation results, the work functions of the {100} and {110} facets were 3.11 and 3.19 eV, respectively (Figure 16a, b). Given that all the facets share the same bulk Fermi energy, it can be concluded that the surface band bending for the {110} facet should also be greater than that for the {100} facet (Figure 16c). Therefore, a higher built-in electric field in the space charge region beneath the {110} facet is generated to drive the directional hole accumulation on the {110} surface.[36,37] However, at the same time, such band bending would hinder the migration of electrons from the bulk phase to the surface,[38] leaving the difference in the conduction band positions of the {100} and {110} facets to be the only reason for the electrons to accumulate on the {100} facet, as discussed in Figure 10.
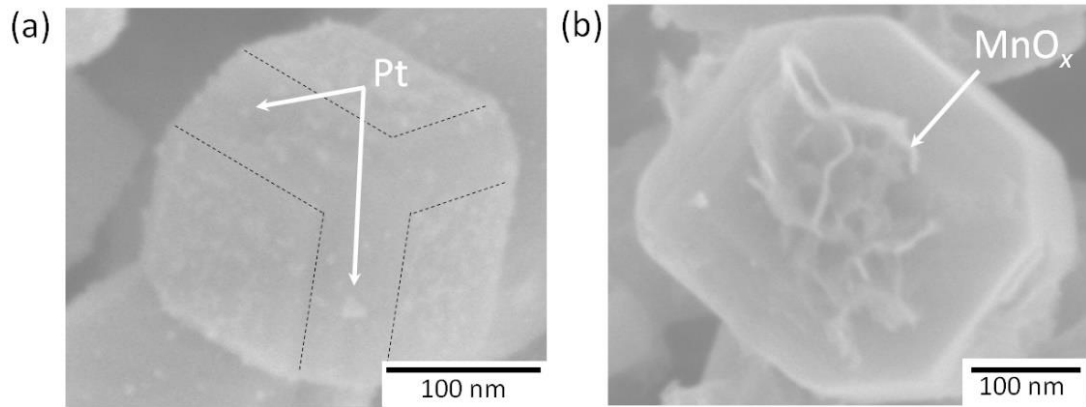

Figure 15. SEM images of impregnated (a) Pt and (b) MnO_x on BTON (KCl), respectively.

Table 2. The calculated effective mass of carriers along the different directions for bulk $BaTaO_2N$.

Direction	Effective mass of electron	Effective mass of hole
[100]	$0.29\ m_0$ (M→ R)	$48\ m_0$ (R→M)
[110]	$0.19\ m_0$ (G→M)	$1.4\ m_0$ (G→M)

m_0 is the mass of free electrons.

The carrier effective mass is calculated by the following formula, $m^* = \hbar^2 [\frac{\partial^2 \varepsilon(k)}{\partial k^2}]^{-1}$ (where $\varepsilon(k)$ are the band edge eigenvalues, k is the wave vector, $\hbar$ is the reduced Planck

constant, and *m** is the carrier effective mass).[35]

 These results further confirmed that reduction reactions preferentially take place on {100} facets, while oxidation reactions preferentially occur on {110} facets, proving that the electron-accumulation and hole-accumulation sites were separately located on the {100} and {110} facets of the BTON (KCl) crystals. As a result, the spatial separation of electron-accumulating and hole-accumulating sites by the construction of {100} and {110} facets on BaTaO$_2$N is beneficial to the separation and transfer of photogenerated charges and consequently promotes the photocatalytic performance of BaTaO$_2$N in this work.
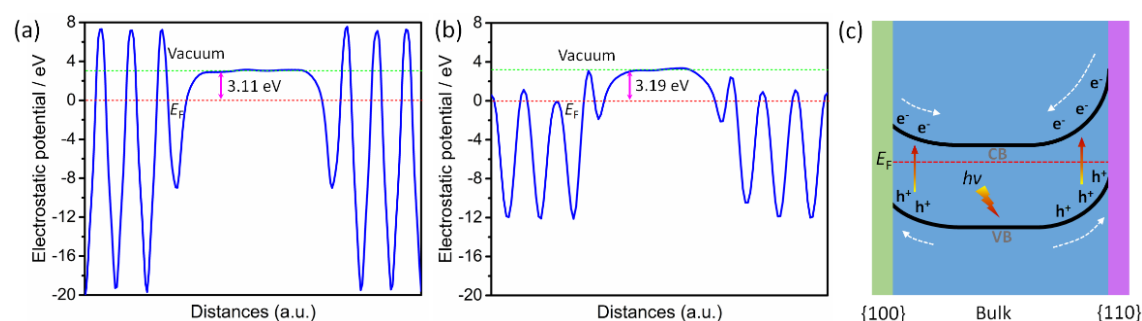

Figure 16. Potential diagrams of (a) {100} and (b) {110} facets based on the first-principles simulation (E_F: Fermi level). (c) Schematic diagram of surface band bending in the ideal case of clean surface model.

4. Conclusion

In summary, symmetric BaTaO$_2$N crystals co-exposed with anisotropic facets were successfully achieved using the one-pot KCl flux-assisted nitridation procedure. The photo-deposition of metal/metal oxide on the corresponding electron/hole-accumulating facets revealed that the photogenerated electrons and holes separately transfer to the {100} and {110} facets of BaTaO$_2$N because of the different energy levels of {100} and {110}. Because of such a spatial separation of charge carriers, the H$_2$ evolution over BaTaO$_2$N crystals with {100} and {110} facets showed a tenfold increase over that of BaTaO$_2$N crystals with sole {100} facets. This finding

provides an innovative approach to the development of efficient (oxy)nitride photocatalysts for solar energy conversion.

5. References

(1) Hirakawa, T.; Kamat, P.V. Charge Separation and Catalytic Activity of Ag@TiO$_2$ Core-Shell Composite Clusters under UV-Irradiation. *J. Am. Chem. Soc.*, *127*, 3928-3934, **2005.**

(2) Tisdale, W. A.; Williams, K. J.; Timp, B. A.; Norris, D. J.; Aydil, E. S.; Zhu, X. Y. Hot-Electron Transfer from Semiconductor Nanocrystal. *Science* **2010**, *328*, 1543-1547.

(3) Zhang, J.; Yu, Z., Gao, Z.; Ge, H., Zhao, S.; Chen, C.; Chen, S.; Tong, X.; Wang, M.; Zheng, Z.; Qin, Y. Porous TiO$_2$ Nanotubes with Spatially Separated Platinum and CoO$_x$ Cocatalysts Produced by Atomic Layer Deposition for Photocatalytic Hydrogen Production. *Angew. Chem. Int. Ed*. **2017**, *56*, 816-820.

(4) Wang, Z.; Inoue, Y.; Hisatomi, T.; Ishikawa, R.; Wang, Q.; Takata, T.; Chen, S.; Shibata, N.; Ikuhara, Y.; Domen, K. Overall Water Splitting by Ta$_3$N$_5$ Nanorod Single Crystals Grown on the Edges of KTaO$_3$ Particles. *Nature Catal*. **2018**, *1*, 756-763.

(5) Wang, Z.; Li, C.; Domen, K. Recent Developments in Heterogeneous Photocatalysts for Solar-Driven Overall Water Splitting. *Chem. Soc. Rev.* **2019**, *48*, 2109-2125.

(6) Zhang, Y.; Park, S. J. Au-pd Bimetallic Alloy Nanoparticle-Decorated BiPO$_4$ Nanorods for Enhanced Photocatalytic Oxidation of Trichloroethylene. *J. Catal*. **2017**, *355*, 1-10.

(7) Zhang, Y.; Park, S. J. Bimetallic AuPd Alloy Nanoparticles Deposited on MoO$_3$ Nanowires for Enhanced Visible-Light Driven Trichloroethylene Degradation. *J. Catal.* **2018**, *361*, 238-247.

(8) Ji, W.; Li, M.; Zhang, G.; Wang, P. Controlled Synthesis of Bi$_{25}$FeO$_{40}$ with Different Morphologies: Growth Mechanism and Enhanced Photo-Fenton Catalytic

Properties. *Dalton Trans.* **2017**, *46*, 10586-10593.

(9) Li, J.; Li, Y.; Zhang, G.; Huang, H.; Wu, X. One-Dimensional/Two-dimensional Core-Shell-Structured Bi_2O_4/BiO_{2-x} Heterojunction for Highly Efficient Broad Spectrum Light Driven Photocatalysis: Faster Interfacial Charge Transfer and Enhanced Molecular Oxygen Activation Mechanism. *ACS Appl. Mater. Interfaces* **2019**, *11*, 7112-7122.

(10) Sun, S.; Gao, P.; Yang, Y.; Yang, P.; Chen, Y.; Wang, Y.; N-doped TiO_2 Nanobelts with Coexposed (001) and (101) Facets and Their Highly Efficient Visible-Light-Driven Photocatalytic Hydrogen Production. *ACS Appl. Mater. Interfaces*, **2016**, *8*, 18126-18131.

(11) Tachikawa, T.; Yamashita, S.; Majima, T. Evidence for Crystal-Face-Dependent TiO_2 Photocatalysis from Single-Molecule Imaging and Kinetic Analysis. *J. Am. Chem. Soc.* **2011**, *133*, 7197-7204.

(12) Gong, H.; Ma, R.; Mao, F.; Liu, K.; Cao, H.; Yan, H. Light-Induced Spatial Separation of Charges Toward Different Crystal Facets of Square-Like WO_3. *Chem. Commun.* **2016**, *52*, 11979-11982.

(13) Zhen, C.; Yu, J. C.; Liu, G.; Cheng, H. M. Selective Deposition of Redox Co-catalyst(s) to Improve the Photocatalytic Activity of Single-Domain Ferroelectric $PbTiO_3$ Nanoplates. *Chem. Commun.* **2014**, *50*, 10416-10419.

(14) Bi, Y.; Ouyang, S.; Umezawa, N.; Cao J.; Ye, J.; Facet Effect of Single-Crystalline Ag_3PO_4 Sub-Microcrystals on Photocatalytic Properties. *J. Am. Chem. Soc.* **2011**, *133*, 6490-6492.

(15) Li, R. G.; Zhang, F. X.; Wang, D. G.; Yang, J. X.; Li, M. R.; Zhu, J.; Zhou, X.; Han, H. X.; Li, C. Spatial Separation of Photogenerated Electrons and Holes Among {010} and {110} Crystal Facets of $BiVO_4$. *Nat. Commun.* **2013**, *4*, 1432.

(16) Mu, L.; Zhao, Y.; Li, A.; Wang, S.; Wang, Z.; Yang, J.; Wang, Y.; Liu, T.; Chen, R.; Zhu, J.; Fan, F.; Li, R.; Li, C. Enhancing Charge Separation on High Symmetry $SrTiO_3$ Exposed with Anisotropic Facets for Photocatalytic Water Splitting. *Energy Environ. Sci.* **2016**, *9*, 2463-2469.

(17) Yu, J.; Low, J.; Xiao, W.; Zhou, P.; Jaroniec, M. Enhanced Photocatalytic CO_2-Reduction Activity of Anatase TiO_2 by Coexposed {001} and {101} Facets. *J. Am. Chem. Soc.* **2014**, *136*, 8839-8842.

(18) Higashi, M.; Domen, K.; Abe, R. Fabrication of an Efficient $BaTaO_2N$ Photoanode Harvesting a Wide Range of Visible Light for Water Splitting. *J. Am. Chem. Soc.* **2013**, *135*, 10238-10241.

(19) Maeda, K.; Lu, D.; Domen, K. Solar-Driven Z-Scheme Water Splitting Using Modified $BaZrO_3$-$BaTaO_2N$ Solid Solutions as Photocatalysts. *ACS Catal.* **2013**, *3*, 1026-1033.

(20) Zhou, J.; Zhou, C.; Shi, Z.; Xu, Z.; Yan, S.; Zou, Z. Oriented Attachment Growth of Hundred-Nanometer-Size $LaTaON_2$ Single Crystal in Molten Salts for Enhanced Photoelectrochemical Water Splitting. *J. Mater. Chem. A* **2018**, *6*, 7706-7713.

(21) Kodera, M.; Urabe, H.; Katayama, M.; Hisatomi, T.; Minegishi, T.; Domen, K. Effects of Flux Synthesis on $SrNbO_2N$ Particles for Photoelectrochemical Water Splitting. *J. Mater. Chem. A* **2016**, *4*, 7658-7664.

(22) Hisatomi, T.; Katayama, C.; Teramura, K.; Takata, T.; Moriya, Y.; Minegishi, T.; Katayama, M.; Nishiyama, H.; Yamada, T.; Domen, K. The Effects of Preparation Conditions for a $BaNbO_2N$ Photocatalyst on Its Physical Properties. *ChemSusChem* **2014**, *7*, 2016-2021.

(23) Lu, W.; Gao, Z.; Liu, X.; Tian, X.; Wu, Q.; Li, C.; Sun, Y.; Liu, Y.; Tao, X. Rational Design of a $LiNbO_3$-Like Nonlinear Optical Crystal, Li_2ZrTeO_6, with High Laser-Damage Threshold and Wide Mid-IR Transparency Window. *J. Am. Chem. Soc.* **2018**, *140*, 40, 13089-13096.

(24) Hibino, K.; Yashima, M.; Oshima, T.; Fujii, K.; Maeda, K. Structures, Electron Density and Characterization of Novel Photocatalysts, $(BaTaO_2N)_{1-x}(SrWO_2N)_x$ Solid Solutions. *Dalton Trans.* **2017**, *46*, 14947-14956.

(25) Chiang, T. H.; Lyu, H.; Hasatomi, T.; Goto, Y.; Takata, T.; Katayama, M.; Minegishi, T.; Domen, K. Efficient Photocatalytic Water Splitting Using Al-doped $SrTiO_3$ Coloaded with Molybdenum Oxide and Rhodium-Chromium Oxide. *ACS*

Catal. **2018**, *8*, 2782-2788.

(26) Ran, J.; Zhang, J.; Yu, J.; Jaroniec, M.; Qiao, S. Z. Earth-Abundant Cocatalysts for Semiconductor-Based Photocatalytic Water Splitting. *Chem. Soc. Rev.* **2014**, *43*, 7787-7812.

(27) Takata, T.; Hitoki, G.; Kondo, J. N.; Hara, M.; Kobayashi, H.; Domen, K. Visible-Light-Driven Photocatalytic Behavior of Tantalum-Oxynitride and Nitride. *Res. Chem. Inter.* **2007**, *33*, 13-25.

(28) Black, A. P.; Suzuki, H.; Higashi, M.; Frontera, C.; Ritter, C.; De, C.; Sundaresan, A.; Abe, R.; Fuertes, A. New Rare Earth Hafnium Oxynitride Perovskites with Photocatalytic Activity in Water Oxidation and Reduction. *Chem. Commun.* **2018**, *54*, 1525-1528.

(29) Yamakata, A.; Vequizo, J. J. M.; Kawaguchi, M. Behavior and Energy State of Photogenerated Charge Carriers in Single-Crystalline and Polycrystalline Powder $SrTiO_3$ Studied by Time-Resolved Absorption Spectroscopy in the Visible to Mid-Infrared Region. *J. Phys. Chem. C* **2015**, *119*, 1880-1885.

(30) Yamakata, A.; Kawaguchi, M.; Nishimura, N.; Minegishi, T.; Kubota, J.; Domen, K. Behavior and Energy States of Photogenerated Charge Carriers on Pt- or CoO_x-Loaded $LaTiO_2N$ Photocatalysts: Time-Resolved Visible to Mid-Infrared Absorption Study. *J. Phys. Chem. C* **2014**, *118*, 23897-23906.

(31) Huang, K.; Yuan, L.; Feng, S. Crystal Facet Tailoring Arts in Perovskite Oxides. *Inorg. Chem. Front.* **2015**, *2*, 965-981.

(32) Hafez, A. M.; Salem, N. M.; Allam, N. K.; Unravelling the Correlated Electronic and Optical Properties of $BaTaO_2N$ with Perovskite-type Structure as a Potential Candidate for Solar Energy Conversion. *Phys. Chem. Chem. Phys*. **2014**, *16*, 18418-18424.

(33) Bera, P.; Priolkar, K. R.; Gayen, A.; Sarode, P. R.; Hegde, M. S.; Emura, S.; Kumashiro, R.; Jayaram, V.; Subbanna, G. N. Ionic Dispersion of Pt over CeO_2 by the Combustion Method: Structural Investigation by XRD, TEM, XPS, and EXAFS. *Chem. Mater.* **2003**, *15*, 2049-2060.

(34) Momma, K.; Izumi, F. VESTA 3 for Three-Dimensional Visualization of Crystal, Volumetric and Morphology Data. *J. Appl. Crystallogr.* **2011**, *44*, 1272-1276.

(35) Xue, J.; Fujitsuka, M.; Majima, T. The Role of Nitrogen Defects in Graphitic Carbon Nitride for Visible-Light-Driven Hydrogen Evolution. *Phys. Chem. Chem. Phys*. **2019**, 21, 2318-2324.

(36) Shi, Z.; Feng, J.; Shan, H.; Wang, X.; Xu, Z.; Huang, H.; Qian, Q.; Yan, S.; Zou, Z. Low Onset Potential on Single Crystal Ta_3N_5 Polyhedron Array Photoanode with Preferential Exposure of {001} Facets. *Appl. Catal. B*, **2018**, *237*, 665-672.

(37) Zhu, J.; Fan, F.; Chen, R.; An, H.; Feng, Z.; Li, C. Direct Imaging of Highly Anisotropic Photogenerated Charge Separations on Different Facets of A Single $BiVO_4$ Photocatalyst. *Angew. Chem. Int. Ed.* **2015**, *54*, 9111-9114.

(38) Zhou, C.; Zhou, J.; Lu, L.; Wang, J.; Shi, Z.; Wang, B.; Pei, L.; Yan, S.; Yu, Z.; Zou, Z. Surface Electric Field Driven Directional Charge Separation on Ta_3N_5 Cuboids Enhancing Photocatalytic Solar Energy Conversion. *Appl. Catal. B*, **2018**, *237*, 742-752.

Chapter 2. Fabrication of Single-Crystalline BaTaO$_2$N from Chloride Fluxes for Photocatalytic H$_2$ Evolution under Visible Light

1. Introduction

Tantalum (oxy)nitrides, such as TaON, Ta$_3$N$_5$, LaTaON$_2$, and ATaO$_2$N (A = Ca, Sr, Ba), have been extensively studied for photocatalytic and photoelectrochemical (PEC) water splitting reactions to convert abundant solar energy into renewable, clean, and storable energy.[1−6] Generally, efficient photocatalysts must possess a narrow band gap to ensure the effective use of sunlight. In addition, they should have suitable band edge positions to straddle the water redox potentials. Compared with traditional transition-metal oxides photocatalysts, whose lowest unoccupied molecular orbitals (LUMOs) and highest occupied molecular orbitals (HOMOs) mainly consist of transition-metal d orbitals and O 2p orbitals, respectively, tantalum-based (oxy)nitrides have HOMOs and LUMOs of Ta 5d orbitals and hybridized N 2p and O 2p orbitals, respectively. The potential of N 2p orbitals is higher than that of O 2p orbitals, which results in the potential of the HOMO of (oxy)nitrides being located at a higher potential energy than that of the corresponding oxide, thereby producing a sufficiently small band gap (1.7−2.5 eV) that can respond to visible light and render tantalum (oxy)nitrides promising photocatalysts.[7−10]

Cubic perovskite-type BaTaO$_2$N is a typical representative of the tantalum (oxy)nitrides and has been demonstrated to produce both H$_2$ and O$_2$ under visible light irradiation in the presence of related sacrificial reagents.[11,12] Like other (oxy)nitrides, BaTaO$_2$N is commonly fabricated *via* the transformation of the precursor oxide during ammonolysis at high temperatures (>700 °C). However, the preparation of these oxynitrides is accompanied by the formation of anion vacancies and reduced tantalum species due to the charge compensation caused by the replacement of oxide ions (O^{2-}) with nitride ions (N^{3-}). Moreover, the formation of reduced tantalum species can also

51

be promoted by the reducing ammonolysis atmosphere. The resulting defects in these materials thereby suppress the charge separation, leading to the inefficient conversion of energy. To achieve a high photocatalytic or PEC performance, the defect densities must be reduced, and the quality of the tantalum (oxy)nitrides crystals must be improved.[13−15]

In this context, flux growth has been demonstrated to be a powerful method for the synthesis of high-quality (oxy)nitride crystals during the high-temperature nitridation procedure, in which a high-temperature molten salt (the flux) is utilized as the solvent for crystallization.[16−18] For example, Zhang et al. achieved single-crystalline $LaTaON_2$ oxynitride crystals *via* a one-pot flux method, where the resulting $LaTaON_2$ exhibited a higher photocatalytic and PEC performance than that prepared *via* polymerization or conventional solid state methods due to the decreased defect density and improved crystallinity.[19] In addition, Kodera et al. reported that $BaNbO_2N$ crystals with different morphologies and crystallinities can be prepared using a range of alkali halide fluxes, and they demonstrated that the types of cations present in the flux play an important role in determining the shapes of the resulting $BaNbO_2N$ crystals.[20] It is noted that the morphology and crystallinity of crystals are also determined by the synthetic conditions employed, as these can influence the solubility of the solutes; examples include the precursor-to-flux molar ratio, the operating temperature, and the nitridation time.[21−23] The optimization of these conditions along with the flux is therefore of particular importance. In our previous report, the photocatalytic H_2 evolution of $BaTaO_2N$ crystals prepared by the flux method was found to be higher than that of crystals prepared by conventional solid state methods due to the improved crystallinity, enhanced particle dispersion, and well-developed facets.[24] In particular, a higher photocatalytic performance was obtained for the $BaTaO_2N$ crystals treated by a KCl flux compared to those treated by a NaCl flux, since the anisotropic facets on the KCl-treated $BaTaO_2N$ crystals were conductive to charge separation, thereby resulting in the efficient conversion of energy. However, no other chloride fluxes were examined for the preparation of $BaTaO_2N$ crystals. We therefore wished to examine whether the

photocatalytic performance of BaTaO$_2$N crystals could be further improved by exploring additional types of chloride flux.

Thus, we herein report our investigation into the effect of different types of chloride flux (i.e., RbCl, CsCl, and BaCl$_2 \cdot$2H$_2$O) in the direct fabrication of single-crystalline BaTaO$_2$N during ammonolysis at high temperatures. The morphologies and photocatalytic performances of the obtained crystals will be examined, paying particular attention to the defect density and the crystallinity. Subsequently, the effects of various experimental parameters (i.e., Ba/Ta molar ratio, solute concentration, holding temperature, and holding time) on the crystallinity and morphology of the BaTaO$_2$N crystals grown using a RbCl flux will be systematically investigated.

2. Experimental section
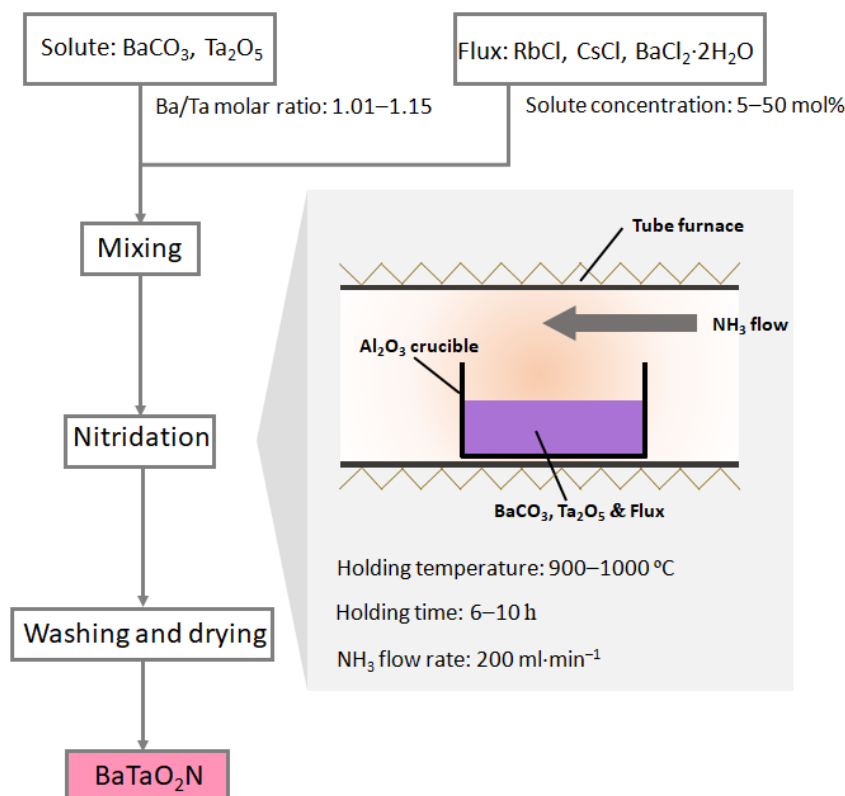
Figure 1. Synthetic route to the BaTaO$_2$N crystals.

Preparation of BaTaO$_2$N. BaCO$_3$ and Ta$_2$O$_5$ were used as the oxide precursors, while

RbCl, CsCl, and $BaCl_2 \cdot 2H_2O$ were employed as the fluxes. All chemicals were purchased from Wako Pure Chemical Industries, Ltd. and were used as received. In a typical procedure, the oxide precursors with a Ba/Ta molar ratio of 1.10 were mixed using the desired flux at a solute concentration of 10 mol%, where the solute concentration is defined as the molar ratio of $BaTaO_2N$ to the flux. An excess of barium was employed to compensate for barium volatilization during the high temperature nitridation process. Following manual mixing, the prepared mixtures (~2 g) were heated in an alumina crucible at 950 °C for 8 h under a flow of NH_3 (200 mL·min^{-1}), then cooled inside the tube furnace to 300 °C. Finally, the NH_3 was replaced with N_2 and the sample was cooled to 25 °C. To remove the remaining flux, the powders were washed with hot water and dried at 100 °C for 6 h. When $BaCl_2 \cdot 2H_2O$ was selected as the flux, a mixture of the oxide precursors and the flux with a solute concentration of 50 mol% also was employed. Hereafter, the RbCl, CsCl, and $BaCl_2 \cdot 2H_2O$-assisted samples will be referred to as BTON (RbCl), BTON (CsCl), and BTON ($BaCl_2$), respectively.

To investigate the effects of the various experimental parameters on the growth of $BaTaO_2N$ crystals using a RbCl flux, the oxide precursors ($BaCO_3$ and Ta_2O_5) with different Ba/Ta molar ratios (1.01−1.15) were mixed with the RbCl flux in a solute concentration range of 5–50 mol%. Similarly, the mixtures were nitrided at 900−1000 °C for 6−10 h under a flow of NH_3 (200 mL·min^{-1}), and then cooled to 25 °C after replacing NH_3 with N_2 at 300 °C (Figure 1).

The Photocatalytic Reaction. H_2 evolution was carried out using a gas-closed circulation system with a top-irradiation Pyrex reaction vessel. Prior to each reaction, the as-prepared $BaTaO_2N$ samples were loaded with a Pt (0.1 wt%) cocatalyst *via* the photodeposition method using an aqueous solution of $H_2PtCl_6 \cdot 6H_2O$ and CH_3OH (10 vol%). The resulting solution was evacuated twice to ensure the complete removal of air. This was followed by irradiation under visible light ($\lambda > 420$ nm) for 5 h through a cutoff filter from a 300-W Xe lamp. Subsequently, the reaction system was evacuated once again and the evolved H_2 gas was detected by online gas chromatography.

Material Characterization. X-ray diffraction (XRD) measurements were collected on a MiniFlex II powder diffractometer (Rigaku) with Cu Kα irradiation in the 2θ range of 10−80°. UV-vis diffuse reflectance spectroscopy (UV-vis DRS) was carried out using a JASCO V-670 spectrophotometer, and a $BaSO_4$ plate was applied as a reference to correct the baseline. A test step of 0.5 nm was employed in the 300−800 nm wavelength range. The chemical valence of Ta was characterized by X-ray photoelectron spectroscopy (XPS, JPS-9010MX, JEOL). The morphologies of the as-prepared samples were verified by field-emission scanning electron microscopy (FESEM; JSM-7600F, JEOL) with an operating acceleration voltage of 5 kV. The exposed dominant facets and the crystalline nature were recorded using transmission electron microscopy (TEM, JEM-2000EX-II, JEOL) and corresponding selected area electron diffraction (SAED) patterns, with an operating acceleration voltage of 200 kV. The quantities of Ba and Ta were determined using inductively coupled plasma atomic emission spectroscopy (ICP-AES, Thermo Fischer Scientific, iCAP 7600duo), while those of O and N were obtained using oxygen/nitrogen/hydrogen (ONH) analysis (LECO corporation, TCH600).

3. Results and discussion

Since selection of the flux reagent is one of the most important factors in influencing the morphology, size, and quality of the grown crystals, we initially examined the effects of different types of chloride flux for $BaTaO_2N$ crystal growth. Thus, Figure 2a shows the XRD patterns of the BaTaO2N crystals grown using RbCl, CsCl, and $BaCl_2 \cdot 2H_2O$ fluxes with solute concentrations of 10 mol% for RbCl and CsCl, and 50 mol% for $BaCl_2 \cdot 2H_2O$ (950 °C, 8 h). All diffraction peaks were assigned to the cubic perovskite $BaTaO_2N$ (ICDD PDF 01-084-1748) with the space group $Pm\bar{3}m$, indicating that single phase $BaTaO_2N$ crystals were successfully obtained. It should be noted here that when $BaCl_2 \cdot 2H_2O$ was used as the flux with a solute concentration of 10 mol% at 950 °C for 8 h, impurity phases such as Ta_3N_5, TaON, $Ba_5Ta_4O_{15}$, were observed (Figure 3). This can be accounted for by considering that the melting point of

$BaCl_2 \cdot 2H_2O$ is 962 °C higher than the heating temperature, and so the partially melted $BaCl_2 \cdot 2H_2O$ prevents efficient diffusion of the solutes. In other words, the excess unmelted $BaCl_2 \cdot 2H_2O$ acted as spacer and suppressed the growth of $BaTaO_2N$ crystals at a solute concentration of 10 mol%. Upon increasing the solute concentration to 50 mol%, pure phase $BaTaO_2N$ was obtained. We then compared the physical and chemical properties of the BTON (RbCl), BTON (CsCl), and BTON ($BaCl_2$) samples synthesized with solute concentrations of 10, 10, and 50 mol%, respectively. As shown in Figure 2b, the UV-vis DRS results indicated that all samples exhibited a visible absorption edge at ~660 nm, which was consistent with the photoabsorption characteristics of $BaTaO_2N$. In addition, the background absorption of BTON ($BaCl_2$) originating from the presence of reduced tantalum species or anionic vacancies was higher than those of BTON (RbCl) and BTON (CsCl). In the XPS spectra of Ta 4f (Figure 4), a higher density of reduced species Ta^{4+} was observed for BTON ($BaCl_2$) than for BTON (RbCl) and BTON (CsCl), implying that BTON ($BaCl_2$) contained the highest defect density among the prepared samples. Considering the differences in electronegativity between N and O, the binding energy between the Ta^{5+} and N^{3-} species was lower than that between the Ta^{5+} and O^{2-} species.[4]
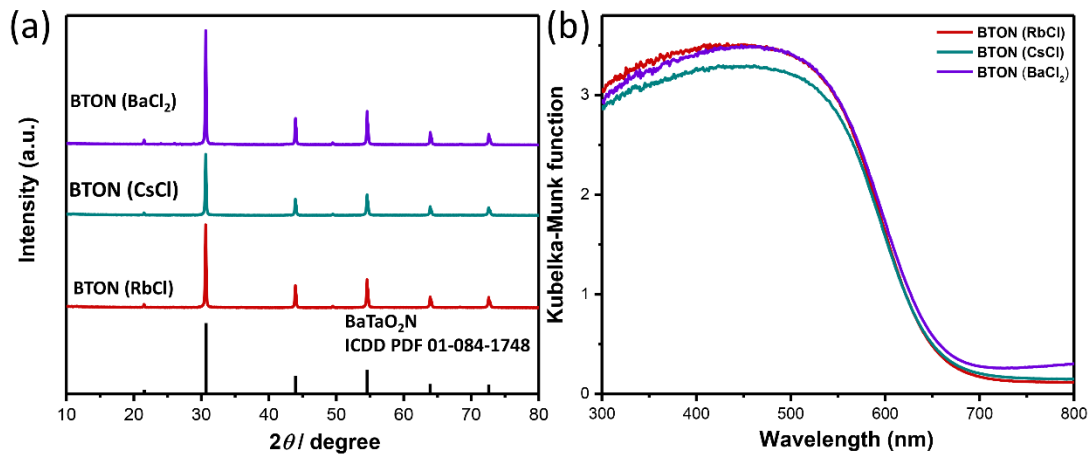
Figure 2. (a) XRD patterns and (b) UV-vis DRS spectra of BTON (RbCl), BTON (CsCl), and BTON ($BaCl_2$).

The morphology and crystallographic nature of each $BaTaO_2N$ sample prepared using the different chloride fluxes were further characterized by SEM, TEM, and

SAED. When RbCl and CsCl were employed, the BaTaO₂N crystals maintained a cubic structure (150−300 nm in size) despite slight edge truncation, and the dominant exposed facets were determined to be {100} facets (Figures 5a–f). No additional diffraction spots or diffuse streaks were observed in the SAED patterns, indicating that BTON (RbCl) and BTON (CsCl) were well-crystallized single crystals. However,
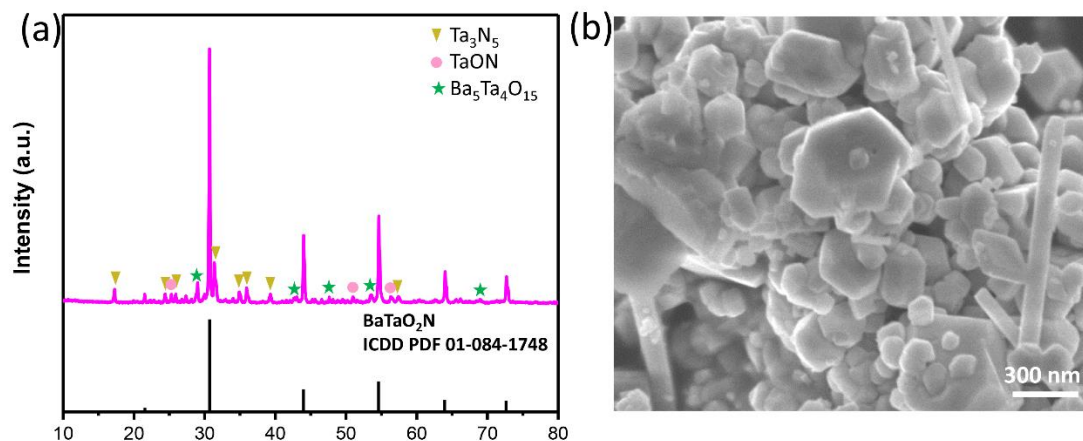

Figure 3. (a) XRD pattern and (b) SEM image of BTON (BaCl₂) prepared using a solute concentration of 10 mol%.

compared with BTON (RbCl), BTON (CsCl) exhibited a greater number of small steps at the edges. According to the bright-field TEM image and the corresponding SAED pattern of BTON (CsCl) (Figures 5e and 5f), the angles between two neighboring steps were right angles, which suggested that the main facets of these steps were the {100} facets. Interestingly, the BaTaO₂N crystals grown using BaCl₂·2H₂O differed in shape from those grown using RbCl and CsCl, although their sizes were similar (Figures 5g–5i). More specifically, the BTON (BaCl₂) particles presented a tetradecahedral shape surrounded by {111} and {100} facets. The clearly ordered diffraction spots, along with the [111] zone axis of the BTON (BaCl₂) crystal, indicated that BTON (BaCl₂) possessed a single crystalline nature.

The different morphologies of the BaTaO₂N crystals were attributed to the different fluxes inducing changes in the electrostatic forces among the precursor particles during the growth process, in analogy to the case previously described for LaTaON₂.[25] More specifically, the flux exhibits an ionic state at higher temperatures, in which the cations and anions are adsorbed on the surfaces of the precursor particles to

form an electric double layer between the precursor particles and the molten salts. Cl⁻ anions exhibit a larger negative adsorption energy than the alkali cations, resulting in their more facile adsorption on the surface, which induces a negative surface charge on $BaTaO_2N$. These surface negative charges are then neutralized by the adsorption of alkali cations on the surface. The strength of the repulsion force between the particles due to the surface negative charges is therefore determined by the amount of adsorbed alkali cations. However, the adsorption energy of the alkali cation decreases as the size of the alkali cation increases, implying that smaller cations can be adsorbed more easily on the $BaTaO_2N$ surface to decrease the repulsion force and promote the aggregation of
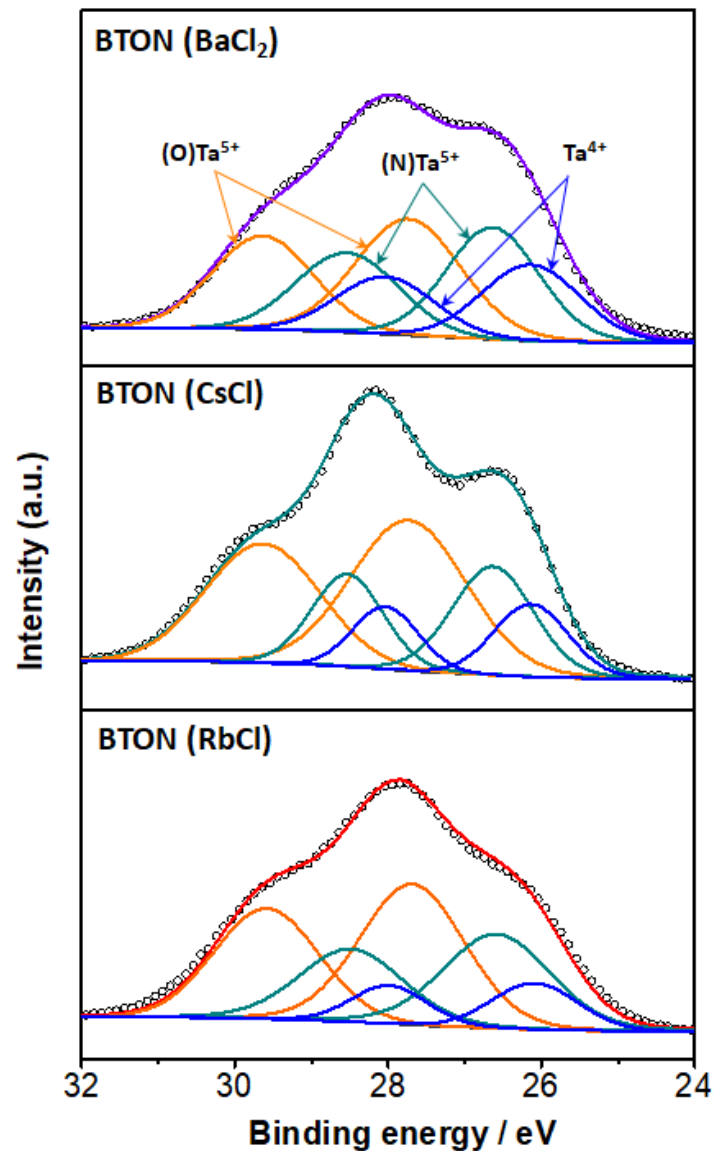
Figure 4. Ta 4f XPS spectra of BTON (RbCl), BTON (CsCl), and BTON (BaCl₂).

BaTaO$_2$N particles. As Cs$^+$ (0.18 nm) is slightly larger than Rb$^+$ (0.17 nm), the BaTaO$_2$N particles grown in the CsCl flux have a greater repulsion force than those grown in the RbCl flux. This increased repulsion force will suppress aggregation of the BaTaO$_2$N particles, leading to the formation of additional edge steps in the BTON (CsCl) samples. In the case of the BTON (BaCl$_2$) samples, the Ba^{2+} cations (0.16 nm) are smaller than both Rb$^+$ (0.17 nm) and Cs$^+$ (0.18 nm), thereby resulting in increased Ba^{2+} cation adsorption on the surfaces of the BaTaO$_2$N particles. However, as barium is one of the constituent elements of BaTaO$_2$N, excess Ba^{2+} adsorption on the surfaces of the growing BaTaO$_2$N particles can affect the atomic arrangement of the BaTaO$_2$N, resulting in the exposure of different crystal facets.
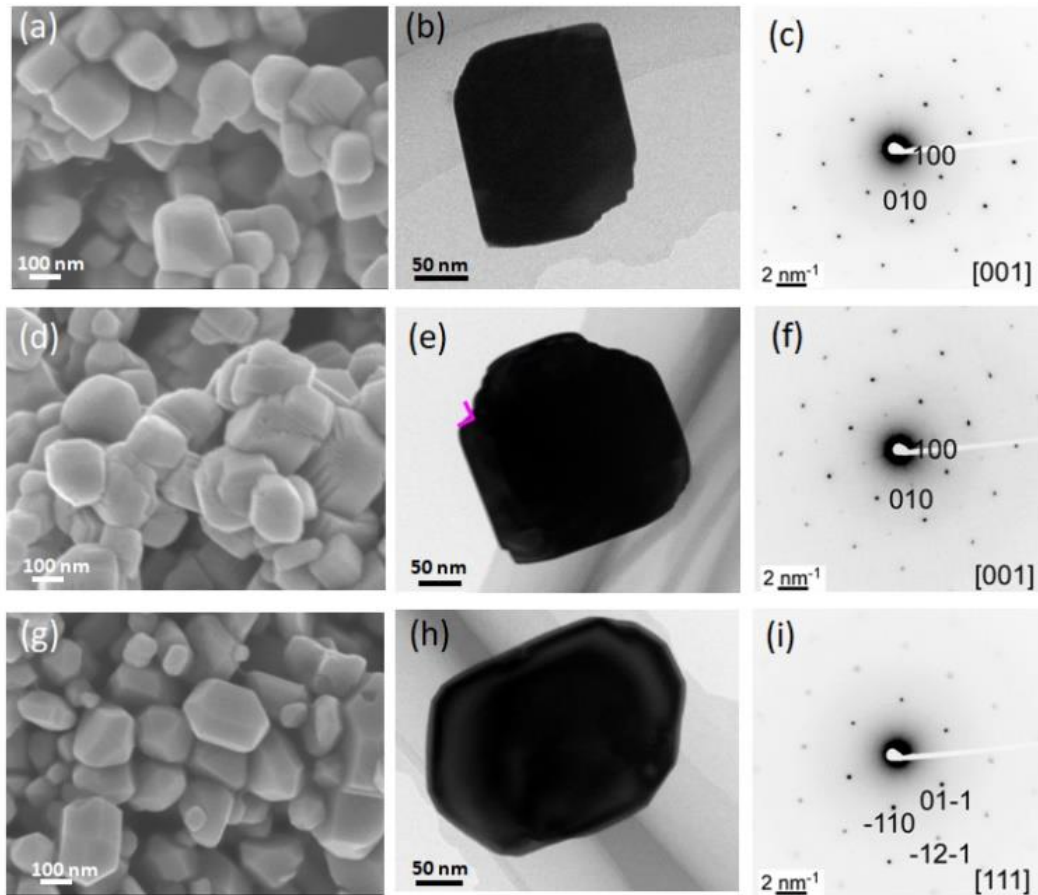
Figure 5. SEM images, TEM images, and SAED patterns of (a, b, c) BTON (RbCl), (d, e, f) BTON (CsCl), and (g, h, i) BTON (BaCl$_2$). The pink arrow in part (e) indicates the right angle between two neighboring steps.
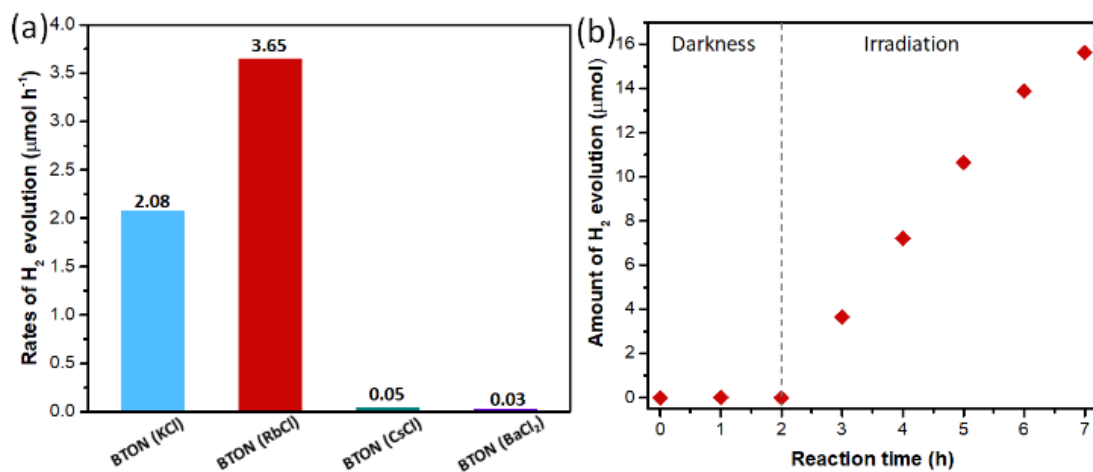
Figure 6. (a) H_2 evolution rates of BTON (KCl), BTON (RbCl), BTON (CsCl), and BTON (BaCl$_2$). (b) Quantity of H_2 evolved upon increasing the reaction time for BTON (RbCl) initially in the absence of light and later under irradiation. Reaction conditions: 0.1 wt% Pt-modified BTON 0.1 g; ultrapure water 150 mL; 10 vol% CH$_3$OH; 300-W Xe lamp ($\lambda > 420$ nm). The H_2 evolution rate of BTON (KCl) is adapted with permission from REF.24.

The photocatalytic evolution of H_2 on the various BaTaO$_2$N samples prepared using different fluxes was then examined under visible light irradiation ($\lambda > 420$ nm) using Pt nanoparticles as the reduction cocatalysts and CH$_3$OH as the sacrificial reagent. The results are presented in Figure 6a. It should be noted that the rate of H_2 evolution over BTON (KCl) was also compared here with the permission of REF.24, since KCl has been demonstrated to be a suitable flux for the growth of BaTaO$_2$N crystals with a high photocatalytic performance for H_2 evolution. Thus, as indicated, the BTON (RbCl) sample showed a higher photocatalytic activity than the BTON (KCl), BTON (CsCl), and BTON (BaCl$_2$) samples. The typical time course of H_2 evolution over BTON (RbCl) is shown in Figure 6b. In the absence of light, no photocatalytic activity for H_2 evolution was detected due to the lack of light excitation resulting in the necessary generation of electrons to drive the H_2 evolution. In contrast, upon irradiation, the amount of evolved H_2 increased almost linearly with the reaction time, indicating a good photocatalytic stability. In addition, elemental analysis was carried out to evaluate the chemical compositions of these samples. As outlined in Table 1, the atomic ratio of

BTON (RbCl) was closest to the theoretical value, while BTON (BaCl$_2$) showed insufficient nitridation and the absence of tantalum in the lattice. These results indicated that BTON (RbCl) had fewer defects that could act as trapping centers,[26,27] in addition to a higher crystallinity to allow efficient photocatalytic reactions to take place; this is consistent with the UV-vis DRS results presented in Figure 2b. As such, RbCl was determined to be the preferred chloride flux for the growth of BaTaO$_2$N crystals exhibiting a high photocatalytic performance.

Table 1. Elemental analyses of BTON (KCl), BTON (RbCl), BTON (CsCl), and BTON (BaCl$_2$) (atomic ratio)

Sample	Ba	Ta	O[a]	N[a]	Sum	Ba/Ta	O/N
BTON (KCl)	0.93	0.96	2.04	0.96	4.89	0.97	2.12
BTON (RbCl)	1.01	1.03	2.03	0.97	5.04	0.98	2.08
BTON (CsCl)	0.98	1.00	2.04	0.96	4.98	0.99	2.11
BTON (BaCl$_2$)	1.00	0.87	2.19	0.81	4.86	1.15	2.73
BTON (theoretical)	1.00	1.00	2.00	1.00	5.00	1.00	2.00

[a]The sum of O and N has been normalized to be 3.00.

In addition, the growth conditions, including the Ba/Ta molar ratio of the source materials, the solute concentration, the reaction temperature, and the reaction time, were found to have a significant influence on the crystallinity and morphology of BTON (RbCl). We initially examined the effect of the Ba/Ta molar ratio, where Figures 7 and 8 present the XRD patterns and SEM images of BTON (RbCl) prepared by nitridation of the mixtures of BaCO$_3$ and Ta$_2$O$_5$ powders at different Ba/Ta molar ratios (1.01−1.15), while maintaining a solute concentration, holding temperature, and holding time of 10 mol%, 950 °C, and 8 h, respectively. When the Ba/Ta molar ratio was <1.10, although perovskite BaTaO$_2$N was the major product, a small number of Ta$_3$N$_5$ byproducts were also clearly observed. In contrast, no secondary phase was detected in the samples prepared using Ba/Ta ratios ≥1.10. According to the SEM images (Figure 8), undeveloped BaTaO$_2$N particles consisting of some rod-like shapes were observed at lower Ba/Ta molar ratios (1.01 and 1.05), while only homogeneous

cubic BaTaO$_2$N particles were obtained at higher Ba/Ta molar ratios (1.10 and 1.15). These results indicate that a suitable excess of BaCO$_3$ could compensate for the loss of barium through volatilization during the high temperature nitridation process,[28] which was beneficial to the growth of BaTaO$_2$N crystallites.
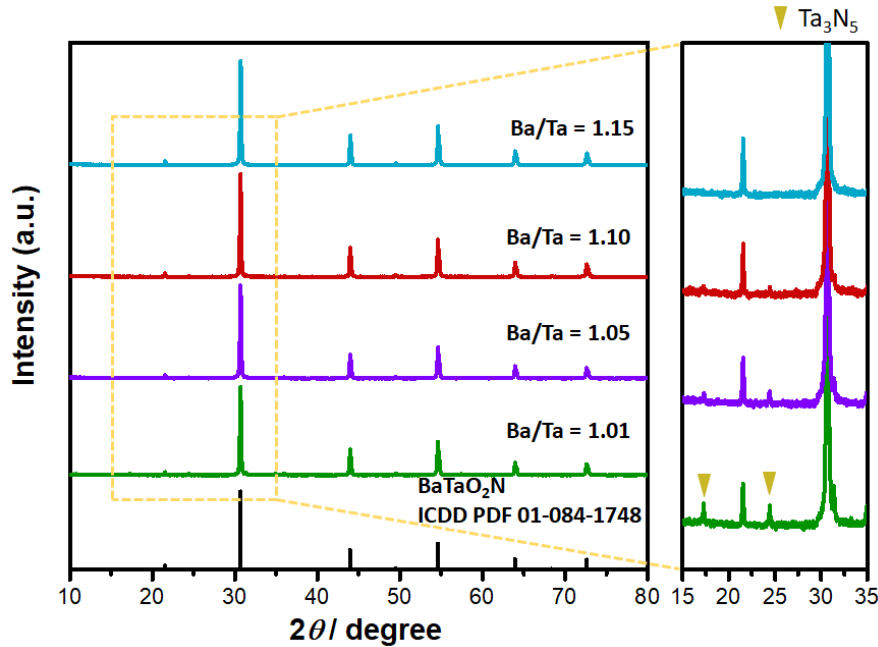

Figure 7. XRD patterns of BTON (RbCl) prepared using Ba/Ta molar ratios of 1.01, 1.05, 1.10, and 1.15.

Subsequently, the effect of the solute concentration (1−50 mol%) on the growth of BTON (RbCl) crystals with a Ba/Ta molar ratio of 1.10 at 950 °C for 8 h was studied. The XRD patterns of BTON (RbCl) crystals prepared using different solute concentrations are presented in Figure 9. At 5 mol%, the main diffraction peaks were indexed as the BaTaO$_2$N phases, with some minor diffraction peaks also being assigned to Ta$_3$N$_5$ impurity phases. Upon increasing the solute concentration (10−50 mol %), the impurity phases disappeared, and strong diffractions peaks were observed at a solute concentration of 10 mol%. Figure 10 shows the SEM images of the BTON (RbCl) crystals prepared using different solute concentrations. As shown, cubic-like BaTaO$_2$N crystals with clear edges and a homogeneous crystal size were observed at solute concentrations of 5 and 10 mol%, while some rod-like impurities were observed at a solute concentration of 5%. Upon increasing the solute concentration beyond 10 mol%,

the BaTaO₂N crystals gradually became irregularly shaped due to the stronger diffusion barrier of the solute in the solvent. These results suggested that an appropriate solute concentration for the growth of BaTaO₂N from a RbCl flux is 10 mol%.
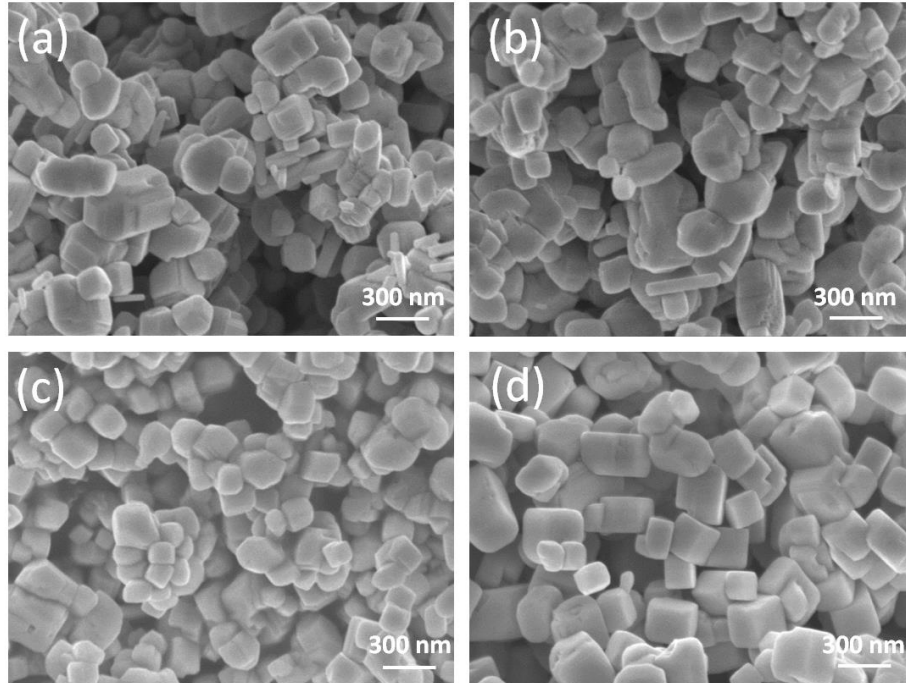

Figure 8. SEM images of BTON (RbCl) prepared using Ba/Ta molar ratios of (a) 1.01, (b) 1.05, (c) 1.10, and (d) 1.15.
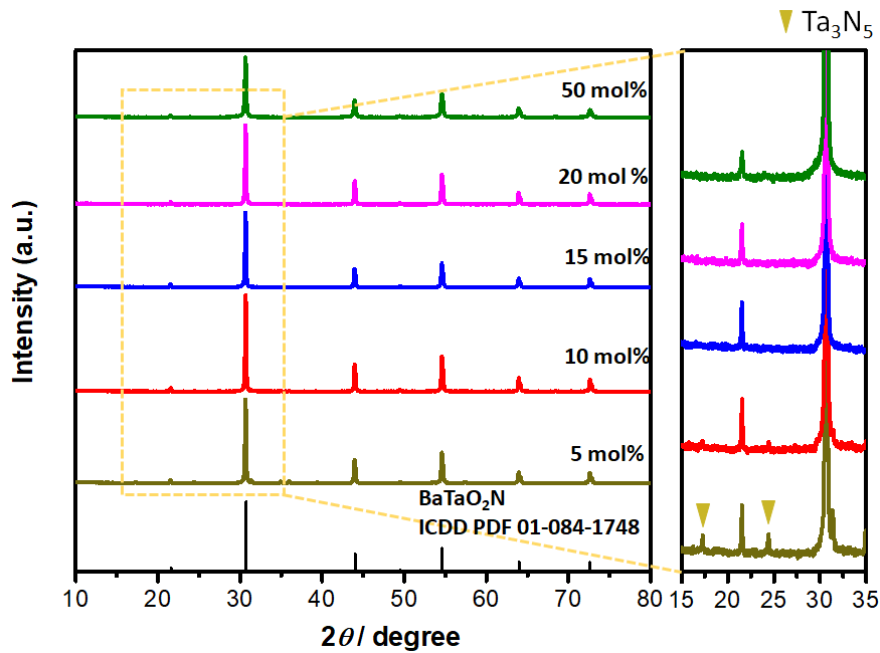

Figure 9. XRD images of BTON (RbCl) prepared using solute concentrations of 5, 10, 15, 20, and 50 mol%.

We subsequently investigated the effect of the holding temperature and time on the growth of BTON (RbCl) crystals. Figure 11 and 12 show the XRD patterns and SEM images, respectively, of the BTON (RbCl) crystals prepared using different holding temperatures with a solute concentration of 10 mol% and a Ba/Ta molar ratio of 1.10 for 8 h. These crystals exhibited similar diffraction patterns and morphologies with the exception of those prepared at 900 °C, in which weaker diffraction peaks and some idiomorphic irregular shapes were observed due to insufficient nitridation. The UV-vis DRS of the BTON (RbCl) crystals prepared using different holding temperatures are shown in Figure 13. All samples exhibited a visible absorption edge at ~660 nm, while
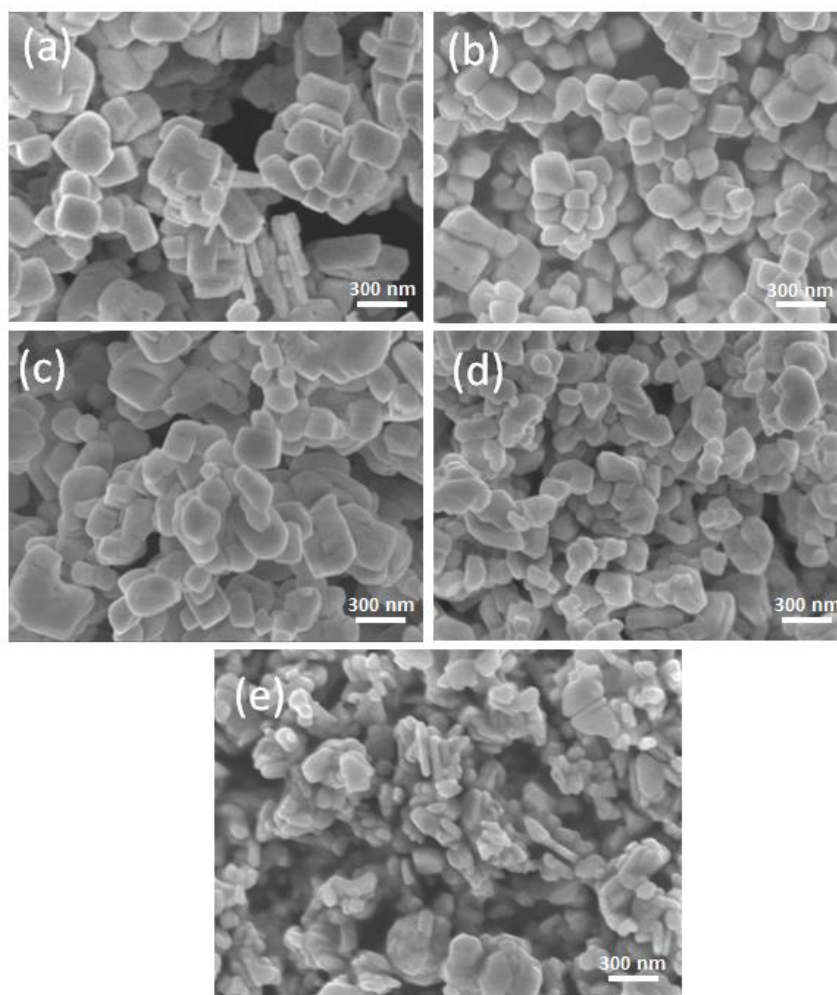
Figure 10. SEM images of BTON (RbCl) prepared using solute concentrations of (a) 5, (b) 10, (c) 15, (d) 20, and (e) 50 mol%.

the background absorption of BTON (RbCl) prepared at 950 °C was lower than those prepared at 900 and 1000 °C. In addition, XPS analysis (Figure 14) showed that the

density of the reduced Ta^{4+} species in BTON (RbCl) prepared at 950 °C was lower than those of the corresponding samples prepared at 900 and 1000 °C, thereby implying that the BTON (RbCl) prepared at 950 °C contained the fewest number of defects. This is likely due to the fact that increasing the temperature from 900 to 950 °C led to sufficient nitridation, thereby decreasing the number of defects. In addition, the hydriding species produced along with the nitriding species upon the dissociation of NH_3 gas resulted in the reduction of some Ta^{5+} at higher temperatures (1000 °C), while the increased vapor pressure or flux decomposition caused by such high temperatures resulted in the formation of nitrogen defects.[29] It was therefore apparent that the $BaTaO_2N$ crystals function more effectively at 950 °C.
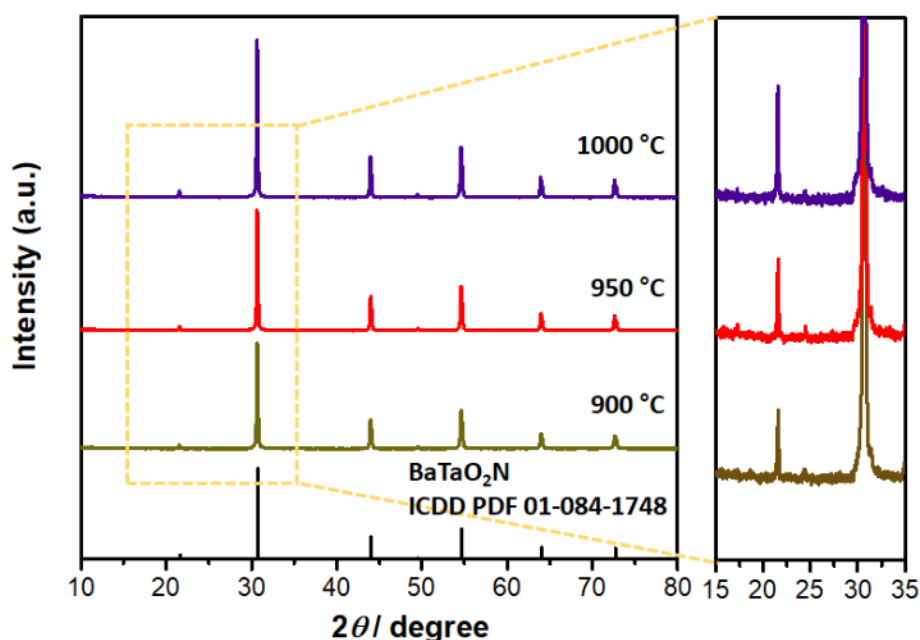
Figure 11. XRD patterns of BTON (RbCl) prepared using holding temperatures of 900, 950, and 1000 °C.
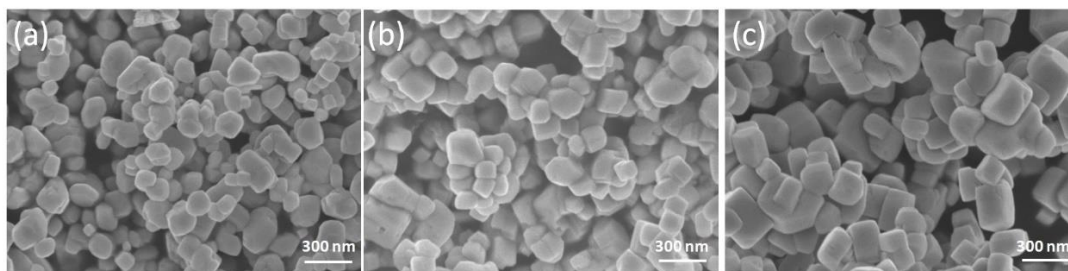

Figure 12. SEM images of BTON (RbCl) prepared using holding temperatures of (a) 900, (b) 950, and (c) 1000 °C.

65
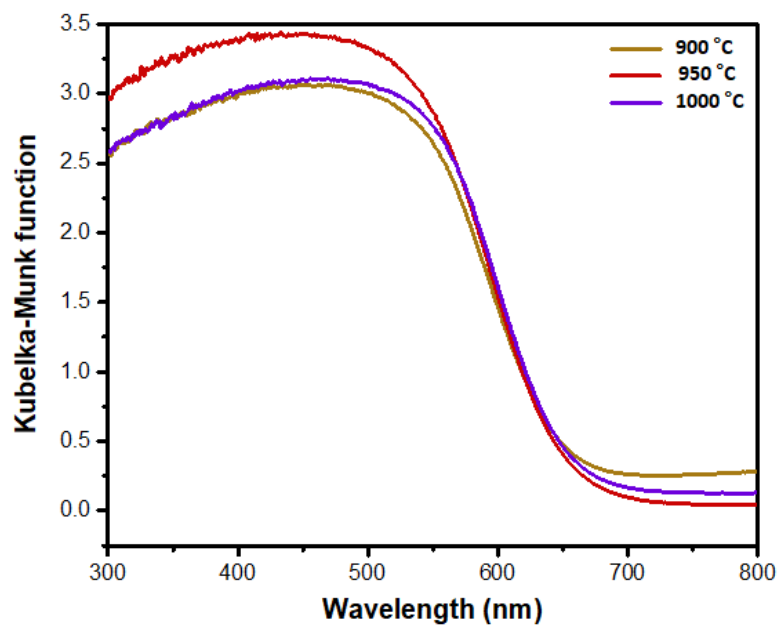
**Figure 13.** UV-vis DRS of BTON (RbCl) prepared using holding temperatures of 900, 950, and 1000 °C.
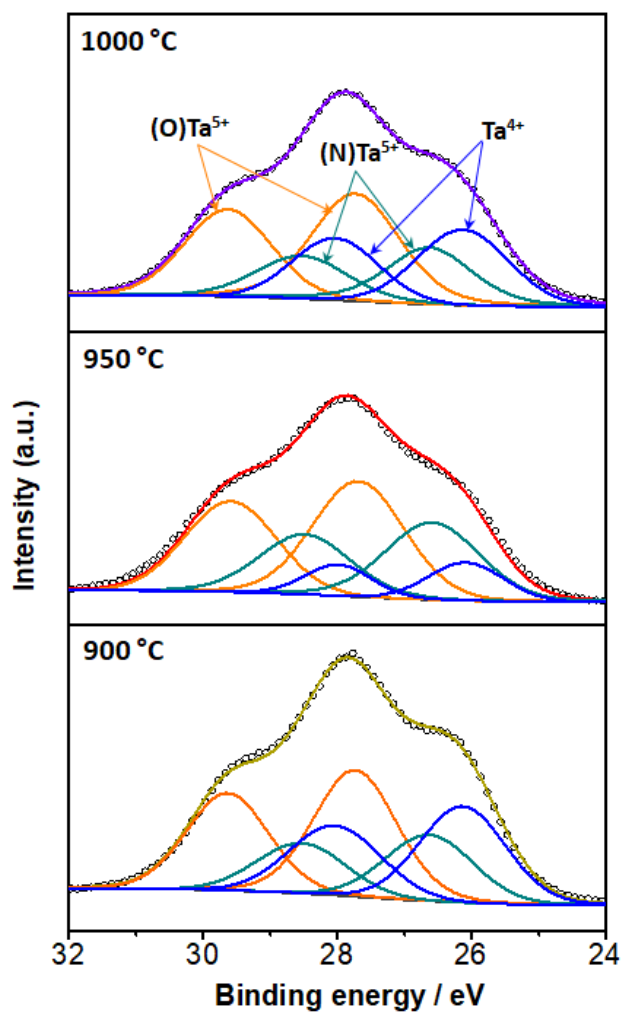
Figure 14. Ta 4f XPS spectra of BTON (RbCl) prepared using holding temperatures of 900, 950, and 1000 °C.

Finally, we studied the growth of $BaTaO_2N$ crystals at 950 °C with different holding times, a solute concentration of 10 mol%, and a Ba/Ta molar ratio of 1.10. As shown in Figure 15, all diffraction patterns were assigned to the $BaTaO_2N$ phase. Upon comparison of the $BaTaO_2N$ crystals grown over 6, 8, and 10 h, the diffraction peaks were more intense for the $BaTaO_2N$ crystals grown for 8 h, indicating a higher crystallinity. The holding time was found to have no significant impact on the morphologies of the $BaTaO_2N$ crystals compared to those observed in the previous experiments (Figure 16).
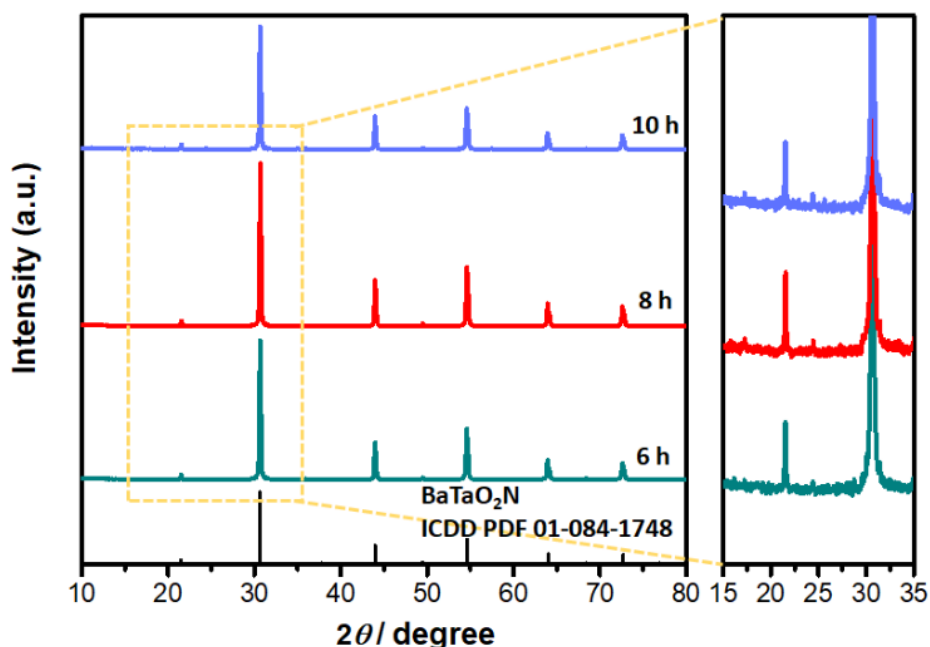

Figure 15. XRD patterns of BTON (RbCl) prepared using holding times of 6, 8, and 10 h.
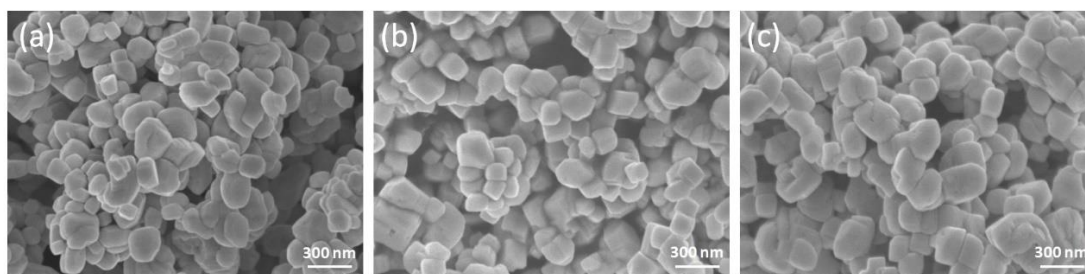
Figure 16. SEM images of BTON (RbCl) prepared using holding times of (a) 6, (b) 8, and (c) 10 h.

4. Conclusion

We herein investigated the crystal growth of $BaTaO_2N$ using a range of chloride fluxes, and subsequently determined the effect of the flux type (i.e., RbCl, CsCl, or $BaCl_2 \cdot 2H_2O$) on the morphology, crystallinity, and photocatalytic performance of the $BaTaO_2N$ crystals. An excellent photocatalytic performance was obtained for H_2 evolution over BTON (RbCl) due to the lower defect density and higher crystallinity. Upon optimization of the experimental parameters, the pure phase BTON (RbCl) crystals with homogenous cubic shapes and a high crystallinity were directly fabricated using a Ba/Ta molar ratio of 1.10 (or 1.15) and a solute concentration of 10 mol% at 950 °C for 8 h under an NH_3 atmosphere. These results are of importance since they indicate that the use of different chloride fluxes and optimization of the reaction conditions can improve the crystallinity and morphology of $BaTaO_2N$ crystals for H_2 evolution, and to ultimately convert abundant solar energy into renewable, clean, and storable energy.

Moreover, in our recent studies, we found that the highly crystalized BTON (RbCl) also play a pivotal role in achieving high photocatalytic activity for Z-scheme water splitting under visible light irradiation. An effective sequential deposition of Pt nanoparticles was utilized to deal with BTON (RbCl) particulate photocatalyst, involving an impregnation-reduction pre-treatment and a subsequent photo-deposition process. In the impregnation-reduction process, uniformly dispersed Pt seeds form an intimate contact with $BaTaO_2N$. Subsequently, photo-deposition allows Pt nanoparticles to uniformly grow at the numerous active Pt seeds. Because of the uniform distribution of Pt cocatalysts and the high crystallinity, Pt-located BTON (RbCl) exhibited a good photocatalytic activity for H_2 evolution from an aqueous methanol solution and Z-scheme water splitting constructed with WO_3.

5. References

(1) Hitoki, G.; Takata, T.; Kondo, J. N.; Hara, M.; Kobayashi, H.; Domen, K. An Oxynitride, TaON, as an Efficient Water Oxidation Photocatalyst under Visible Light Irradiation (λ < 500 nm). *Chem. Commun*. **2002**, *16*, 1698–1699.

(2) Wang, Z.; Inoue, Y.; Hisatomi, T.; Ishikawa, R.; Wang, Q.; Takata, T.; Chen, S.; Shibata, N.; Ikuhara, Y.; Domen, K. Overall Water Splitting by Ta_3N_5 Nanorod Single Crystals Grown on the Edges of $KTaO_3$ Particles. *Nature Catal.* **2018**, *1*, 756–763.

(3) Takata, T.; Hitoki, G.; Kondo, J. N.; Hara, M.; Kobayashi, H.; Domen, K. Visible-Light-Driven Photocatalytic Behavior of Tantalum-Oxynitride and Nitride. *Res. Chem. Inter.* **2007**, *33*, 13–25.

(4) Wang, X.; Hisatomi, T.; Wang, Z.; Song, J.; Qu, J.; Takata, T.; Domen K. Core–Shell-Structured $LaTaON_2$ Transformed from $LaKNaTaO_5$ Plates for Enhanced Photocatalytic H_2 Evolution. *Angew. Chem.* **2019**, *131*, 1–6.

(5) Zhong, Y.; Li, Z.; Zhao, X.; Fang, T.; Huang, H.; Qian, Q.; Chang, X.; Wang, P.; Yan, S.; Yu, Z.; Zou, Z. Enhanced Water-Splitting Performance of Perovskite $SrTaO_2N$ Photoanode Film through Ameliorating Interparticle Charge Transport. *Adv. Funct. Mater*. **2016**, *26*, 7156–7163.

(6) Wang, Z.; Li, C.; Domen, K. Recent Developments in Heterogeneous Photocatalysts for Solar-Driven Overall Water Splitting. *Chem. Soc. Rev.* **2019**, *48*, 2109–2125.

(7) Fang, M.; De Wijs, G. A.; Orhan, E.; De With, G.; De Groot, R. A.; Hintzen, H. T.; Marchand, R. Local Structure and Electronic Properties of $BaTaO_2N$ with Perovskite-Type Structure. *J. Phys. Chem. Solids.* **2003**, *64*, 281–286.

(8) Fuertes, A. Metal Oxynitrides as Emerging Materials with Photocatalytic and Electronic Properties. *Mater. Horiz.* **2015**, *2*, 453–461.

(9) Chun, W. J.; Ishikawa, A.; Fujisawa, H.; Takata, T.; Kondo, J. N.; Hara, M.; Kawai, M.; Matsumoto, Y.; Domen, K. Conduction and Valence Band Positions of Ta_2O_5,

TaON, and Ta$_3$N$_5$ by UPS and Electrochemical Methods. *J. Phys. Chem. B* **2003**, *107*, 1798–1803.

(10) Balaz, S.; Porter, S. H.; Woodward, P. M.; Brillson, L, J. Electronic Structure of Tantalum Oxynitride Perovskite Photocatalysts. *Chem. Mater.* **2013**, *25*, 3337−3343.

(11) Wang, C.; Hisatomi, T.; Minegishi, T.; Wang, Q.; Zhong, M.; Katayama, M.; Kubota, J.; Domen, K. Synthesis of Nanostructured BaTaO$_2$N Thin Films as Photoanodes for Solar Water Splitting. *J. Phys. Chem. C* **2016**, *120*, 15758−15764.

(12) Dong, B.; Qi, Y.; Cui, J.; Liu, B.; Xiong, F.; Jiang, X.; Li, Z.; Xiao, Y.; Zhang, F.; Li, C. Synthesis of BaTaO$_2$N Oxynitride from Ba-Rich Oxide Precursor for Construction of Visible-Light-Driven Z-Scheme Overall Water Splitting. *Dalton Trans.*, **2017**, *46*, 10707–10713.

(13) Ebbinghaus, S. G.; Abicht, H. P.; Dronskowski, R.; Muller, T.; Reller, A.; Weidenkaff, A. Perovskite-Related Oxynitrides-Recent Developments in Synthesis, Characterisation and Investigations of Physical Properties. *Prog. Solid State Chem.* **2009**, *37*, 173–205.

(14) Wang, Y.; Jin, S.; Pan, G.; Li, Z.; Chen, L.; Liu, G.; Xu, X. Zr Doped Mesoporous LaTaON$_2$ for Efficient Photocatalytic Water Splitting. *J. Mater. Chem. A* **2019**, *7*, 5702–5711.

(15) Maeda, K.; Domen, K. New Non-Oxide Photocatalysts Designed for Overall Water Splitting under Visible Light. *J. Phys. Chem. C* **2007**, *111*, 7851–7861.

(16) Kodera, M.; Urabe, H.; Katayama, M.; Hisatomi, T.; Minegishi, T.; Domen, K. Effects of Flux Synthesis on SrNbO$_2$N Particles for Photoelectrochemical Water Splitting. *J. Mater. Chem. A*, **2016**, *4*, 7658–7664.

(17) Kawashima, K.; Hojamberdiev, M.; Wagata, H.; Yubuta, K.; Vequizo, J. J. M.; Yamakata, A.; Oishi, S.; Domen, K.; Teshima, K. NH$_3$-Assisted Flux-Mediated Direct Growth of LaTiO$_2$N Crystallites for Visible-Light-Induced Water Splitting. *J. Phys. Chem. C* **2015**, *119*, 15896−15904.

(18) Kim, Y. Effects of KCl Flux on the Morphology, Anion Composition, and Chromaticity of Perovskite Oxynitrides, $CaTaO_2N$, $SrTaO_2N$, and $LaTaON_2$. *Ceram. International* **2014**, *40*, 5275–5281.

(19) Zhang, L.; Song, Y.; Feng, J.; Fang, T.; Zhong, Y.; Li, Z.; Zou, Z. Photoelectrochemical Water Oxidation of $LaTaON_2$ under Visible-Light Irradiation. *Int. J. Hydrogen Energy* **2014**, *39*, 7697–7704.

(20) Kodera, M.; Katayama, M.; Hisatomi, T.; Minegishi, T.; Domen, K. Effects of Flux Treatment on Morphology of Single-Crystalline $BaNbO_2N$ Particles. *CrystEngComm*, **2016**, *18*, 3186–3190.

(21) Bugaris, D. E.; Zur Loye, H. C. Materials Discovery by Flux Crystal Growth: Quaternary and Higher Order Oxides. *Angew. Chem. Int. Ed.* **2012**, *51*, 3780–3811.

(22) Park, N. Y.; Kim, Y. Morphology and Band Gap Variations of Oxynitride $LaTaON_2$ Depending on the Ammonolysis Temperature and Precursor. *J. Mater. Sci*. **2012**, *47*, 5333–5340.

(23) Yamada, T.; Murata, Y.; Wagata, H.; Yubuta, K.; Teshima, K. Facile Morphological Modification of $Ba_5Nb_4O_{15}$ Crystals Using Chloride Flux and in Situ Growth Investigation. *Cryst. Growth Des*. **2016**, *16*, 3954−3960.

(24) Luo, Y.; Suzuki, S.; Wang, Z.; Yubuta, K.; Vequizo, J. J. M.; Yamakata, A.; Shiiba, H.; Hisatomi, T.; Domen, K.; Teshima, K. Construction of Spatial Charge Separation Facets on $BaTaO_2N$ Crystals by Flux Growth Approach for Visible-Light-Driven H_2 Production. *ACS Appl. Mater. Interfaces* **2019**, *11*, 22264−22271.

(25) Zhou, J.; Zhou, C.; Shi, Z.; Xu, Z.; Yan, S.; Zou. Z. Oriented Attachment Growth of Hundred-Nanometer-Size $LaTaON_2$ Single Crystal in Molten Salts for Enhanced Photoelectrochemical Water Splitting. *J. Mater. Chem. A* **2018**, *6*, 7706–7713.

(26) Xue, J.; Fujitsuka, M.; Majima, T. The Role of Nitrogen Defects in Graphitic Carbon Nitride for Visible-Light-Driven Hydrogen Evolution. *Phys. Chem. Chem.*

Phys. **2019**, *21*, 2318–2324.

(27) Xue, J.; Fujitsuka, M.; Majima, T. Shallow Trap State-Induced Efficient Electron Transfer at the Interface of Heterojunction Photocatalysts: The Crucial Role of Vacancy Defects. *ACS Appl. Mater. Interfaces* **2019**, *11*, 40860−40867.

(28) Hisatomi, T.; Katayama, C.; Teramura, K.; Takata, T.; Moriya, Y.; Minegishi, T.; Katayama, M.; Nishiyama, H.; Yamada, T.; Domen, K. The Effects of Preparation Conditions for a $BaNbO_2N$ Photocatalyst on Its Physical Properties. *ChemSusChem* **2014**, *7*, 2016−2021.

(29) Higashi, M.; Abe, R.; Takata, T.; Domen, K. Photocatalytic Overall Water Splitting under Visible Light Using $ATaO_2N$ (A = Ca, Sr, Ba) and WO_3 in a IO_3^-/I^- Shuttle Redox Mediated System. *Chem. Mater.* **2009**, *21*, 1543–1549.

Chapter 3. Platy BaTaO₂N Crystals Fabricated from K₂CO₃–KCl Binary Flux for Photocatalytic H₂ Evolution

1. Introduction

Shape-controlled syntheses of inorganic single crystals play a crucial role in the determination of their physical and chemical properties.[1–3] In particular, the design and discovery of photocatalysts with desirable shapes have become an important strategy to effectively harvest incident light, expose active facets, and accelerate charge separation and transfer, thereby maximizing their photocatalytic water splitting performance.[4–7] According to the principles of crystal growth, the crystal shape is determined not only by the thermodynamic factors, in which the most stable crystal product is formed with the minimized total interfacial free energy of a system, but also by the kinetic factors, which limit the growth process by generating barriers such as decomposition, diffusion, and rearrangement of ions in the starting materials. Therefore, many studies have focused on the controllable growth of particulate photocatalysts to form a unique shape with better performance.[8,9] Unconventional TiO_2 crystals with a curved surface were successfully prepared using synergistic organic-inorganic capping agents, and it exhibited a higher photocatalytic performance than the conventional faceted TiO_2 crystals.[10] The design of CdS photocatalysts with nanorod structures *via* a one-pot solvothermal method significantly improved the H_2-evolution activity when compared with CdS nanoparticles.[11] Crystalline carbon nitride nanosheets with an inherent 2-dimensional crystal structure prepared by a sonication-centrifugation process showed significantly enhanced photocatalytic activity for H_2 generation.[12] However, the relationship between the morphology and the photocatalytic performance based on narrow band-gap photocatalysts especially for the (oxy)nitride materials with the intense wide-range visible light harvest is rarely reported.[13,14]

Perovskite-type (oxy)nitride $BaTaO_2N$ is a promising photocatalyst that has gained considerable attention for its ability to convert solar energy into chemical fuel

H$_2$. This is because BaTaO$_2$N has a narrow band gap that can utilize visible light up to 660 nm and a band edge position that is suitable for the reduction and oxidation reaction of water.[15,16] However, compared with other oxide materials, it is more difficult to control the morphology of BaTaO$_2$N owing to the harsh syntheses conditions that require a high temperature and involve an ammonia flow. BaTaO$_2$N has been fabricated *via* traditional solid-state reaction, hydrothermal, polymerized complex, and flux methods.[17–20] However, most of the prepared BaTaO$_2$N crystals were aggregated particles that contained many defects due to the rearrangement of metal ions and the diffusion and replacement of nitrogen atoms during the nitridation process. High-quality BaTaO$_2$N crystals with well-developed {100} facets were obtained using the flux method, in which an alkali chloride was employed as the solvent to reduce the diffusion resistance of the solutes for crystallization. Nevertheless, the main shape of BaTaO$_2$N is still cubic because BaTaO$_2$N belongs to the cubic system and has a highly symmetric lattice. It has been reported that the plate-like structure of photocatalyst materials could decrease the charge carrier diffusion distance from the bulk to the surface, thus promoting the photo-excited charge separation and transfer towards efficient photocatalytic reactions.[21] Therefore, plate-like structured BaTaO$_2$N crystals that are well crystallized are expected to be explored and so are their photocatalytic performances for H$_2$ evolution.

A few studies noted that the combination of two kinds of flux (binary flux) with different properties can tailor the crystal morphology, which has inspired us to employ suitable binary flux in the nitridation process to control the particulate structure of the BaTaO$_2$N crystals.[22–24] In the current study, we focus on the fabrication of platy BaTaO$_2$N crystals with a lower defect density and higher crystallinity by simply varying the molar ratio of K$_2$CO$_3$/KCl during the nitridation process. Subsequently, the formation mechanisms of the platy BaTaO$_2$N crystals and the effects of the K$_2$CO$_3$/KCl molar ratio on the photocatalytic activity for H$_2$ evolution were investigated.

2. Experimental section

Preparation of BaTaO₂N crystals. Oxynitride BaTaO$_2$N crystals were directly grown from K$_2$CO$_3$–KCl binary flux during the nitridation process. BaCO$_3$, Ta$_2$O$_5$, K$_2$CO$_3$, and KCl were purchased from Wako Pure Chemical Industries, Ltd., and used as received without further purification. Typically, stoichiometric mixtures of Ba$_2$CO$_3$ and Ta$_2$O$_5$ were mixed with K$_2$CO$_3$–KCl binary flux at a solute concentration of 10 mol.%, in which the solute concentration was defined as a molar ratio of BaTaO$_2$N to that of the sum of BaTaO$_2$N and K$_2$CO$_3$–KCl binary flux, and the molar ratio of K$_2$CO$_3$/KCl was varied within a range of 5/95 to 50/50. The mixtures (~2 g) were then placed in an alumina crucible and heated to 950 °C at a rate of 10 °C·min^{-1}. They were subsequently held at this temperature for 8 h in an NH$_3$ atmosphere with an NH$_3$ flow rate of 200 ml·min^{-1}. Afterward, the crucible was naturally cooled to 300 °C in an NH$_3$ atmosphere and then cooled to room temperature in a N$_2$ atmosphere. The obtained powders were immersed in hot water to remove the residual flux and then dried at 100 °C for 4 h. Hereafter, the samples grown from different molar ratios of K$_2$CO$_3$/KCl were denoted as BTON (5/95), BTON (10/90), BTON (20/80), BTON (30/70) and BTON (50/50). For comparison, BaTaO$_2$N was also prepared through a solid-state reaction, single K$_2$CO$_3$, and single KCl flux with a solute concentration of 10 mol.% under the same heat-treatment conditions, which were hereafter denoted as BTON (SSR), BTON (KCO), and BTON (KCl), respectively. To investigate the formation mechanisms of the platy BaTaO$_2$N crystals, similar samples were prepared at 750−950 °C for 0−8 h using K$_2$CO$_3$/KCl binary flux with a molar ratio of 20/80 in an NH$_3$ atmosphere with an NH$_3$ flow rate of 200 ml·min^{-1}.

Photocatalytic H₂ production. The photocatalytic H$_2$ evolution reaction on the BaTaO$_2$N crystals was tested after Pt modification by the impregnation method. Firstly, the obtained powders were immersed in a H$_2$PtCl$_6$·6H$_2$O aqueous solution with 0.1 wt% of Pt to BaTaO$_2$N, followed by heating at 200 °C for 1 h under a mixed H$_2$ (20 ml·min^{-1}) and N$_2$ (200 ml·min^{-1}) atmosphere. Subsequently, the Pt-modified BaTaO$_2$N (0.1 g)

was dispersed in a 150 ml aqueous solution with 10 vol% methanol as the hole scavenger. After completely removing the dissolved air, the mixed solution was irradiated using a 300-W Xe lamp with a 420-nm cutoff filter, and the evolved gas was detected by an online thermal conductivity detector gas chromatography system.

Characterization. The crystallization phases of the samples were determined using X-ray diffraction (XRD; MiniFlexII, Rigaku) with Cu Kα irradiation. The optical properties of the samples were measured using UV-vis diffused reflectance spectroscopy (UV-vis DRS) with a JASCO V-670 spectrophotometer. The morphologies of the samples were detected by field-emission scanning electron microscopy (FESEM; JSM-7600F, JEOL). The exposed facet of the optimized sample was determined using transmission electron microscopy (TEM; EM-002B, TOPCON) and selected area electron diffraction (SAED) patterns. The surface areas of the samples were obtained by nitrogen adsorption-desorption isotherms (BELSORP-mini). X-ray photoelectron spectroscopy (XPS) was used to determine the defect density (JPS-9010MX, JEOL) and the valence band position (PHI Quantera II) of the samples.

3. Results and discussion

The molar ratio of K_2CO_3/KCl greatly influences the crystallinity and morphology of $BaTaO_2N$. Figure 1a shows the XRD patterns of the $BaTaO_2N$ crystals grown from K_2CO_3–KCl binary flux with various molar ratios and a solute concentration of 10 mol% at 950 °C for 8 h. All the diffraction peaks in the XRD patterns of the crystals grown with a K_2CO_3/KCl molar ratio of ≤20/80 were attributed to the single-phase $BaTaO_2N$ by referring to the International Center for Diffraction Data Powder Diffraction File (ICDD PDF 01-084-1748). Upon increasing the K_2CO_3 content (molar ratio >20/80), a hexagonal $Ba_5Ta_4O_{15}$ (ICDD PDF 01-072-0631) impure phase was produced along with the main crystalline phase of $BaTaO_2N$ and the diffraction peak intensities of $Ba_5Ta_4O_{15}$ increased as the K_2CO_3 content increased. When only K_2CO_3 was employed as flux, some stronger diffraction peaks of impurities that were assigned to $Ba_5Ta_4O_{15}$ and Ta_3N_5 (ICDD PDF 01-079-1533) were observed, and the obtained sample exhibited

a highly aggregated irregular shape (Figure 2 and Figure 3a). In contrast, similar cubic-like BaTaO$_2$N crystals with a small amount of rod-like Ta$_3$N$_5$ impure phases were obtained when only KCl flux was used (Figure 4 and Figure 3b), in which the formation of Ta$_3$N$_5$ was attributed to the loss of barium with the KCl volatilization during the high-temperature nitridation process.[20,25] These results implied that the use of K$_2$CO$_3$ alone as flux is not suitable for growing single-phase BaTaO$_2$N crystals, while a suitable K$_2$CO$_3$ content could help avoid the loss of barium volatilization and obtain single phase of BaTaO$_2$N from the KCl flux. In addition, the UV-vis DRS spectra (Figure 1b) shows that the sample with a K$_2$CO$_3$/KCl molar ratio of ≤20/80 has a visible absorption edge at ~660 nm, corresponding to a band gap of ~1.89 eV. However, for the sample with a K$_2$CO$_3$/KCl molar ratio of >20/80, the absorption edge shifted towards shorter wavelengths due to the existence of the Ba$_5$Ta$_4$O$_{15}$ impure phase.
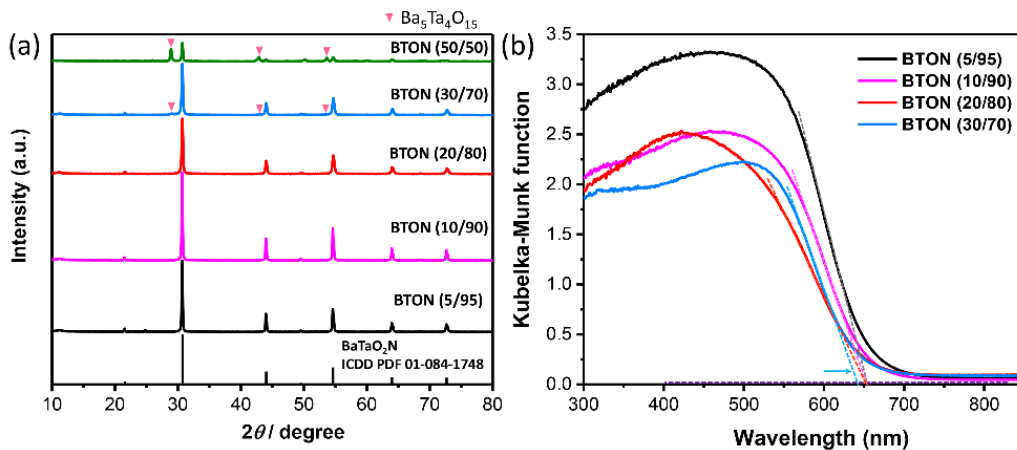
Figure 1. (a) XRD patterns and (b) UV-vis DRS spectra of BaTaO$_2$N grown from K$_2$CO$_3$–KCl binary flux with various molar ratios at 950 °C for 8 h.
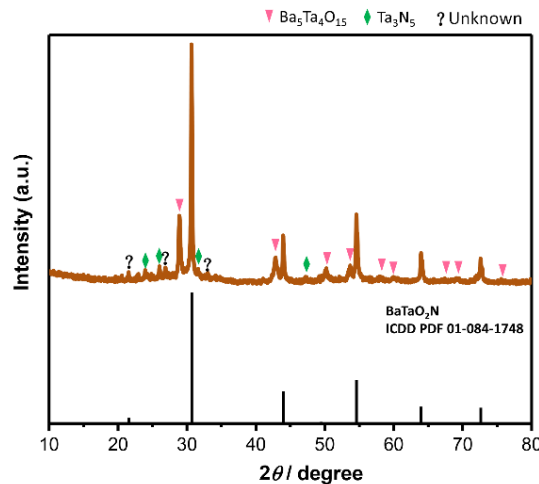
**Figure 2.** XRD pattern of BaTaO$_2$N grown from K$_2$CO$_3$ flux at 950 ℃ for 8 h.
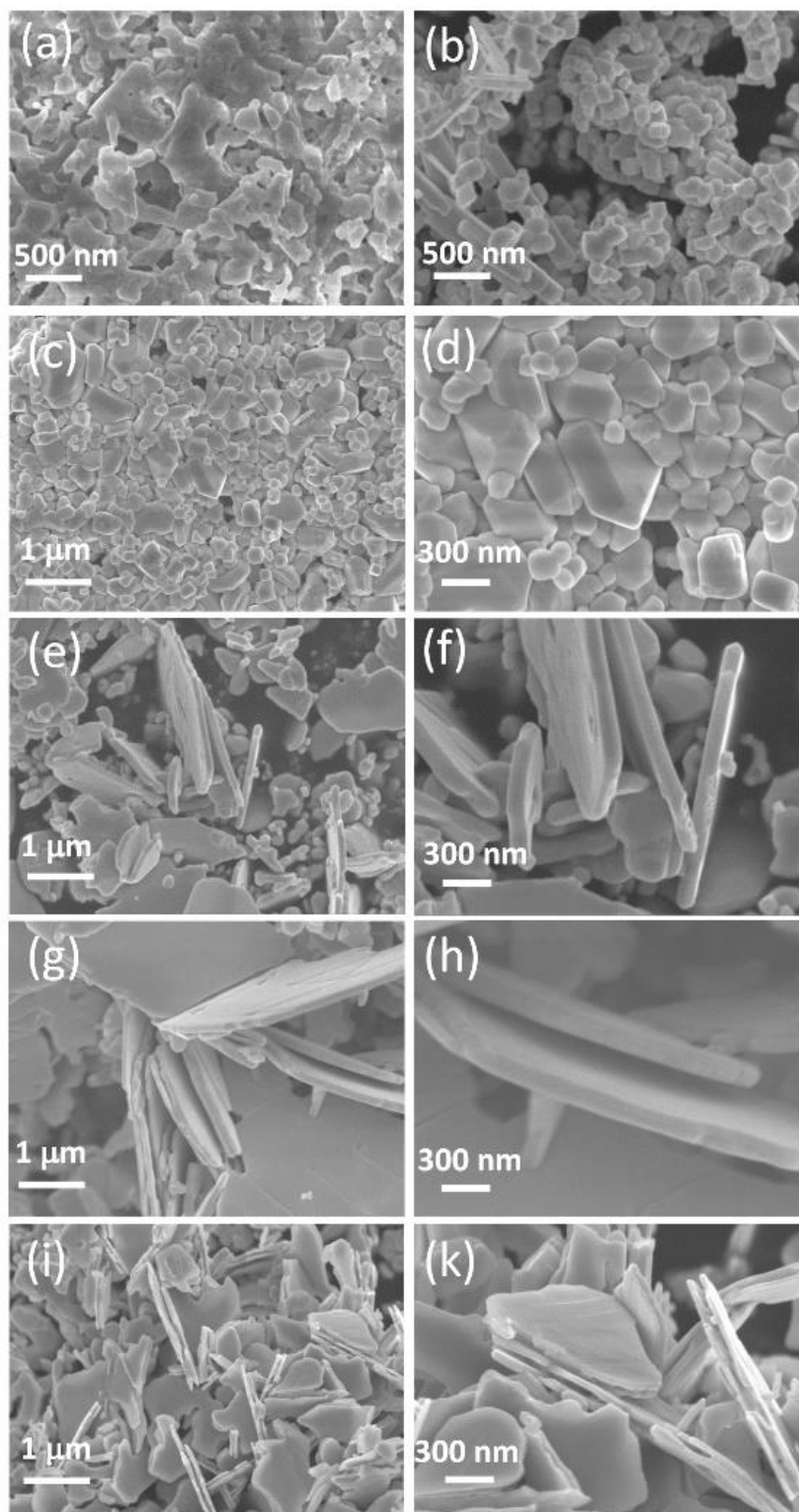
Figure 3. SEM images of BaTaO$_2$N grown from (a) single K$_2$CO$_3$ flux, (b) single KCl flux, and K$_2$CO$_3$–KCl binary flux with molar ratios of (c, d) 5/95, (e, f) 10/90, (g, h) 20/80, and (i, k) 30/70 at 950 °C for 8 h.
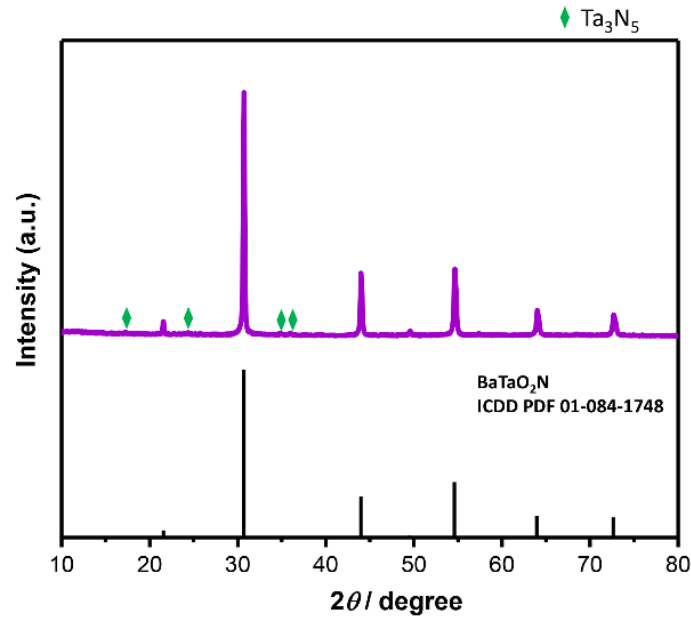
Figure 4. XRD pattern of BaTaO$_2$N grown from KCl flux at 950 ℃ for 8 h.

Generally, it is suggested that the BaTaO$_2$N crystal grows into a cubic shape because the crystal structure of BaTaO$_2$N belongs to the cubic system. As shown in Figure 3b, similar cubic-like BaTaO$_2$N crystals were obtained when only KCl was employed as flux. Conversely, a significant change in morphology was observed for the BaTaO$_2$N grown from the K$_2$CO$_3$–KCl binary flux, as shown in Figure 3c–k. When a small amount of K$_2$CO$_3$ was added, the BTON (5/95) sample exhibited a polyhedral crystal shape with a particle size from 150 nm to 700 nm. This large difference in particle size was most likely due to the uneven diffusion of small amounts of K$_2$CO$_3$ (Figure 3c, d). Upon increasing the K$_2$CO$_3$/KCl molar ratio, platy crystals were formed (Figure 3e–h). However, when the molar ratio of K$_2$CO$_3$/KCl increased to 30/70, the edges of the platy crystals became rough (Figure 3i, k).
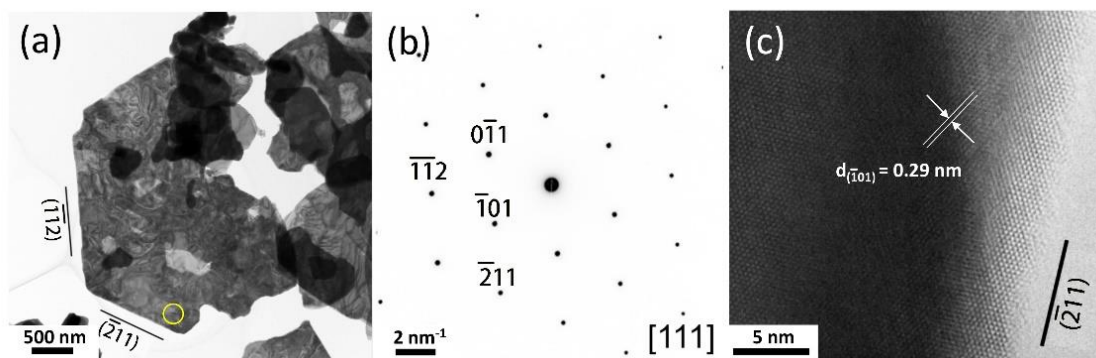
Figure 5. (a) Bright-field TEM image, (b) SAED pattern, and (c) HRTEM image of BaTaO$_2$N grown from K$_2$CO$_3$–KCl binary flux with molar ratio of 20/80 at 950 °C for 8 h.
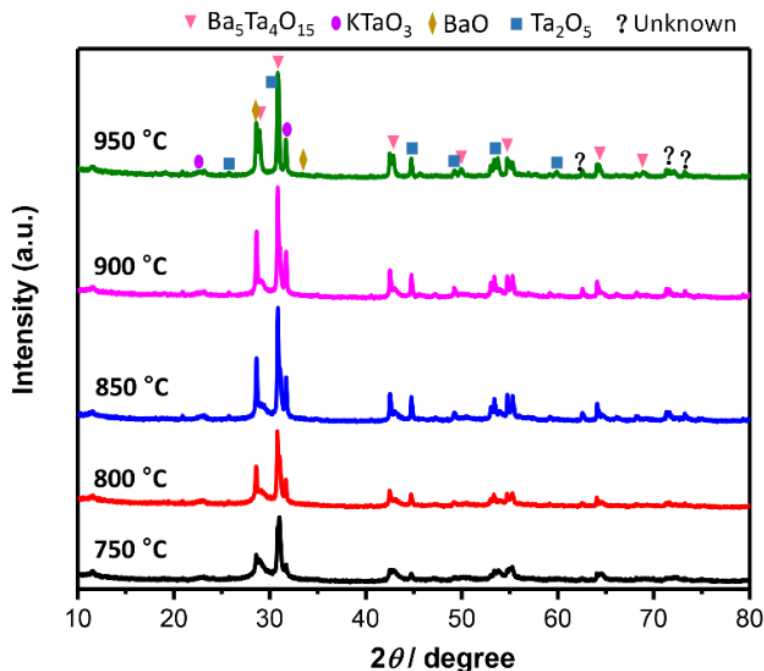

Figure 6. XRD patterns of BaTaO$_2$N grown from K$_2$CO$_3$–KCl binary flux with molar ratio of 20/80 at different temperatures for 0 h. Herein, 0 h indicates that the raw materials were heated to different temperatures (750 °C, 800 °C, 850 °C, etc.), without going through the holding stage, and then cooled to room temperature.

To further investigate the exposed facets of the platy crystals, the typical BTON (20/80) sample was characterized using bright-field TEM and SAED. Figure 5 shows the bright-field TEM image, SAED pattern, and high-resolution TEM (HRTEM) image of the platy crystals. The highly and clearly ordered diffraction spots, viewed from the [111] direction of BTON (20/80), indicate that the platy BaTaO$_2$N was a single crystal with high crystallinity. The HRTEM image, taken near the edge of the platy crystal in the circled area indicated in Figure 5a, shows that the spacing between the adjacent lattice fringes is 0.29 nm which corresponds to the (-101) lattice spacing of BaTaO$_2$N. Moreover, these diffraction spots on the left side of Figure 5b can be indexed as 0-11, -1-12, and -101; thus, we can conclude that the platy BaTaO$_2$N crystal dominantly exposed {111} facets and was enclosed by {-211} as shown in Figure 5a. The SEM and

TEM results implied that the platy $BaTaO_2N$ crystals with exposed {111} facets could be fabricated by simply varying the molar ratio of K_2CO_3/KCl during the nitridation process, indicating that the K_2CO_3 critically affected the crystallization behavior, and this led to a significant change in morphology of $BaTaO_2N$.

Next, the $BaTaO_2N$ crystals from the K_2CO_3–KCl binary flux with a molar ratio of 20/80 was grown at different temperatures and holding times to gain insight into the formation mechanism of the platy $BaTaO_2N$ crystals. Figure 6 shows the XRD patterns of the samples prepared at different temperatures for 0 h. Herein, 0 h indicates that the raw materials were heated to different temperatures (750 °C, 800 °C, 850 °C, etc.), without going through the holding stage, and then cooled to room temperature. In these samples, the $BaCO_3$ gradually decomposed to BaO, $Ba_5Ta_4O_{15}$ and $KTaO_3$ phases were observed. As the temperature increased to 850 °C, the intensity of the diffraction peaks increased as the liquid-phase line of the K_2CO_3–KCl binary flux with a molar ratio of 20/80 is close to 700 °C,[26] this allowed the reactants to decompose, diffuse and react with each other sufficiently. However, according to a previous study by Hojamberdiev *et al.*,[27] when only KCl was selected as the flux for the growth of $BaTaO_2N$, $BaTa_2O_6$ with lattice parameters of $a = b = 21.12$ Å and $c = 3.92$ Å in the hexagonal *P6/mmm* space group[28] was initially formed and no $KTaO_3$ was detected during the heating process, indicating that the intermediate phase can be controlled *via* the appropriate addition of CO_3^{2-} in the flux. Moreover, as reported,[29,30] oxo-anions such as SO_4^{2-}, NO_3^- and CO_3^{2-} tend to generate O^{2-} ions which can promote the dissolution of metal oxides and then form the corresponding oxo-complexes during the high temperature melting reaction. In our case, besides KCl, K_2CO_3 with a melting point of 891 °C was also added in the reaction system. Therefore, the decomposition and diffusion of the precursors occurred in the binary flux, and the oxo-complex $[TaO_3]^-$ was subsequently formed through the reaction between dissolved Ta_2O_5 and the O^{2-} produced by K_2CO_3. These oxo-complexes were combined by corner-sharing to form the basic framework of $KTaO_3$, or to form 2-dimensional arrays of $Ba_5Ta_4O_{15}$. This explains why $KTaO_3$ was not observed when only KCl was used as flux, while it was observed when K_2CO_3/KCl

was used as flux. $Ba_5Ta_4O_{15}$ was formed instead of $BaTa_2O_6$ during the heating stage, this is because of the generation of oxo-complex $[TaO_3]^-$ assisted by CO_3^{2-} and part of the tantalum source was consumed by the formation of $KTaO_3$.
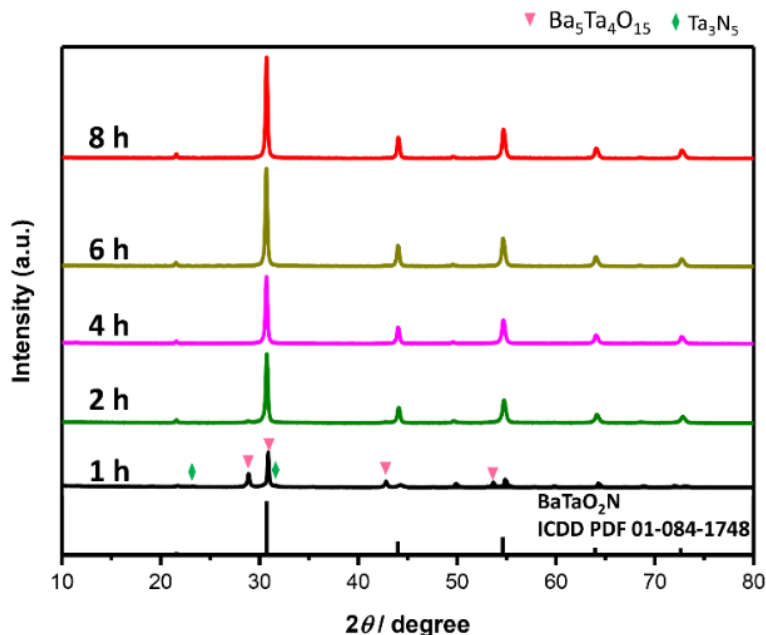

Figure 7. XRD patterns of BaTaO₂N grown from K_2CO_3–KCl binary flux with molar ratio of 20/80 at 950 °C for different holding time.

However, $Ba_5Ta_4O_{15}$ and $KTaO_3$ only existed as intermediate phases during the nitridation process, in which O^{2-} was replaced by N^{3-} produced by the dissociation of NH_3. As shown in Figure 7, $KTaO_3$ was transformed into Ta_3N_5 in a relatively short nitridation time ($\leq$1 h), with the volatilization of potassium ions and the formation of $BaTaO_2N$ accompanied by the transformation of $Ba_5Ta_4O_{15}$ and Ta_3N_5. Moreover, the diffraction peak intensity of Ta_3N_5 decreased faster than that of $Ba_5Ta_4O_{15}$ due to the reaction of Ta_3N_5 with completely dissolved BaO. As a result, $Ba_5Ta_4O_{15}$ was the main intermediate phase for the formation of $BaTaO_2N$ in the subsequent reaction. With the further dissociation of NH_3 resulting in a considerable amount of nitriding species in the reaction system, the pure $BaTaO_2N$ phase was observed after 2 h at 950 °C and the relevant diffraction peaks became stronger as the holding time increased. Figure 8 shows the SEM images of the samples prepared at 950 °C for different holding times. The crystals prepared for 1 h exhibited small and irregular platy morphologies, which

mainly reflected the morphology of $Ba_5Ta_4O_{15}$ intermediate phases according to the XRD results. $Ba_5Ta_4O_{15}$ consists of five close-packed asymmetric layers and it belongs to the hexagonal crystal system, so it can show a hexagonal platy shape.[31] Upon prolonging the holding time at 950 °C, these crystals grew larger and the edges became clearer. We observed that these plates did not transform into the cubes which are part of the thermodynamically stable shape of $BaTaO_2N$, but it still maintained the shape of $Ba_5Ta_4O_{15}$, indicating that there is some correlation between the structures of $Ba_5Ta_4O_{15}$ and $BaTaO_2N$.
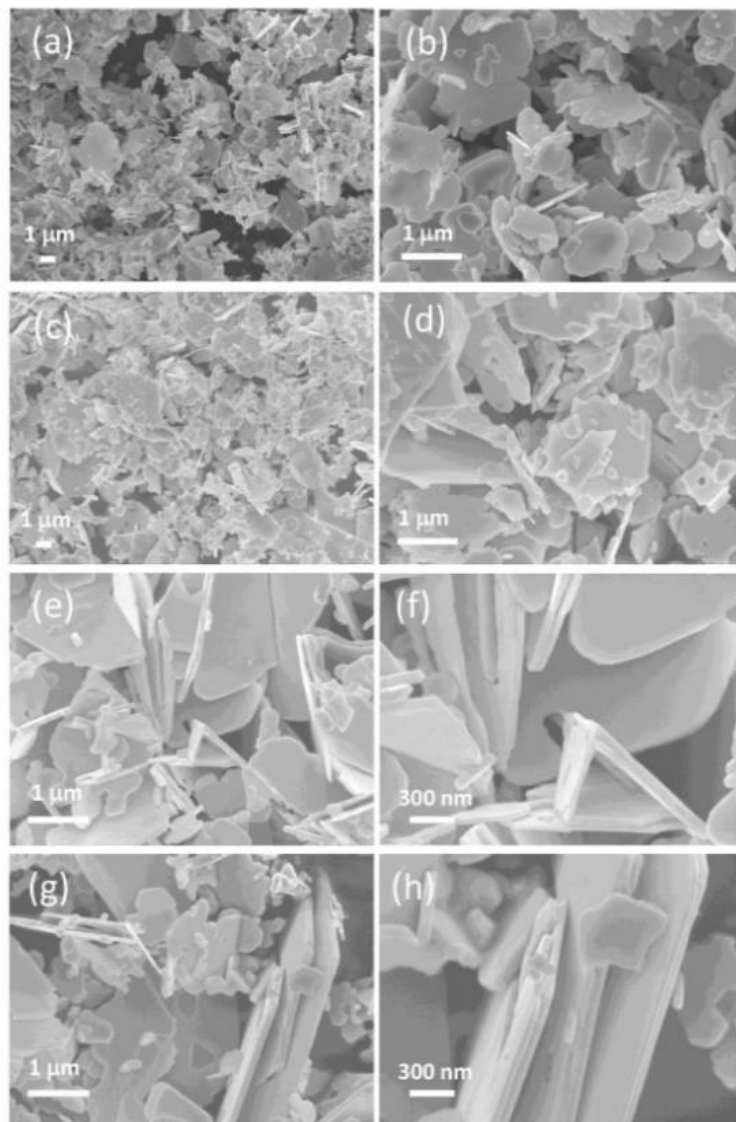
Figure 8. SEM images of $BaTaO_2N$ grown from K_2CO_3–KCl binary flux with molar ratio of 20/80 at 950 °C for (a, b) 1 h, (c, d) 2 h, (e, f) 4 h, and (g, h) 6 h. The SEM

images of the crystals grown from K_2CO_3–KCl binary flux with molar ratio of 20/80 at 950 °C for 8 h are shown in Figure 3e, f.
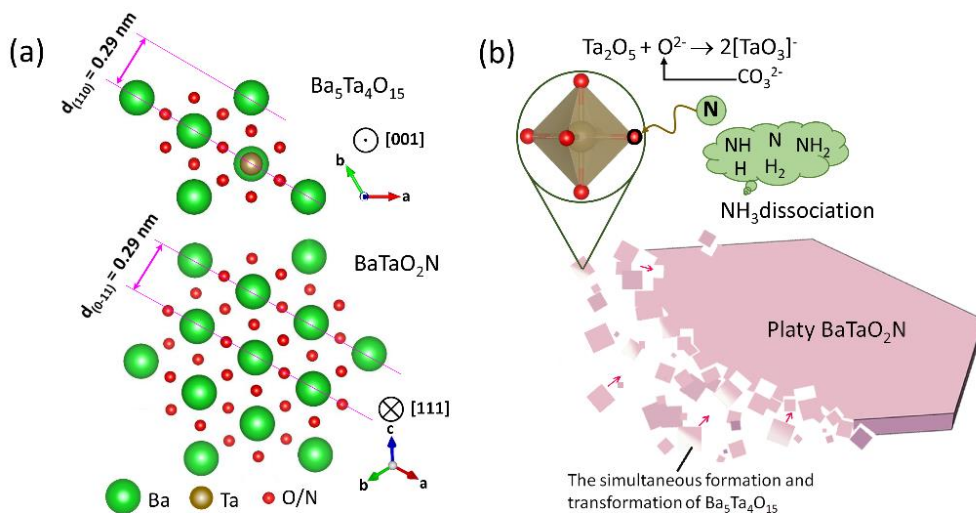

Figure 9. (a) Crystal structures of $Ba_5Ta_4O_{15}$ viewed from the [00-1] direction (top) and $BaTaO_2N$ viewed from the [111] direction (bottom), produced using the VESTA program.[32] (b) Schematic illustration of the formation mechanism of the platy $BaTaO_2N$ crystal.
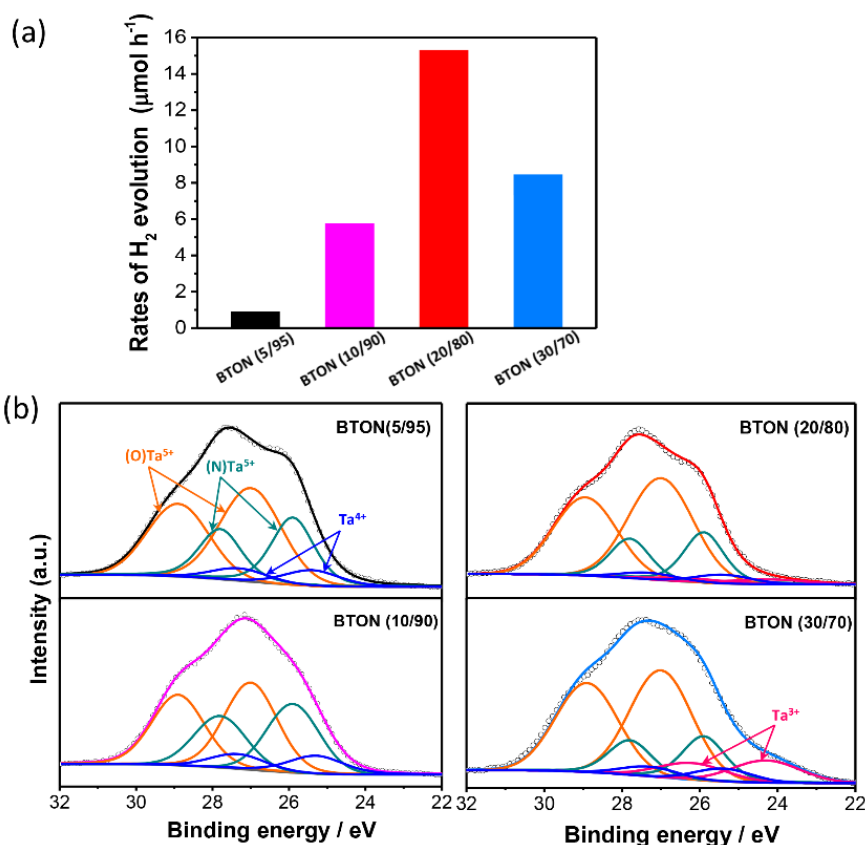
Figure 10. (a) H_2 evolution rates of $BaTaO_2N$ grown from K_2CO_3–KCl binary flux with various molar ratios at 950 °C for 8 h. Reaction conditions: 0.1 wt% Pt-modified $BaTaO_2N$, 0.1g; ultrapure water, 150 ml; 10 vol.% CH_3OH; 300-W Xe lamp ($\lambda > 420$ nm). (b) Ta 4f XPS spectra of $BaTaO_2N$ grown from K_2CO_3–KCl binary flux with various molar ratios at 950 °C for 8 h.

As shown in Figure 9a, the atomic arrangement of the $Ba_5Ta_4O_{15}$ (001) plane matches well with that of $BaTaO_2N$ (111) plane with a lattice mismatch of 0.7%, implying that the $BaTaO_2N$ crystal with exposed {111} facets can be obtained from the transformation of $Ba_5Ta_4O_{15}$ {001} facets. However, it has been proven that the $BaTaO_2N$ grown by directly nitriding the $Ba_5Ta_4O_{15}$ precursor had a porous morphology owing to the replacement of three O^{2-} by two N^{3-}. Therefore, we can conclude that $BaTaO_2N$ with a smooth surface can be obtained when the formation and transformation of $Ba_5Ta_4O_{15}$ simultaneously occurs during the growth stage of $BaTaO_2N$. Based on these analyses, we proposed a possible growth mechanism of the platy $BaTaO_2N$ with a smooth surface. During the heating stage, $KTaO_3$ and $Ba_5Ta_4O_{15}$ were produced with the assistance of CO_3^{2-}. After that, the $KTaO_3$ transformed quickly
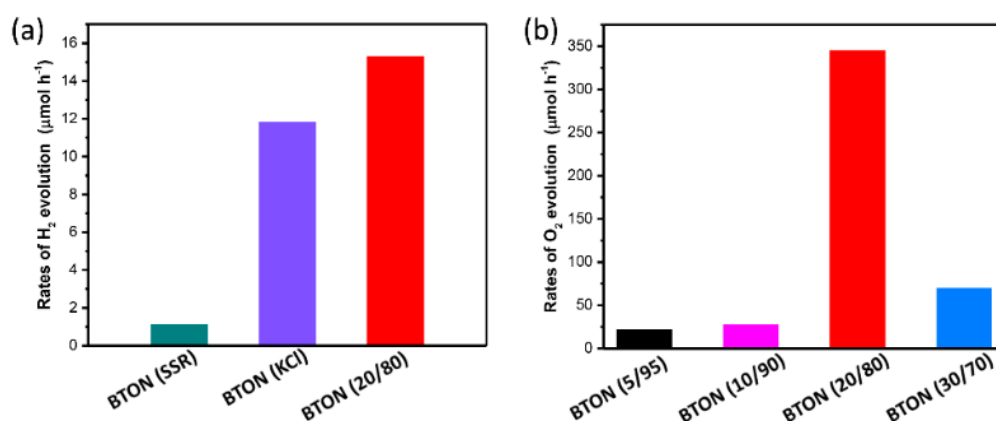

Figure 11. (a) H_2 evolution rates of BTON (SSR), BTON (KCl) and BTON (20/80) samples. (b) O_2 evolution rates of $BaTaO_2N$ grown from K_2CO_3–KCl binary flux with various molar ratios at 950 °C for 8 h. Conditions: (a), 0.1 wt% Pt-modified $BaTaO_2N$, 0.1g; ultrapure water, 150 ml; 10 vol.% CH_3OH; 300-W Xe lamp ($\lambda > 420$ nm). (b), 0.5 wt% Co-modified $BaTaO_2N$, 0.1g; ultrapure water, 150 ml; La_2O_3, 0.05 g; 0.2 mol·L^{-1} $AgNO_3$, 300-W Xe lamp ($\lambda > 420$ nm).

to Ta_3N_5 with the volatilization of potassium ions in NH_3 atmosphere. Upon prolonging the holding time at 950 °C, Ta_3N_5 completely reacted with BaO, and thus $Ba_5Ta_4O_{15}$ was the main intermediate phase for the formation of $BaTaO_2N$ in the subsequent reaction. Since the flux is as excessive as the solvent, the CO_3^{2-} in the flux continued to produce the oxo-complexes $[TaO_3]^-$ and promote the formation of $Ba_5Ta_4O_{15}$. Meanwhile, a considerable amount of nitriding species produced by the dissociation of NH_3 replaced the O^{2-} in the oxo-complexes, thereby leading to the simultaneous formation and transformation of $Ba_5Ta_4O_{15}$, as shown in Figure 9b. Consequently, the platy $BaTaO_2N$ crystals with smooth surface were obtained.

Table 1. Brunauer–Emmett–Teller (BET) surface area of $BaTaO_2N$ grown from K_2CO_3–KCl binary flux with various molar ratios at 950 °C for 8 h.

Photocatalysts	BET surface area / m^2g^{-1}
BTON (5/95)	2.51
BTON (10/90)	4.28
BTON (20/80)	3.45
BTON (30/70)	4.38

We then investigated the photocatalytic performance of H_2 evolution on $BaTaO_2N$ grown from K_2CO_3–KCl binary flux under visible irradiation. Each sample was modified with 0.1 wt% Pt cocatalysts *via* an impregnation process before the reaction. As shown in Figure 10a, the photocatalytic H_2 evolution activity strongly depended on the K_2CO_3/KCl molar ratios. As the molar ratio of K_2CO_3/KCl increased, the photocatalytic H_2 evolution rate was enhanced significantly, reaching an optimal activity at a K_2CO_3/KCl molar ratio of 20/80. Moreover, the H_2 evolution rate on BTON (20/80) was also higher than that on $BaTaO_2N$ prepared by a solid-state reaction and single KCl flux (Figure 11a). As mentioned, K_2CO_3 as flux is not suitable for growing single-phase $BaTaO_2N$ crystals but is suitable for controlling the morphology of $BaTaO_2N$, thereby BTON (KCl) showed a good activity but was still lower than BTON (20/80). In addition, we explored the evolution of O_2 on $BaTaO_2N$ grown from K_2CO_3–KCl binary flux (Figure 11b). This was similar to the H_2 evolution reaction, in

which the O_2 evolution rate on BTON (20/80) was clearly higher than those on other samples. Although the specific surface areas of BTON (20/80) were slightly smaller than BTON (10/90) and BTON (30/70) (Table 1), BTON (20/80) still exhibited the best photocatalytic performance. This indicated that the activity of these samples did not strongly depend on the surface areas. According to the band positions of $BaTaO_2N$ (Figure 12), the conduction band of BTON (20/80) is lower than that of BTON (30/70) and the valence band is higher than that of BTON (5/95), suggesting that BTON (20/80) does not have the strongest reduction or oxidation driving forces among these samples. Therefore, the outstanding activity of BTON (20/80) was not caused by the driving forces. In contrast, the reduced tantalum species produced by the reducing ammonolysis atmosphere and the replacement of three O^{2-} with two N^{3-} ions could act as the recombination centers of photo-generated electron-hole pairs and affect the photocatalytic performance.[33] The XPS analysis of the as-prepared samples are shown in Figure 13 and Figure 10b. There is no signal in the region of K 2p and Cl 2p, reflecting that K and Cl elements did not remain in the samples. Owing to the difference in the electronegativity of O and N atoms, the binding energy of Ta^{5+} with N^{3-} was lower than that of Ta^{5+} with O^{2-}.[34] Apart from the main peaks of Ta^{5+}, some reduced Ta species (Ta^{4+}, Ta^{3+}) were also detected at lower binding energies, which were greatly affected by the addition of K_2CO_3. The density of Ta^{4+} decreased as the K_2CO_3/KCl molar ratio increased and reached a minimum at a ratio of 20/80 while reduced Ta^{3+} species were simultaneously observed. However, the density of Ta^{3+} increased when the molar ratio was greater than 20/80 indicating that BTON (20/80) had fewer defects. Moreover, as described above, BTON (20/80) showed a well-crystallized plate-like structure, which would shorten the diffusion distance of photo-excited charges and facilitate the charge carriers transfer from the interior to the surface of the $BaTaO_2N$ plate.[21,35] As such, the performance of the BTON (20/80) photocatalyst for photocatalytic H_2 evolution was good. For the first time, we obtained a well-grown and highly-crystalline $BaTaO_2N$ plate photocatalyst with comparable or higher H_2-evolution activities than previous $BaTaO_2N$ with different morphologies.[27,36,37]

Although highly crystalline platy crystals were obtained, they still contained a few defects on the surface and in the bulk of BaTaO$_2$N generated during the crystallization process, as discussed in the XPS section. Therefore, there is enough room to further improve the photocatalytic efficiency of H$_2$ evolution on platy BaTaO$_2$N by decreasing the thickness of the plate structure and defect density in the crystal structure *via* refinement of the fabrication procedure and the use of various carbonate-chloride binary flux species. In addition, it is desirable to extend the application of multiple fluxes in the fabrication of shape-controlled and well-crystallized oxynitrides with high photocatalytic performance.
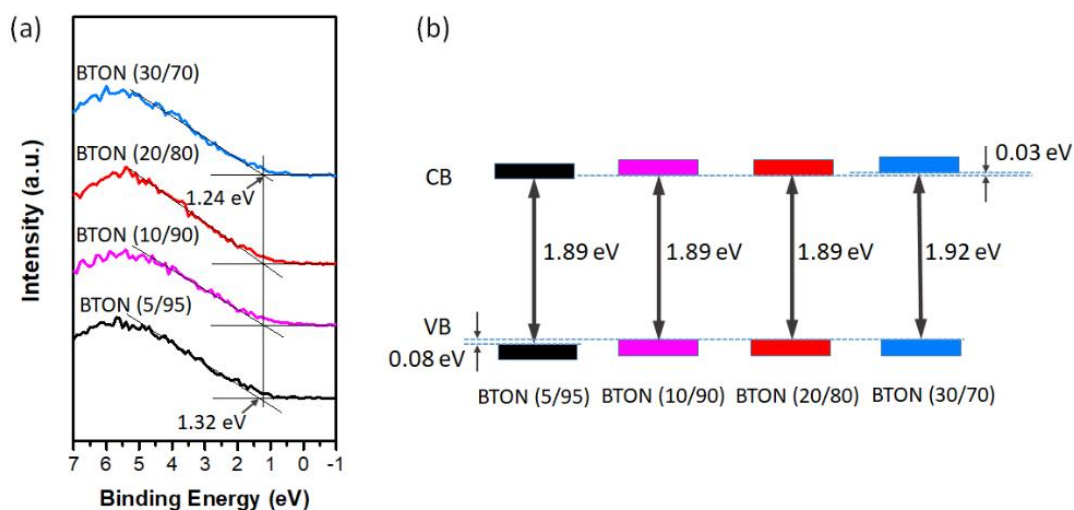
Figure 12. (a) Valence band XPS spectra, and (b) schematic illustration of the band positions of BaTaO$_2$N grown from K$_2$CO$_3$–KCl binary flux with various molar ratios at 950 °C for 8 h. The band gaps of (b) were calculated according to the results of UV-vis DRS in Figure 1b.
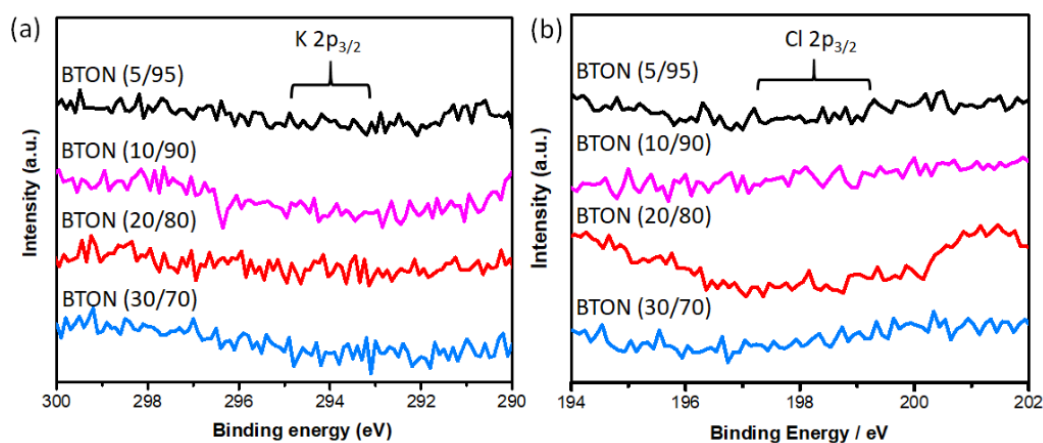
Figure 13. (a) K 2p and (b) Cl 2p XPS spectra of $BaTaO_2N$ grown from K_2CO_3–KCl binary flux with various molar ratios at 950 °C for 8 h.

4. Conclusion

Platy $BaTaO_2N$ crystals with dominantly exposing {111} facets were synthesized by simply varying the molar ratio of K_2CO_3/KCl binary flux during a nitridation process. The formation mechanisms of the platy $BaTaO_2N$ were investigated by controlling the growth conditions. By the assistance of CO_3^{2-} and the dissociation of NH_3, the formation and transformation of $Ba_5Ta_4O_{15}$ occurred simultaneously during the growth stage of $BaTaO_2N$. In addition, the atomic arrangement of the $BaTaO_2N$ (111) plane matches well with that of $Ba_5Ta_4O_{15}$ (001) plane. These resulted in a platy $BaTaO_2N$ crystal with dominantly exposing {111} facets. Moreover, we observed that the K_2CO_3/KCl molar ratio of 20/80 was the most suitable for obtaining well-grown and high-quality $BaTaO_2N$ platy crystals. Because of the plate-like structure and high crystallinity that shortened the travel distance and facilitated the transfer of photo-excited carriers, BTON (20/80) showed excellent photocatalytic performance in this study.

5. References

(1) Xia, Y.; Xiong, Y.; Lim, B.; Skrabalak, S. E. Shape-Controlled Synthesis of Metal Nanocrystals: Simple Chemistry Meets Complex Physics? *Angew. Chem. Int. Ed.* **2009**, *48*, 60–103.

(2) Jun, Y.; Choi, J.; Cheon, J.; Shape Control of Semiconductor and Metal Oxide Nanocrystals through Nonhydrolytic Colloidal Routes. *Angew. Chem. Int. Ed*. **2006**, *45*, 3414–3439.

(3) Chen, D. P.; Fu, J.; Skrabalak, S. E. Towards Shape Control of Metal Oxide Nanocrystals in Confined Molten Media. *ChemNanoMat*. **2015**, *1*, 18–26.

(4) Osterloh, F. E. Inorganic Nanostructures for Photoelectrochemical and Photocatalytic Water Splitting. *Chem. Soc. Rev*. **2013**, *42*, 2294–2320.

(5) Zhang, L.; Wang, W.; Zhou, L.; Xu, H. Bi_2WO_6 Nano- and Micro-structures: Shape Control and Associated Visible-Light-Driven Photocatalytic Activities. *Small*, **2007**, *9*, 1618–1625.

(6) Wang, Z.; Lv, K.; Wang, G.; Deng, K.; Tang, D. Study on the Shape Control and Photocatalytic Activity of High-Energy Anatase Titania. *Appl. Catal. B: Environ.* **2010**, *100*, 378–385.

(7) Li, R.; Zhang, F.; Wang, D.; Yang, J.; Li, M.; Zhu, J.; Zhou, X.; Han, H.; Li, C. Spatial Separation of Photogenerated Electrons and Holes Among {010} and {110} Crystal Facets of $BiVO_4$. *Nat. Commun.* **2013**, *4*, 1432.

(8) Huang, K.; Yuan, L.; Feng, S. Crystal Facet Tailoring Arts in Perovskite Oxides. *Inorg. Chem. Front.* **2015**, *2*, 965–981.

(9) Bugaris, D. E.; Zur Loye, H. C. Materials Discovery by Flux Crystal Growth: Quaternary and Higher Order Oxides. *Angew. Chem. Int. Ed.* **2012**, *51*, 3780–3811.

(10) Yang, S.; Yang, B.; Wu, L.; Li, Y.; Liu, P.; Zhao, H.; Yu, Y.; Gong, X.; Yang, H. Titania Single Crystals with a Curved Surface. *Nat. Commun*. **2014**, *5*, 5355.

(11) Zhang, L.; Fu, X.; Meng, S.; Jiang, X.; Wang, J.; Chen, S. Ultra-low Content of Pt Modified CdS Nanorods: One-Pot Synthesis and High Photocatalytic Activity for H_2 Production under Visible Light. *J. Mater. Chem. A* **2015**, *3*, 23732–23742.

(12) Ou, H.; Lin, L.; Zheng, Y.; Yang, P.; Fang, Y.; Wang, X. Tri-s-triazine-Based Crystalline Carbon Nitride Nanosheets for an Improved Hydrogen Evolution. *Adv. Mater.* **2017**, *29*, 1700008.

(13) Fuertes, A. Metal Oxynitrides as Emerging Materials with Photocatalytic and Electronic Properties, *Mater. Horiz.* **2015**, *2*, 453–461.

(14) Wang, Z.; Li, C.; Domen, K. Recent Developments in Heterogeneous Photocatalysts for Solar-Driven Overall Water Splitting. *Chem. Soc. Rev.* **2019**, *48*, 2109–2125.

(15) Fang, M.; De Wijs, G. A.; Orhan, E.; De With, G.; De Groot, R. A. Hintzen, H. T. Marchand, R. Local Structure and Electronic Properties of BaTaO$_2$N with Perovskite-Type Structure. *J. Phys. Chem. Solids.* **2003**, *64*, 281–286.

(16) Luo, Y.; Suzuki, S.; Wang, Z.; Yubuta, K.; Vequizo, J. J. M.; Yamakata, A.; Shiiba, H.; Hisatomi, T.; Domen, K.; Teshima, K. Construction of Spatial Charge Separation Facets on BaTaO$_2$N Crystals by Flux Growth Approach for Visible-Light-Driven H$_2$ Production. *ACS Appl. Mater. Interfaces* **2019**, *11*, 22264–22271.

(17) Ueda, K.; Minegishi, T.; Clune, J.; Nakabayashi, M.; Hisatomi, T.; Nishiyama, H.; Katayama, M.; Shibata, N.; Kubota, J.; Yamada, T.; Domen, K. Photoelectrochemical Oxidation of Water Using BaTaO$_2$N Photoanodes Prepared by Particle Transfer Method. *J. Am. Chem. Soc.* **2015**, *137*, 2227–2230.

(18) Wang, C.; Hisatomi, T.; Minegishi, T.; Wang, Q.; Zhong, M.; Katayama, M.; Kubota, J.; Domen, K. Synthesis of Nanostructured BaTaO$_2$N Thin Films as Photoanodes for Solar Water Splitting. *J. Phys. Chem. C* **2016**, *120*, 15758–15764.

(19) Maeda, K.; Domen, K. Preparation of BaZrO$_3$−BaTaO$_2$N Solid Solutions and the Photocatalytic Activities for Water Reduction and Oxidation under Visible Light. *J. Catal.* **2014**, *310*, 67–74.

(20) Luo, Y.; Wang, Z.; Suzuki, S.; Yubuta, K.; Kariya, N.; Hisatomi, T.; Domen, K.; Teshima, K. Fabrication of Single-Crystalline BaTaO$_2$N from Chloride Fluxes for Photocatalytic H$_2$ Evolution under Visible Light. *Cryst. Growth Des*. **2020**, *20*, 255–261.

(21) Ida, S.; Ishihara, T. Recent Progress in Two-Dimensional Oxide Photocatalysts for Water Splitting. *J. Phys. Chem. Lett.* **2014**, *5*, 2533–2542.

(22) Suzuki, S.; Yanai, M.; Yamada, T.; Wagata, H.; Sasaki, Y.; Oishi, S.; Domen, K.; Teshima, K. Ta$_3$N$_5$ Photoanodes Fabricated by Providing NaCl−Na$_2$CO$_3$ Evaporants to Tantalum Substrate Surface under NH$_3$ Atmosphere. *ACS Appl. Energy Mater*. **2018**, *1*, 6129–6135.

(23) Yamada, T.; Zettsu, N.; Kim, H.; Hagano, Y.; Handa, N.; Yubuta, K.; Teshima, K. One-Dimensional Growth of Li_2NiPO_4F Single Crystals from Intermediate $LiNiPO_4$ Crystal Surface Using KCl−KI Molten Fluxes. *Cryst. Growth Des*. **2018**, *18*, 6777–6785.

(24) Yamada, T.; Zettsu, N.; Nozaki, S.; Teshima, K. Growth of Idiomorphic $LiMnPO_4$ Crystals in Molten NaCl−KCl and LiF−NaCl−KCl Fluxes. *CrystEngComm* **2017**, *19*, 93–98.

(25) Hisatomi, T.; Katayama, C.; Teramura, K.; Takata, T.; Moriya, Y.; Minegishi, T.; Katayama, M.; Nishiyama, H.; Yamada, T.; Domen, K. The Effects of Preparation Conditions for a $BaNbO_2N$ Photocatalyst on Its Physical Properties. *ChemSusChem* **2014**, *7*, 2016–2021.

(26) Yaokawa, J.; Oikawa, K.; Anzai, K. Thermodynamic Assessment of the KCl-K_2CO_3-$NaCl$-Na_2CO_3 System. *Calphad* **2007**, *31*, 155–163.

(27) Hojamberdiev, M.; Yubuta, K.; Vequizo, J. J. M.; Yamakata, A.; Oishi, S.; Domen, K.; Teshima, K. NH_3-Assisted Flux Growth of Cube-like $BaTaO_2N$ Submicron Crystals in a Completely Ionized Nonaqueous High-Temperature Solution and Their Water Splitting Activity. *Cryst. Growth Des.* **2015**, *15*, 4663–4671.

(28) Xu, T.; Zhao, X.; Zhu, Y. Synthesis of Hexagonal $BaTa_2O_6$ Nanorods and Influence of Defects on the Photocatalytic Activity. *J. Phys. Chem. B* **2006**, *110*, 25825–25832

(29) Sudare, T.; Kawaura, D.; Yubuta, K.; Hayashi, F.; Teshima, K. Growth of {100}-Faceted $NaFeTiO_4$ Crystals with Tunable Aspect Ratio from a $NaCl$–Na_2SO_4 Binary Flux. *CrystEngComm* **2018**, *20*, 873–878.

(30) Xiao, X.; Hayashi, F.; Yubuta, K.; Selloni, A.; Teshima, K. Effects of Alkali Cations and Sulfate/Chloride Anions on the Flux Growth of {001}-Faceted β-Li_2TiO_3 Crystals. *Cryst. Growth Des.* **2017**, *17*, 1118–1124.

(31) Xu, T. G.; Zhang, C.; Shao, X.; Wu, K.; Zhu, Y. F. Monomolecular-Layer $Ba_5Ta_4O_{15}$ Nanosheets: Synthesis and Investigation of Photocatalytic Properties.

Adv. Funct. Mater. **2006**, *16*, 1599–1607.

(32) Momma, K.; Izumi, F. VESTA 3 for Three-Dimensional Visualization of Crystal, Volumetric and Morphology Data. *J. Appl. Crystallogr.* **2011**, *44*, 1272-1276.

(33) Xue, J.; Fujitsuka, M.; Majima, T. The Role of Nitrogen Defects in Graphitic Carbon Nitride for Visible-Light-Driven Hydrogen Evolution. *Phys. Chem. Chem. Phys.* **2019**, *21*, 2318–2324.

(34) Chun, W. J.; Ishikawa, A.; Fujisawa, H.; Takata, T.; Kondo, J. N.; Hara, M.; Kawai, M.; Matsumoto, Y.; Domen, K. Conduction and Valence Band Positions of Ta_2O_5, TaON, and Ta_3N_5 by UPS and Electrochemical Methods. *J. Phys. Chem. B* **2003**, *107*, 1798–1803.

(35) Wang, Z.; Inoue, Y.; Hisatomi, T.; Ishikawa, R.; Wang, Q.; Takata, T.; Chen, S.; Shibata, N.; Ikuhara, Y.; Domen, K. Overall Water Splitting by Ta_3N_5 Nanorod Single Crystals Grown on the Edges of $KTaO_3$ Particles. *Nature Catal.* **2018**, *1*, 756–763.

(36) Maeda, K.; Domen, K. Water Oxidation Using a Particulate $BaZrO_3$-$BaTaO_2N$ Solid-Solution Photocatalyst That Operates under a Wide Range of Visible Light. *Angew. Chem. Int. Ed.* **2012**, *51*, 9865–9869.

(37) Dong, B.; Qi, Y.; Cui, J.; Liu, B.; Xiong, F.; Jiang, X.; Li, Z.; Xiao, Y.; Zhang, F.; Li, C. Synthesis of $BaTaO_2N$ Oxynitride from Ba-Rich Oxide Precursor for Construction of Visible-Light-Driven Z-Scheme Overall Water Splitting. *Dalton Trans.* **2017**, *46*, 10707–10713.

General Conclusion

In this thesis, flux method is used to obtain high crystallized $BaTaO_2N$ crystals with some special surface features, thereby improving the photocatalytic performance. In the Chapter 1, $BaTaO_2N$ crystals co-exposed with {100} and {110} facets are achieved by using KCl flux assisted nitridation process, which show a higher activity than $BaTaO_2N$ crystals with sole {100} facets prepared by NaCl flux and $BaTaO_2N$ crystals prepared by conventional method. Based on the analysis of experimental and theoretical results, the samples prepared by flux method contain fewer defects than that prepared by conventional method, and the photogenerated electrons and holes separately transfer to the {100} and {110} facets of $BaTaO_2N$ because of the different energy levels of {100} and {110}. Due to the enhanced crystallinity and spatial separation of charge carriers, BTON (KCl) shows a good performance. Following Chapter 1, the effect of other chloride fluxes on the crystallinity and activity of $BaTaO_2N$ is studied, and the optimal flux is selected to explore the suitable synthetic conditions in Chapter 2. An excellent photocatalytic activity for H_2 evolution is obtained by using RbCl flux due to the lower defect density and higher crystallinity. The suitable synthetic conditions for BTON (RbCl) are Ba/Ta molar ratio of 1.10 (or 1.15), solute concentration of 10 mol%, holding temperature of 950 ℃ and holding time of 8 h. Differently, in Chapter 3, the binary flux (K_2CO_3 and KCl) is used to control the morphology of $BaTaO_2N$. During the nitridation process, the existence of CO_3^{2-} promotes the formation of oxo-complex $[TaO_3]^-$, and the O^{2-} in the oxo-complexes is replaced by the nitriding species produced by the dissociation of NH_3, leading to the simultaneous formation and transformation of $Ba_5Ta_4O_{15}$. Moreover, the atomic arrangement of the $BaTaO_2N$ (111) plane matches well with that of the $Ba_5Ta_4O_{15}$ (001) plane, so that the platy $BaTaO_2N$ crystals exposed with {111} facets are obtained consequently. Owing to the plate-like structure and high crystallinity, the platy $BaTaO_2N$ exhibits an excellent photocatalytic performance for H_2 evolution at the molar ratio of 20/80.

In summary, BaTaO$_2$N co-exposed with {100} and {110} facets is developed to facilitate spatial charge separation, a higher crystallinity BaTaO$_2$N with low defects is fabricated to reduce the generation of recombination centers, and a platy BaTaO$_2$N is obtained to decrease the migration distance of photogenerated electrons and holes. All these positive features result in an enhanced activity of BaTaO$_2$N. Therefore, the design and discovery of photocatalysts with desirable shape and high crystallinity *via* refinement of the fabrication procedure and the use of various flux species is an important strategy to further improve the photocatalytic performance of (oxy)nitrides. For example, highly crystalline one-dimensional (rods and wires) and two-dimensional (discs and plates) (oxy)nitride photocatalysts, which usually have large surface area and low defect density, are expected for water splitting by using suitable flux with some special properties. Moreover, since the different electronic properties of different facets will affect the photogenerated charge separation, it is worth investigating the (oxy)nitride crystal uniformly exposed isotropic or anisotropic facets by considering the characteristics of ions in flux. This study provides a facile approach to develop efficient (oxy)nitride photocatalysts for solar energy conversion.

List of Publications

1. **Ying Luo**, Sayaka Suzuki, Zheng Wang, Kunio Yubuta, Junie Jhon M.Vequizo, Akira Yamakata, Hiromasa Shiiba, Takashi Hisatomi, Kazunari Domen, Katsuya Teshima, Construction of Spatial Charge Separation Facets on $BaTaO_2N$ Crystals by Flux Growth Approach for Visible-Light-Driven H_2 Production, *ACS Appl. Mater. Interfaces,* **2019**, *11*, 22264–22271.

2. **Ying Luo,** Zheng Wang, Sayaka Suzuki, Kunio Yubuta, Nobuko Kariya, Takashi Hisatomi, Kazunari Domen, Katsuya Teshima, Fabrication of Single-Crystalline $BaTaO_2N$ from Chloride Fluxes for Photocatalytic H_2 Evolution under Visible Light. *Cryst. Growth Des*. **2020**, *20*, 255–261.

3. **Ying Luo**, Zheng Wang, Tetsuya Yamada, Kunio Yubuta, Sayaka Suzuki, Takashi Hisatomi, Kazunari Domen, Katsuya Teshima, Platy $BaTaO_2N$ Crystals Fabricated from K_2CO_3–KCl Binary Flux for Photocatalytic H_2 Evolution, *ACS Appl. Energy Mater.* **2020**, *3*, 10669–10675.

Acknowledgements